Characterization and Finite Element analysis for soft magnetic materials used in automotive applications

By

Hayat A. Eltawahni B.Sc. Eng

A Thesis Submitted in Fulfilment of the Requirements for the Degree of
Master of Engineering (M. Eng)

Supervisors
Prof. Saleem Hashmi & Dr. Abdul-Ghani Olabi

School of Mechanical and Manufacturing Engineering
Dublin City University

May 2006

DECLARATION

I hereby certify that this material, which I now submit for assessment on the program of study leading to the award of master of engineering is entirely my own work and has not been taken from the work of others save and to the extent that such work has been cited and acknowledged within the text of my work.

Signed: ______________ ID: 52149706

Date: 25/06/06

ACKNOWLEDGEMENTS

First of all I would like to express my sincere thanks and gratitude to Almighty Allah, who helped and blessed me during the course of my studies.

Also, I am really grateful to my supervisors Prof. M. S. J. Hashmi and Dr. Abdul Ghani Olabi. Without their continuous help and advice this work would not have been made possible.

I am thankful to my, father, mother and my family, which have given me the chance of discovering what I like, and of devoting myself to it.

I also would like to take this opportunity to extend my thanks to Dr. Aran Rafferty for his support.

I would like to thank the technical staff of the School of Mechanical & Manufacturing Engineering, especially Mr. Liam Domican and Mr. Chris Crouch.

I also would like to gratefully acknowledge the Libyan government for the financing of this research.

Last but not least I would like to take this opportunity to extend my thanks to each one of my friends, here in Ireland and back home, for their honest and sincere concerns about my study and myself.

Characterization and Finite Element analysis for soft magnetic materials used in automotive applications

Hayat A. Eltawahni, B.Eng.

ABSTRACT

This project aims to develop and optimize soft magnetic materials for use in solenoids for automotive components such as: electric injectors, electric valves, electric pumps… etc. The work seeks to produce soft magnetic materials with higher magnetic permeability to produce higher magnetic forces in solenoids.

Powder metallurgy was used to produce the magnetic solenoid parts with a wide array of possible material combinations. Different mixtures of Fe-Si, Fe-Co and Fe-Si-Co were developed. A cold-isostatic compacting technique was used with a pressure of 180 MPa. Then the samples were sintered twice at a temperature of 1315 °C for 45 min after compacting, and after the final machining.

Density, compression, hardness and microstructure were investigated for all samples before and after the second sintering. The results showed that the mechanical properties and the microstructure were improved after the second sintering.

The magnetic density and intensity (B-H) was determined for each material. A sample of each new material was sent to an American Lab.

Finite element simulations were carried out using commercial software (ANSYS) to simulate the magnetic field of a common rail electro-injector solenoid. The maximum magnetic force was determined for each developed material.

Different models were built-up by varying the magnetic material properties and the working parameters such as the coil turn - current for a fixed gap between the armature and the back iron.

TABLE OF CONTENTS

LIST OF FIGURES

LIST OF TABLES

CHAPTER I
INTRODUCTION

1. INTRODUCTION

Archaeological evidence suggests that Powder Metallurgy (P/M) has a history dating back to 2500 B.C. in Persia. Egyptians are also said to have used P/M techniques to make iron tools as far back as 3000 B.C. P/M was adapted long before artisans were melting and casting iron. P/M parts have been used in magnetic applications for many years. Magnetic applications make use of P/M, due to both economical benefits and design flexibility. In the powder metallurgy industry there is the belief that soft magnetic parts made from iron powders hold the key to the future prosperity of ferrous-based powder metallurgy products. The benefits of powder metallurgy, such as its near net shaping capabilities with high dimensional precision and maximum material savings are making it an ever more preferable process for the fabrication of soft magnetic components. While the magnetic and electric properties of powder metallurgy parts were once below that of wrought materials, they are increasingly offering the same, and sometimes better, level of performance. The development of new powder metallurgy techniques, along with great activity in the research for superior performing materials, promises to progress the industry in the near future [1, 2, 3].

1.1 Powder Metallurgy Process.

Metallic powders are produced by different mechanical and chemical techniques. These techniques have various effects on the densification mechanism and the properties of grains formed during sintering. Parts produced by powder metallurgy are used in massive quantities in a wide variety of industries as this process couples unique technical features with low cost. P/M technology has a wide application in producing components which are homogeneous, have controlled density, high purity and uniform strength. The P/M process has some advantages and disadvantages. Its advantages are:

1. Excellent surface finishes
2. Ability to use the benefits of controlled porosity
3. Only cost-effective processing, if the starting powders are available.

4. Process easily adapted to produce small quantity of a given shape.

The Disadvantages of this technique are:

1. Costs of powder production
2. Limitations on the shapes and features which can be generated, e.g. process cannot produce reentrant angles by fixed die pressing or radial holes in vertically pressed cylinders
3. The size will always change after sintering [4].

The P/M process consists of three main stages as shown in Fig. 1.1. The first stage is mixing the metallic powders with binder and/or lubricant powders. Then, compaction can be done by various methods, depending on the shape required. Finally, sintering of the green compact is the last stage. Furthermore, during sintering, the atmosphere, time and temperature have considerable effects on the properties of the component [5].

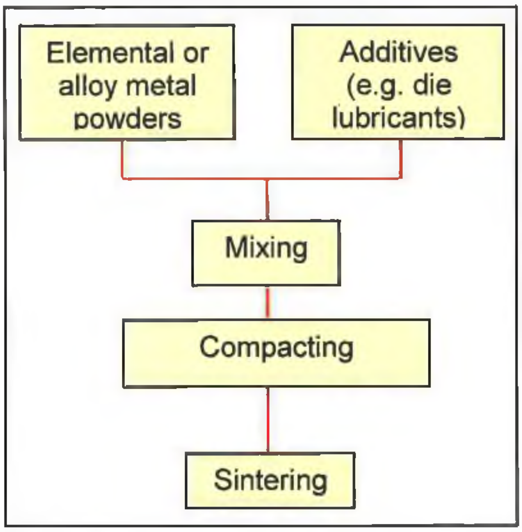

Fig.1.1: Powder metallurgy process main stages.

1.1.1 Mixing

For most metal powders, mixing is carried out using rotating containers that have different shapes as shown in Fig.1.2. The mixer shape and the volume of the powder in the mixer determine the mixing efficiency. A powder volume that occupies 20 to 40% of the mixer's capacity would give a good mixing efficiency. The rotation speed also has a large effect on the mixing efficiency. Rapid rotation will create a high centrifugal force upon the powder which interferes with powder flow. Small centrifugal forces are desirable, they would give the best mixing, but not so small that turbulence does not occur [5].

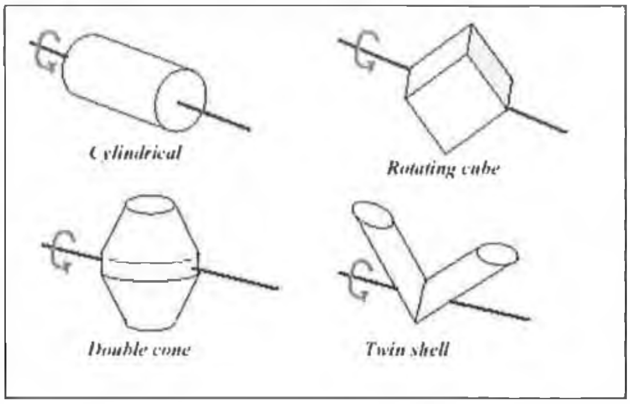

Fig.1.2: Some common equipment geometries for mixing or blending powders [5]

1.1.2 Compacting

Compaction relies on an external source of pressure for deforming the powders into a relatively high density mass, also providing shape and dimensional control to the powder. This pressure determines the components densities.

The most common compacting techniques are axial and isostatic pressing. In axial pressing, the powder is compacted unside rigid dies by punches which increase the density. The axial compaction pressure, which is defined as the punch load divided by the punch face area, is the main process variable. In isostatic pressing the powder is sealed in a flexible mold and exposed to the hydrostatic pressure of a liquid. As a consequence, the green compact properties such as density are more uniform. In both cases, the density approaches a final density level, which is below the theorical density of the materials as shown in Fig.1.3 [5].

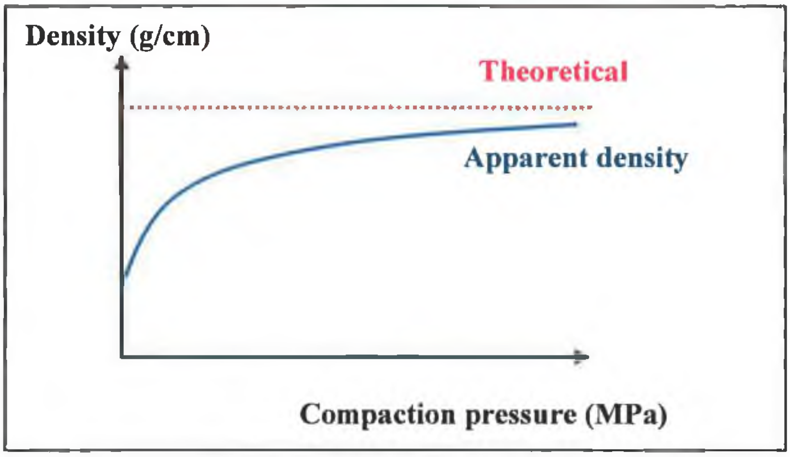

Fig. 1.3: Density behaviour during compacting [5].

1.1.2.1 Axial pressing

In axial compacting, the metal powder is compacted between the punch faces and the die walls. Using this technique very close geometrical tolerances can be obtained. Therefore, axial powder pressing is a very economic way for pressing metal powders in mass production. The floating die shown in Fig. 1.4 is usually used to produce cylindrical or rectangular compacts at pressure levels up to 800 MPa. After ejection, the compact density can be estimated from its mass and dimensions [6].

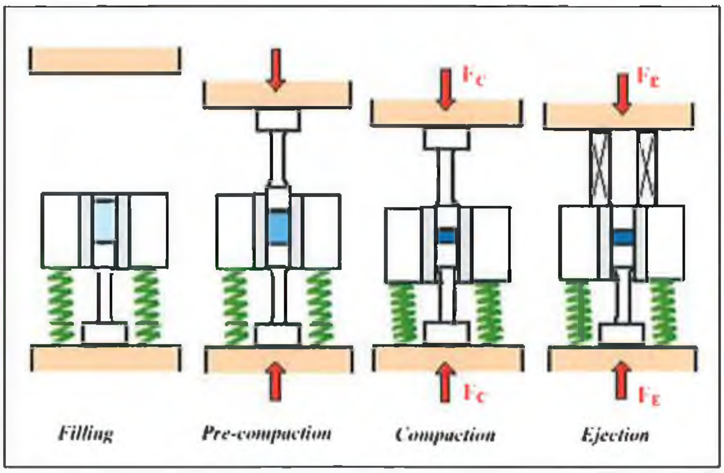

Fig. 1.4: Various stages of the axial compaction.

1.1.2.2 Cold isostatic pressing

Cold isostatic pressing, shown in Fig.1.5, is carried out in practice either by the wet bag or the dry bag method. By using wet bag tooling, the flexible bag of the mold should be filled outside the pressure vessel, sealed and finally placed in the vessel. The bag is completely surrounded by the pressure-exerting fluid. With dry bag tooling the bag is permanently sealed within the pressure vessel which means that the powder must be filled without removing it from the vessel. It can be mentioned that the dry bag tooling is more limited in shape flexibility, but it is more suitable for mass production. Cold isostatic pressing is usually performed at pressures below 350 MPa [6].

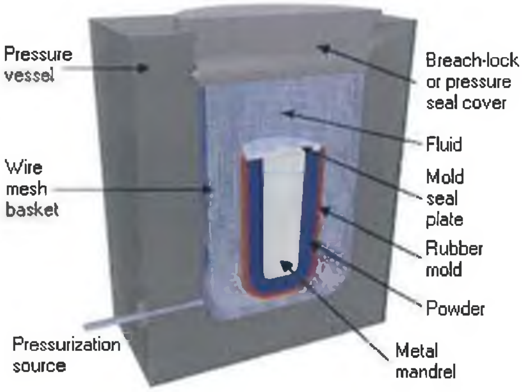

Fig.1.5: Isostatic press components [7].

The flexible mold, which usually contains the powder, has the same shape as the desired part. Different shapes of bags can be used to obtain the required shape. It is necessary to maintain the seals tight during the isostatic pressing to prevent leaking of the pressurization fluid into the powder [6].

This pressing technique is useful in making large, homogeneous compacts. Compared to axial pressing, the isostatic pressing method provides uniform pressures around the flexible mold which produces better compaction uniformity with an increment in shape capabilities. Moreover, isostatic compaction is more efficient when compared to die compaction at a given pressure. It is necessary to reduce the air contained in the bag to obtain the best possible results. Therefore air is removed with a vacuum pump. Isostatic pressing has many advantages over axial die pressing as described in the following points: The shape capability, is much less restricted in isostatic pressing. Parts of thin walled compacts with large height/diameter ratios can be produced with the absence of die wall friction effects. The only size limitation for the compact is the dimension of the pressure vessel as the hydrostatic pressure is acting homogeneously within the pressure fluid. The density distribution within the compacts is homogeneous, which again is related to the absence of wall friction. The ejection step is different. This is important mainly for compacts of low green strength. The compaction pressure for such materials in die pressing is limited by ejection shear stresses, which can cause failure when the compacts leave the die [6].

1.1.3 Sintering

Heating the metal powders to temperatures below but close to the melting temperature bonds its particles together; this phenomenon is termed sintering. On a microstructural scale, cohesion takes place as necks (welds) grow at the points of contact between particles, as can be seen in Fig. 1.6. The material properties improve as the growth of these necks continue during the sintering process [5].

Fig. 1.6: Neck in the point of particle contact.

1.1.3.1 Sintering effects on properties

Compact hardness, strength, fatigue life, toughness, ductility, electrical conductivity, magnetic saturation, and corrosion resistance are common properties that are usually considered important. The degree of sintering, in terms of neck size, shrinkage or densification, has a different effect on each of these properties. Generally they improved with the increase in the sintering temperature. An example of this effect in terms of the sintering temperature is shown in Fig. 1.7. The dynamic properties (fatigue and impact strength) prove to be the most sensitive to the sintering level. Using high sintering temperatures lead to rapid sintering, but this is not always favourable due to the higher expense in furnace design and energy cost [5].

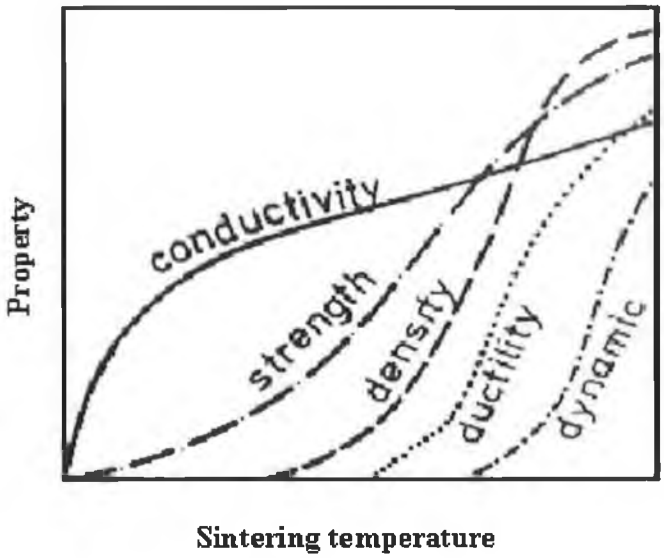

Fig. 1.7: Compact properties with the degree of sintering as represented by the sintering temperature [5].

1.1.3.2 Sintering conditions (atmosphere and furnace)

To avoid oxidation during sintering the process has to be carried out in a reduced atmosphere, to avoid the formation of oxides on the powder surface which would prevent diffusion bonding and result in inadequate properties [6]. In order to provide the time-temperature control to the sintering cycle, special sintering furnaces are used. Two main factors control the selection of the furnace type, the furnace temperature and the compact position. Fig. 1.8 shows the time-temperature cycle needed in commercial sintering treatments [5].

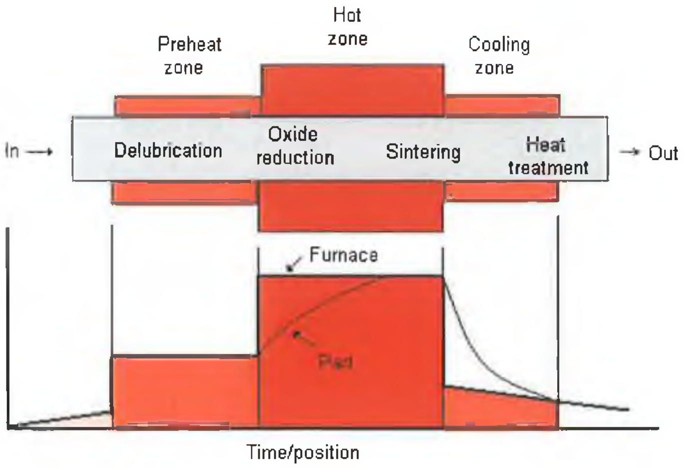

Fig. 1.8: Plan for the sintering of commercial parts [5].

1.2 Soft Magnetic Materials

One of the earliest known form of magnets is loadstone, an iron oxide ore, originally mined from a material called magnetite. The name magnet comes from a region called Magnesia, of present-day turkey, where much of the material was mined. Soft magnetic materials are those materials that are easily magnetised and demagnetised. They typically have an intrinsic coercivity less than 100 Am^{-1}. They are used primarily to enhance and channel the flux produced by an electric current. Currently, magnetic materials are important factors in technology, from data memory to motors. The history of soft magnetic materials is traced from 1000 B.C. to the preset time. This includes the work of Oersted and Faraday who invented the first transformer, and the gradual improvements in core materials over the last 150 years. These cover soft iron, silicon iron, grain orientation, domain control by lasers, and spark ablation. Nowadays, Soft magnetic materials play a key role in power distribution, allow the conversion between electrical and mechanical energy and play a fundamental role in many electrical and electronic systems [8].

1.2.1 Basic concepts

Magnetic forces are generated by moving electrically charged particles; these magnetic forces are in addition to any electrostatic forces that may prevail. Many times it is convenient to think of magnetic forces in terms of fields. Imaginary lines of force may be drawn to indicate the direction of the force at positions in the vicinity of the field source. The magnetic field distributions as indicated by lines of force are shown for an electrical current loop and also a bar magnet in Fig. 1.9.

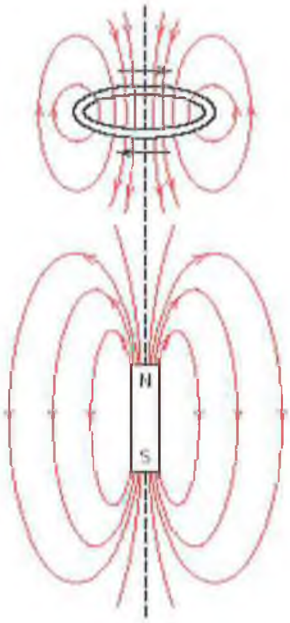

Fig. 1.9: Magnetic field lines of force around a current loop and a bar magnet [8].

Magnetic behaviour can be described in terms of several fields. The externally applied magnetic field, sometimes called the magnetic field strength, and is denoted by H (A/m). If the magnetic field is generated by means of a cylindrical coil (or solenoid) consisting of N closely spaced turns, having a length L, and carrying a current of magnitude I, then the magnetic field strength is expressed by:

$$H = {}^{NI}\!/_{L} \qquad (1)$$

A schematic diagram of such an arrangement is shown in Fig. 1.10a. The magnetic field that is generated by the current loop and the bar magnet in Fig.1.10b is an H field.

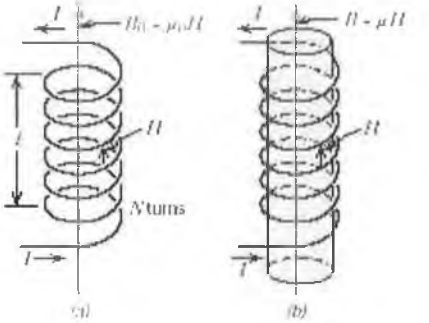

Fig. 1.10: The magnetic field and the magnetic flux density (a) Cylindrical coil and (b) Solid material [8].

The magnetic flux density, or magnetic induction, denoted by B, corresponds to the magnitude of the internal field strength within a body that is subjected to an H field. H is determined from Eq. (1). The units for B are teslas. Both B and H are field vectors, being characterized not only by magnitude, but also by direction in space. The magnetic flux density, B, also depends on the material that the field is running through. The material property of concern in this relation is the permeability, denoted by μ, and has the units of H/m (Henries/m). In Fig. 1.10a, for example, the magnetic field could be running through vacuum, which is often taken as a reference for the magnetic properties of materials. In this case, the magnetic flux density can be calculated from

$$B_0 = \mu_0 H \qquad (2)$$

Where: μ_o is the permeability of vacuum, a universal constant equal to ($4\pi.10^{-7}$ H/m). The flux density is denoted by B_0, to indicate that vacuum is the medium of interest. If the medium is a solid material (e.g. a solenoid), as in Fig. 1.10b, the relation for magnetic flux density takes the form

$$B = \mu H \tag{3}$$

Where: μ is the permeability of the core material.

The material's permeability is sometimes quoted as the relative permeability in material handbooks and data sheets. The relative permeability μ_r is a measurement of the material's permeability expressed as a ratio of the permeability of the material divided by vacuum permeability as described in Eq. 4.

$$\mu_r = {}^{\mu}\!/_{\mu_0} \tag{4}$$

μ_r has no units and it indicates the degree to which the material can be magnetized, or how easily a magnetic field flux, B, can be induced in the presence of an external H field [9].

1.3 Soft Magnetic Materials

As mentioned earlier soft magnetic materials are those materials that are easily magnetised and demagnetised. They normally have natural coercivity less than 1000 $\mathrm{Am^{-1}}$. The most important parameter, often used as a quality reference for soft magnetic materials, is the relative permeability μ_r, which is an indication of how easily the material reacts to an applied magnetic field. The other key parameters of interest are the coercivity, the saturation magnetisation and the electrical resistivity.

Applications for soft magnetic materials fall into two main categories; DC and AC systems. In DC applications the material is magnetised in order to perform a function and then demagnetised at the end of the function, e.g. an electromagnet on a winch at a scrap yard will be switched on to attract the scrap steel and then switched off to drop the steel. In AC applications the material will be continuously cycled from being magnetised in one direction to the other, during the period of operation, e.g. a power supply transformer. High permeability is desirable for both applications. However, the significance of the other properties, such as coercivity, may differ [10].

1.4 The Hysteresis Loop and Magnetic Properties

A hysteresis loop shows the relationship between the induced magnetic flux density B and the magnetizing force H. It is often referred to as the B-H loop. By studying the hysteresis loop a great deal of information can be learned about the magnetic properties of a material. An example of a hysteresis loop is shown in Fig.1.11. The loop is created by recording the magnetic flux B of a ferromagnetic substance as the magnetizing force H is changed. A ferromagnetic substance that has never been magnetized or has been completely demagnetized will follow the dashed line as H is increased. As the line discloses, the greater the amount of current applied (H+), the stronger the magnetic field in the substance (B+). At point "a" approximately all of the magnetic domains are aligned and an additional increase in the magnetizing force will produce very little increase in magnetic flux. The substance has reached its saturation point of magnetism. As H is reduced back down to zero, the curve will move from point "a" to point "b." At this point, it can be seen that some magnetic flux remains in the material although the magnetizing force is zero. This indicates that the remanence or level of residual magnetism in the substance. When the magnetizing force is reversed, the curve moves to point "c", where the flux is reduced to zero. This is called the point of coercivity on the curve. The force required to remove the residual magnetism from the material, is called the coercive force or coercivity of the material. As the magnetizing force is increased in the negative direction, the material will again become magnetically saturated but in the reverse direction at point "d". Increasing H to zero brings the curve to point "e", which will have a level of residual magnetism equal to that reached in the other direction. Increasing H back in the positive direction will return B to zero. Notice that the curve does not return to the origin of the graph because some force is required to remove the residual magnetism. The curve must take a different path to complete the loop from point "f" back the saturation point. From the hysteresis loop, several important magnetic properties of a material can be determined such as [11]:

1. Retentivity - It is a material's capability to hold a certain amount of residual magnetic field when the magnetizing force is removed after achieving saturation. In the diagram it is the value of B at point “b” on the hysteresis curve.
2. Residual Magnetism or Residual Flux - this is the magnetic flux density remaining in the material when the magnetizing force has disappeared. Note that residual magnetism and retentivity are the same when the material has been magnetized to the saturation point. However, the level of residual magnetism may be lower than the retentivity value when the magnetizing force does not reach the saturation level.
3. Coercive Force - The amount of reverse magnetic field which must be applied to a magnetic material to make the magnetic flux return to zero. This is the value of H at point “c” on the hysteresis curve.
4. Permeability, μ - A property of a material that describes the ease of establishing a magnetic flux in the component.
5. Reluctance - Is the resistance that a ferromagnetic material exhibits to the establishment of a magnetic properties in a complete circuit. Reluctance is similar to the resistance in an electrical circuit [11].

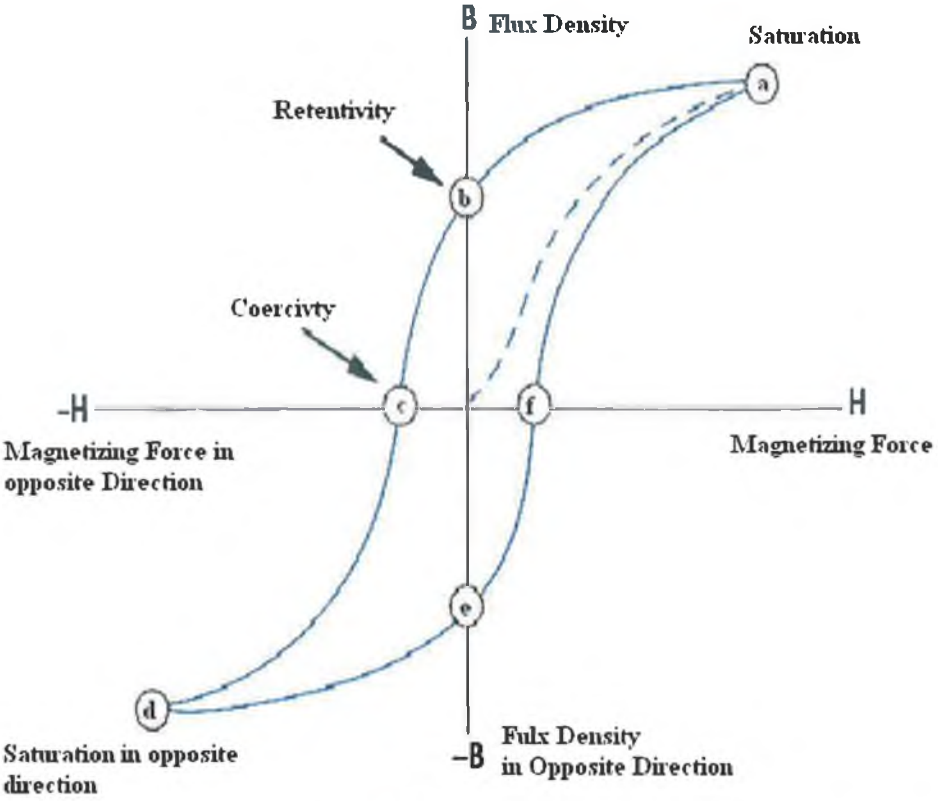

Fig. 1.11: A sample Hysteresis loop for a ferromagnetic material [9].

1.5 Solenoid

A solenoid is an electromechanical system, which usually consists of a coil and a movable iron core named an armature. The solenoid works as follows: When current flows through the coil, a magnetic field is generated around the coil. With many turns of wire as shown in Fig.1.12, this magnetic field becomes many times stronger, flowing around the coil and through its centre in a doughnut shape. When the coil is energized with current, a core inside it is also magnetised in a magnetic material. If this core is in two parts, separated by an air gap, and one part is free to move. The two parts will be attracted to each other, and the part which is free to do so, will move towards the fixed part. The core moves to increase the flux linkage by closing the air gap between the two parts of the core. The movable part is usually spring-loaded to allow it to retract when the current is switched off. The force generated is approximately proportional to the square of the current and inversely proportional to the square of the length of the air gap. Solenoids are inexpensive, and they are used in on-off applications such as latching, locking, and triggering [11].

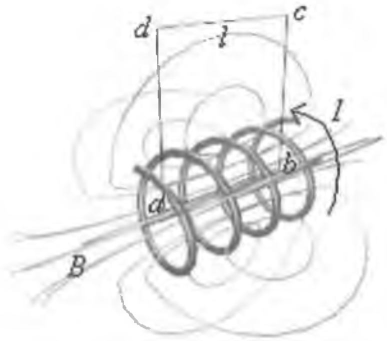

Fig. 1.12: Magnetic field coil [11].

1.5.1 Types of solenoids and their applications

Solenoids have three common types, electromechanical solenoids, which utilize electrical energy; pneumatic solenoids, which gain their energy from compressed air and hydraulic solenoids, which gain energy from pressurized fluids. Electromechanical solenoids are frequently used in electronic machines as well as in different parts of the car engine either for insult in diesel or CNG engines, solenoids are used as electro-injectors as shown in Fig.1.13, or reducing valves, etc. Pneumatic solenoids are popular for heavy tools and machining applications which required large power such as jackhammers. While, hydraulic solenoids, which are even more powerful, are normally used only for the heaviest projects such as wave pools and in aircraft manufacturing to bend titanium and other heavy metals [12]. Some solenoids that belong to each type explained above are shown in Fig. 1.14

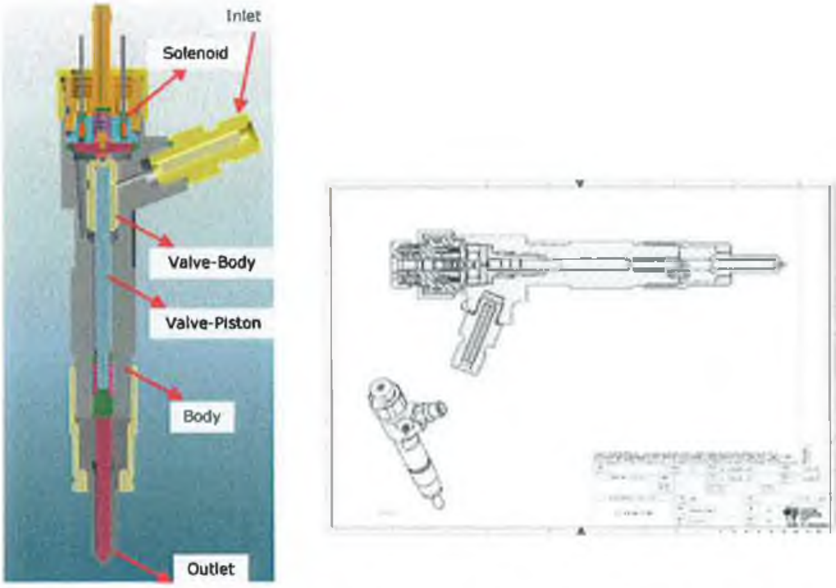

Fig. 1.13: The new industrial common rail electro-injector [40].

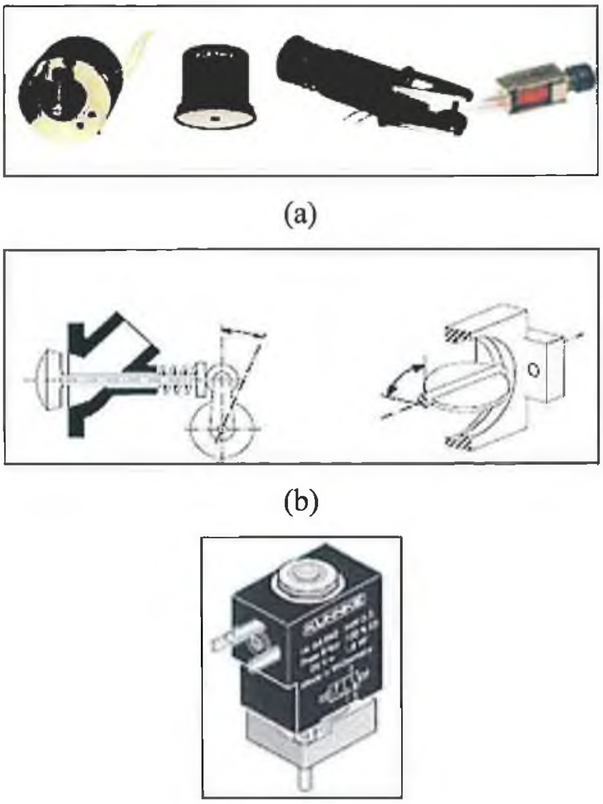
(a)

(b)

(c)

Fig. 1.14: Types of solenoid (a) electromechanical, (b) pneumatic and (c) hydraulic [12].

1.6 Present Work and its Objective

The objective of this work is to develop different binary and ternary alloy systems of soft magnetic material with an iron base with different percentages of Silicon and Cobalt using powder metallurgy processes for solenoid applications.

To achieve this objective the cold isostatic compacting technique with a compacting pressure of 180 MPa was applied to different mixtures of these binary and ternary mixtures of powders. The green compacts were sintered at 1315 °C for 45 Min. After the first sintering the samples were machined to their final required shape. Finally, the samples were re-sintered at 1315 °C for 45 min.

In order to characterize the produced samples, mechanical testing, densification measurements, microstructural characterization and H-B magnetic curve definition were carried out for all samples.

Finite element analysis was also performed using ANSYS to simulate the magnetic force for the solenoid using different current densities and gaps between the armature and the back-iron.

1.7 Outline of the Thesis

Chapter 1 gives an overall introduction about P/M process, the basic concepts of magnetism, properties of soft magnetic materials, definition of the hysteresis loop and magnetic properties as well as the different types of solenoids and their applications. The chapter also shows the current work objective. Chapter 2 shows the literatures review of articles related to the current work. Chapter 3 describes the experimental procedure, the equipment and the methods that were used. Chapter 4 summarizes the steps followed to build up the FEM models. Chapter 5 shows the results and discussion of the densification, mechanical properties, microstructural characterization and magnetic properties of the different samples. Chapter 6 presents the results and discussion of the FEM simulations. Finally, Chapter 7 outlines the conclusions of this investigation and some recommendations for future work.

CHAPTER II
LITERATURE SURVEY

2. LITERATURE SURVEY

This literature survey presents up to date information on powder metallurgy, soft magnetic materials properties and their applications in solenoids and how these properties change with the variation of the process variables.

2.1 Powder Metallurgy Process

Powder metallurgy is a highly developed method of manufacturing reliable ferrous and nonferrous parts. Much has been written over the past number of years related to the use of P/M parts in soft magnetic applications. In the last few decades many articles were published presenting the effects of mixing, compaction and sintering on the materials' properties.

2.1.1 Mixing

Powders can be mixed to form new compositions. Many powder metallurgy products rely on the mixing of elemental powders to obtain alloy formulations. Powders subjected to die compaction are lubricated to ease ejection and minimize die wear. It is common practice to mix a lubricant with the powder before compaction. For some types of powders, a binder is added to achieve a high green strength (strength after pressing). This is the case for the finer powders, especially of the harder materials. During sintering, both the lubricants and binders are burned out of the compacts. Popular lubricants are stearate salts of Al, Zn, Li, Mg or Ca, especially zinc stearate, and increasingly, other organic compounds of a waxy nature [5].

Semel et al. [13] have investigated the lubricating effects on the pressing properties of an ordinary binder versus one containing a lubricant. The results show that the lubricating binder is superior in terms of its effects on compressibility and dies ejection forces.

Galdarov et al. [14] have investigated the effect of the lubricant in the mixture on the properties of the sintered product. Zinc stearate as a lubricant was mixed with iron powder in different proportions. It was found that the ejection force decreases when the zinc stearate content was increased, and the agreeing with Semel density of a sintered compact increases with the increase in zinc stearate up to 0.5% and after that it starts to decrease. This extends the work of Semel to the stage after sintering and suggests that high density before sintering will lead to high density after sintering. It was also found that the hardness decreases with the increase in zinc stearate content.

Another study has been undertaken by Uede et al. [15] to investigate the effect of Zn stearate mixed with Fe powder, on die compaction, green density, die wall friction and friction between particles of the powder. It was concluded that 0.5wt% Zn stearate is the most suitable amount for optimum powder flow and uniformity of density agreeing with Galdarov. It was found that the added lubricant improved powder friction but not green density disagreeing with Semel. A reduced amount of lubricant (less than 0.5%) could still be effective but the compaction pressures must then be above 700 MPa.

Lawrence et al. [16] have investigated the effect of lubricant particle size on compaction, ejection force and green density. The results indicated that fine lubricants provide higher green density and higher strength, while the only effect of coarse lubricants was to reduce the ejection force required. Perhaps this helps to reconcile the differences between Uede and Semel. The results demonstrate that progress has been made toward the development of a new composite lubricant which was used by Lawrence. Ejection and sliding pressures have shown to be reduced when compared to the effects of a commercial composite lubricant.

Kao et al. [17] have investigated the effect of three types of lubricants added to atomized steel and pre-alloyed 316L stainless steel. It was concluded that the zinc stearate addition provides higher apparent densities agreeing with Semel and Galdarov. It was also indicated that the green strength decreases with increasing lubricant additions in steel powders, perhaps agreeing with Galdarov if green strength is equated with hardness, but indicating also that the effects described by Lawrence using fine lubricants was not observed.

2.1.2 Compaction

Compaction is one of the most important stages in the sinter-forming route. It gives the powder an initial shape and gives the compact the necessary strength for handling in further operations. Wheatley et al. [18]worked with electrolytic iron powder, and found that increasing the compacting pressure resulted in smaller pore sizes. Also the structure displayed a more coherent appearance after sintering at 1050 °C.

Mamodov [19] discussed the factors which limit densification during compaction particularly factors relating to gases and lubricants. Techniques to reduce pore gas pressure were developed. Recommendations were made concerning the production of high density Fe based compacts by single cold pressing.

Gethin et al. [20] have carried out a detailed examination of uniaxial compaction of Fe powders. The compaction mechanism was studied and a total force balance was constructed. It was shown that there is a particle rearrangement phase for about 30% of the compaction stroke for Fe. The effect of friction was analysed using a friction coefficients of 0.1. A finite element model was developed and validated against the experimental data and good agreement was reported. Since this work was carried out quite soon after that of Mamodov, the effect of gas pressure in the pores was not considered.

Eksi et al. [21] have studied the effects of powder hardness and particle size on the densification of cold isostatically pressed (CIP) powders. The densification behaviours of aluminium, iron and alumina powders under CIP were examined. It was found that full densification was almost attainable with CIP in soft and easy to deform aluminium powders. For iron powder of medium hardness density 82% of the TD without removing air was achieved and 92% of the TD was achieved with removing air to a vacuum of 10^{-2} torrs the compaction pressure was 500 MPa. This is an example of the analysis carried out by Mamodov being applied to CIP.

2.1.3 Sintering

In the sintering furnace, when a critical temperature is reached, the energy associated with surface tension of a liquid film on the particles is sufficient to counteract viscosity forces opposing motion. This allows particle movement to minimized surface energy and causes the final bonding between the metal particles. Wiest [22] has reported that iron compacts sintered in Hydrogen were stronger and tougher than those sintered in vacuum but their fatigue strength did not differ significantly. This could be an important factor with regard to this project. The indication is that the iron particles had an oxide coat which was removed by the Hydrogen, but at the same time brittle Hydrogen formation was produced by excess Hydrogen. Perhaps better magnetic properties would be produced by sintering in Hydrogen.

Munitz et al. [23] have studied the effects of nitrogen and argon on Fe powders, with particular reference to their mechanical properties and microstructure. Both hot isostatic (HIP) and cold isostatic pressed (CIP) were used. The powders were compressed at 350MPa for 3 min by cold isostatic pressed (CIP) and sintered under either nitrogen or an argon atmosphere. It was found that the Fe [N] was very brittle and could not be turned on a lathe, while the Fe [Ar] could be machined easily. This again indicates that the iron reacks with the atmosphere during sintering.

Bas et al. [24] have investigated the manufacturing of soft magnetic materials using P/M. It was reported that by using P/M it is possible to obtain magnetic characteristics adjustable to the special needs of different applications and produce intricately shaped part having high dimensional accuracy with the maximum material savings.

The effect of density on a wide variety of powder metallurgy parts has been thoroughly documented. Generally, as density is increased almost all properties, including strength and magnetic performance are improved. Traditionally, density would be increased by raising compaction pressures, elevating sintering temperature, making sintering enhancement additions, and carrying out double press/double sintering processing (see next paragraph). Rutz and Hanejko [25] have studied high density processing of high performance ferrous materials for ANCORDENSE. It was mentioned that the density is an important factor in the performance of powder metallurgy components and it was concluded that high densities can be achieved at lower compaction pressures using methods such as double press/double sinter processing.

Roberts et al. [26] have also discussed the powder processing of soft magnetic composites. It was noted that the techniques of pressing powder are becoming more advanced. One such technique is the double-press double-sinter method (DP/DS). As its name suggests, this uses two pressing and sintering stages for the same sample. The first pressing is a conventional one, and the first sintering burns off the lubricant. The delubrication process can leave voids in the sample even after sintering, which is then repressed at the same pressure and sintered again. This increases the density of the sample considerably. Comparison between the Ancordense premix and conventional premix using the single-press single-sinter (SP/SS) and double-press double-sinter (DP/DS) methods was made. It was found that when compacting of the conventional material to 30 psi the green density was 7.00 g/cm^3 and after sintering the density was 7.01 g/cm^3, while the density after DP/DS was 7.22 g/cm^3. As a result of several compactions it was concluded that this technology increases the density of the sample considerably. It is not clear how long the dwell-time of the sintering stages was, and whether there could be any residual cracked when lubricant was removed.

Effects of high temperature sintering (HTS) of high performance silicon containing P/M steels to produce metallurgical and mechanical enhancements have been explored by Schubert et al. [27]. High temperature sintering of two silicon-containing materials, Ancorloy MDB and Ancorloy MDC, were investigated. It was concluded that silicon-containing P/M steel produces excellent properties when sintered above 1260 °C and the process was capable of attaining high apparent hardnesses. High temperature sintering has some advantages such as improving the Density, Mechanical properties, corrosion resistance and other physical properties like magnetic properties. It was mentioned that this technique has some key concerns such as cost, energy consumption and slow cooling rates. Table 2.1 shows the advantages and concerns of HTS.

Table 2.1: Advantages and concerns associated with HTS [27].

Advantages	Key concerns
• Increased homogeneity. • Elimination of some reducible oxides. • Increased diffusion rates. • Ability to properly process new high performance materials. • More pore rounding. • Larger mean pore spacing.	• Higher equipment/consumable expenditures. • Higher energy requirements. • Higher furnace maintenance costs. • Lower throughput. • The possibility of part distortion. • Slower cooling rates required.

The sintering atmosphere affects the pore size during sintering. Varela and whittemore [28] reported that during the sintering of MgO in an inert atmosphere like argon, pores shrink in the first few minutes of sintering due to rearrangement and other densifying mechanisms. In contrast, during the sintering of ZnO in dry argon at low temperatures, there was a slight widening of the pores with no grain growth.

2.2. Soft Magnetic Materials

The benefits of powder metallurgy, such as its near net shaping capabilities, are making it an increasingly attractive process for the production of soft magnetic components. The best soft or temporary magnetic materials have a narrow hysteresis loop. With regard to the basic measurable properties, this means that Hc should be as small as possible, while μ_m and B_m should be as large as possible. It is obvious that the optimal magnetic properties can be obtained when the maximum output (B) is achieved with the smallest energy input (H). In general, B_r should also be minimized, unless a reverse current is going to be applied during the application cycle. From an energy utilization standpoint, the area inside the loop is related to the work done in traversing the cycle and released as heat [29].

Lefebvre et al. [30] did a series of investigations to obtain materials with good magnetic properties. They conclude that the dielectric amount should be kept as low as possible while maintaining low eddy current losses. The influence of electrical resistivity on core losses in iron powder compacts at low frequency (f<1 KHZ) was presented. The results obtained show that if the resistivity is one order of magnitude higher than the resistivity of iron (~ 0.1μΩm) it is sufficient to maintain low eddy current losses in powder cores at frequencies below 100Hz.

For iron parts, the density has the greatest controlling influence on magnetic properties. The density increases as the sintering temperature is increased. Another way to improve density is to use a high compressibility powder. This might be achieved using high-purity materials. Another factor to improve the magnetic properties is the cooling rate which optimises the annealing operation. However, it must also be sintered adequately to obtain good soft magnetic properties [29].

The silicon content of textured Si-Fe alloys must fall within a narrow range, of 3 to 3.5% since, no commercial Si-Fe sheets have been produced with more than 3.5%. The early trials in cold-rolling of alloys containing 4% or more Si proved to be not suitable for cold-rolling, due to the brittleness. On the other hand, it can be considered as an advantage to use higher Silicon contents because this leads to the lower magnetostriction and this might solve some of the remaining problems of power transformer cores made of 3.25% Si-Fe sheets [31].

Bas et al. [32] have investigated the effect of silicon and cobalt content on the soft magnetic properties of iron based materials. It was concluded that silicon increases the iron's resistivity, reducing losses due to eddy currents. A silicon content of 3wt% would give a resistivity of about 50μΩcm and this is sufficient to eliminate the eddy current problem according to Lefebvre. During the entire sintering of Fe-Si the α-phase was maintaned, giving a large ferrite grain size which helps to promote a low coercivity and a high permeability and good induction. It was also reported that cobalt's ferromagnetic properties increase when alloyed with iron so that the material has a higher induction response at low magnetic fields when manufactured by HDT. The saturation induction was almost reached at 12 A/cm with an induction of almost 2T. Iron-cobalt is used in circuits where a high induction to volume (or weight) ratio is needed.

Gumlich and Goerens [33] have studied the addition of 2-2.5% silicon on the magnetic properties of iron based materials. It was found that the magnetic softness was increased considerably the coercivity being reduced to about one-half of the standard iron cores.

Rulz et al. [34] have developed materials and processes to improve the magnetic properties for several electromagnetic applications. It has been found that the addition of phosphorus and silicon can significantly improve the magnetic permeability relative to pure iron agreeing with Gumlich and Goerens. The iron and iron phosphorus materials were sintered at 1120°C. Whereas the sintering of the iron silicon alloys was done at the higher temperature of 1260 °C to homogenize the silicon. It was demonstrated that larger grain size and greater pore rounding could be obtained using higher sintering temperature. Consequently, higher permeability and significantly lower coercivity were obtained.

Hanejko et al. [35] have studied the effect of silicon additions to iron of 1%, 2% and 3% on the magnetic properties of P/M compacts compacted at 480 MPa and 685 MPa and sintered at 1260 °C or 1315 °C to homogenize the silicon. It was found that increasing the silicon addition from 1% to 3% raised the permeability from 3100 to 5600 at the 1260 °C sintering temperature with a corresponding decrease in the coercivity from 1.6 Oersted to 1.0 Oersted. While sintering at 1315 °C increased the permeability from 3500 to 5950 with a corresponding decrease in the coercive force from 1.5 Oersteds to 0.9 Oersteds. P/M sintered iron with 3wt% silicon exhibits DC permeabilities up to 6000, and a DC coercivities of 1.0 Oersted. It was mentioned that the choice of alloy system and processing can be optimized to meet the specific magnetic requirements of the component. This work confirms the questions obtained by both Gumlich and Goerens and Rulz et al.

Jansson [36] has studied soft magnetic materials produced by P/M for AC applications. It was noted that higher compaction pressure increases permeability and decreases coercive force. It was mentioned that the silicon alloys require higher temperature sintering to achieve a metallurgically well sintered part with good magnetic properties this agrees with Rulz et al. and Hanejko et al.. It was reported that a sintered density of 7.3 g/cm^3 for ASC100.29+2%Si could be obtained if compacted at 785 MPa and sintered at 1250°C for 30 min. This leads to an increase of resistivity, improve the maximum permeability and decrease the coercive force to approximately one-third. Also ASC100.29+3%Si require a higher sintering time of 60min at 1250 °C to achieve good magnetic properties. Again this agrees with similar results by the other investigators.

Lall and Baum. [37] have also reviewed the performance of soft magnetic components produced by powder metallurgy. It was noted that the density has the greatest controlling influence on magnetic properties, and the density increases rapidly as the sintering temperature is increased. It was found that powders which highly compressible tend to produce products with increased densities. Iron-Silicon components were investigated in the study. It was found that the magnetic properties are much poorer if the sintering temperature was below 1200 °C, due to the fact that silicon oxide requires a high temperature to dissociate. The transient liquid phase produced when sintering near 1260-1315 °C, leads to rapid densification and, this, improves both mechanical and magnetic properties. This work provides an explanation why higher temperatures are needed when sintering Iron with Silicon.

Hanejko et al. [38] have investigated iron and silicon alloys made by mixing a pure iron powder with a silicon-iron intermetallic. This approach allows the flexibility to incorporate more silicon into the iron. Increasing the silicon contents result in higher resistivity levels. It was mentioned that to realize the full benefit of the Ferro-Silicon addition, the sintering operation must result in a homogenous Iron-Silicon alloy. Unlike Iron-Phosphorus alloys which will homogenize at 1120 °C, iron and silicon alloys required sintering temperatures of at least 1260 °C to achieve complete homogenization. This high sintering temperature requires special furnace quality with high purity atmosphere requirements.

Bas and Molins [39] noted that materials with low coercive force and high permeability such as Fe-Si and Fe-Ni have magnetic properties which are more easily damaged by machining than other alloys. It was indicated that the soft magnetic materials must be annealed in order to reorganize the crystalline structure and restore the initial magnetic properties. Annealing must be performed in vacuum furnaces or under hydrogen atmospheres with extremely slow cooling rates. This paper also describes the advantages of electromagnetic applications and in particular the actuator, it was mentioned that the solenoid actuator has the advantage of combining larger force and displacement with low cost.

German [5] has studied the soft magnetic properties of ferrous powder compacts. It was noted that high purity ferrous powders have three dominant characteristics, namely, a low interstitial level, a high density and a coarse grain structure. The magnetic properties have been determined from the hysteresis loop as measured on toroidal test geometry and the effects of several P/M variables on one of the magnetic properties were compared. It was found that at higher sintered density, pores are reduced, while higher sintering temperatures cause pore spheroidization at a constant density. Both factors would improve the magnetic characteristics. Also, the slower cooling rate from the sintering temperature improves permeability by reducing residual stress. As with other properties of P/M materials, the magnetic properties improve rapidly as the sintered density increases. Moreover it was found that any disruption of the uniform magnetic field is detrimental to the soft magnetic properties. Therefore, a low interstitial content and minimal porosity are beneficial. In this connection it is noted that the sintering atmosphere and the initial powder purity have the greatest effect on the interstitial content.

2.3 Application of Finite Element Method FEM to Solenoids

Finite Element Methods (FEM) has been used to simulate the electro-magnetic properties for different applications. Olabi and Ricco [40] have studied the application of a unique solenoid actuator for different automotive components, which would be used in different systems under different conditions. The analytical work of the application of FEM was carried out using ANSYS. Different models were built-up by varying the number of coil turns and the current, and varying the gap between the armature and the back iron, the movable part and the stationing part, both of which are magnetized by the coil. This study provides a wide range of results to estimate the required force for each gap. The study would help to design the ECU either for PMW (pulse width modulation) models or variable models.

Kajime [41] has applied FEM to study the relationship between the weights of moving parts of the solenoid and the switching time. It was found that with moving parts having smaller weight the switching time is greatly reduced, because smaller weights require smaller solenoid forces. It was reported that to eliminate the generation of eddy currents, materials with low conductivities are advantageous, as expected. Also, it was found that materials with high saturation magnetic flux densities are beneficial.

Ricco et al. [42] have analysed the effect of different parameters in a magnetically operated electro-injector for use in off-road applications. The analytical studies were implemented to simulate the solenoid actuator in the electro-injector. Different models were built-up by varying the material properties on the one hand and the working parameters such as number of coil turns and the current for a fixed gap between the armature and the back iron on the other. The analytical study was carried out using the FEM in the ANSYS programmes. It was concluded that Fe-50Ni and Fe-3Si give a very high electro-magnetic performance producing the highest forces.

Tao et al. [43] have studied the effect of the magnetic field intensity in a high-speed response solenoid valve. The approach used to simulate the HSV's magnetic field, was simplified by selecting plane containing the axial of symmetry of the valve, and using this as the basis of the model so that the finite element method can be applied. In addition, an optimal design method was developed for designing the solenoid valve to achieve larger magnetic forces using low power by making changes in the parameters and choices which the materials. The simulation was compared with experimental results. The comparison result confirmed that the simulation calculations and the proposed optimal design method were effective in HSV designing and in predicting its performance. This two dimensional approach was therefore shown to be effective.

Kano and Maeda [44] have used the finite element method to calculate the magnetic flux density and the thrust. An FEM program has been developed for analysing the magnetic field of a linear electromagnetic solenoid. In this program, the intensity of the magnetic field was also computed using a two dimensional. FEM and experimental results were in good agreement with the theoretical estimates, with an error of only 2 %.

CHAPTER III

EXPERIMENTAL PROCEDURES

3. EXPERIMENT WORK

Designers of electromagnetic devices utilizing wrought materials are faced with a wide variety of magnetic materials from which to choose. Similarly, designers of P/M soft magnetic components are faced with a multiplicity of Ferro-magnetic materials and processing paths to meet performance and cost requirements. In this study different powders were used throughout the experimental programme to produce parts with different percentages. In this research a comparison between several powder compositions was made. The general procedures employed were to prepare the mixtures and to measure the density after first and second sintering as well as to characterize the mechanical properties and magnetic properties under similar conditions. This chapter presents the materials and the equipment which were used in this study.

3.1 Material

Three metal powders have been selected as raw materials to produce soft magnetic materials. These materials are regularly used in engineering applications as soft magnetic materials [29,45]. The specifications of these powders as received from the manufacturer can be seen in Table 3.1.

Table 3.1: Metal Powders specification.

No.	Element	Molecular Weight g/mol	Particle size μm	Purity %	Density g/cm^3	Melting point °C
1	Iron	55.85	44	97	7.860	1535
2	silicon	28.09	44	99	2.330	1410
3	Cobalt	58.93	149	99.9	8.90	1493

3.2 Powder Mixing Tool

A uniform distribution of powders at the end of the mixing process is very important to obtain excellent mechanical and magnetic properties [6]. A stainless steel V-Shaped mixer of 1.25 litres capacity was used for mixing the powders. The rotating chuck of a lathe machine was used to support the mixer and rotate it at a speed of 40 rpm. Fig.3.1 shows a photograph of the V-Shaped mixer, which was designed by Al-Tousi [46]. Different percentages of there metal powders were mixed using V-Shaped mixer Table 3.2 shows the sample numbers and their compositions. Ten mixtures of 300 g each were mixed as presented below in Table 3.2.

Table 3.2: Sample composition

Elements	Samples									
	1	2	3	4	5	6	7	8	9	10
Fe	99%	98%	97%	99%	97%	95%	98%	96%	94%	92%
Si	1%	2%	3%	-	-	-	1%	1%	1%	1%
Co	-	-	-	1%	3%	5%	1%	3%	5%	7%

Fig.3.1: V-Shaped mixer.

3.3 Micromeritics Helium Pycnometer

Pycnometry was used to determine the true density of the metal powders. The skeletal Density, sometimes called the true density of the metal powders was determined using a small volume Accupyc 1330 instrument. Fig 3.2a is a photograph of this small volume pycnometer which uses a gas displacement technique to determine the volume of the tested sample. The density is calculated using the sample weight which was previously measured using a balance. The instrument measures the sample volume, excluding interstitial voids in bulk powders and any open porosity in the individual particles, to which the gas has access. Internal (closed) porosity is still included in the volume. This test is normally performed at room temperature, but can be performed at a customer-specified temperature in the range of 0 °C to 50 °C. Almost any solid samples as well as some fluid samples can be measured by this technique. A large volume helium pycnometer was used to determine the density after sintering. Fig. 3.2b is a photograph of the large volume pycnometer.

Fig.3.2: Accupyc 1330 pycnometer (a) small volume helium pycnometer and (b) large volume helium pycnometer.

3.3.1 Theoretical density calculation

The theoretical density of a mixture is calculated using the density of each material. The volume fraction of constituent *a* in a mixture of two constituents *a* and *b* can be defined as described below [47]:

$$f_a = \frac{(m_a / d_a)}{(m_a / d_a + m_b / d_b)} \qquad 3.1$$

Provided the total volume is the sum of the volumes of a and b.

The Theoretical density becomes then:

$$d = f_a * d_a + f_b * d_b \qquad 3.2$$

$$\% \text{ of Theoretical Density} = \left(\frac{\text{Measured density}}{\text{Theroetical}} \right) \times 100 \qquad 3.3$$

Where: m_a, m_b, d_a, and d_b are the masses and densities of each constituent.

3.4 Isostatic Tools:

3.4.1 The rubber bag

The rubber bag shown in Fig. 3.3 was filled with a powder mixture and sealed. In order to create a pressure-tight container, a sealing ring was inserted into the rubber top closure. Then the rubber bag was placed in a perforated aluminium container and attached to a vacuum pump as can be seen in Fig. 3.4. When the required vacuum was achieved the small rubber tube was clamped to avoid any liquid or air seepage into the bag during the pressing operation as shown in Fig.3.5. In order to create a pressure-tight container, the open top of the bag was closed by inserting a rubber closure which was held in place by two cable ties. The rubber closure had a central hole through it so that the bag could be evacuated through a small rubber tube.

Fig. 3.3: Rubber bag, top closure and vacuum tube.

Fig. 3.4: Vacuum pump and tubing connected to the rubber bag.

Fig. 3.5: The rubber bag with vacuum tube clamped, over the isostatic pressure chamber.

3.4.2 Cold isostatic press

Cold isostatic pressing, CIP, produces parts with uniform density and this leads to a reduction of internal stresses and a reduction in the potential for cracks. CIP also produces products that may have a higher green strength in critical regions. It can be used for complex shapes, and the product tend to have better machinability [48]. In this work the isostatic press used was a Convertible HIP/CIP type with maximum pressure of 180 MPa and maximum sample size up to 200 mm in diameter. Fig. 3.6 shows the breech nut used to close the press chamber. An isostatic press was available for this work in the laboratories of Enterprise-Ireland. In the process a chamber is filled with liquid and a pump is used to generate hydraulic pressure simultaneously and uniformly to all surfaces of the part being formed.

In operation the bag which had been previously filled with powder and then sealed was lowered into the press chamber as shown in Fig. 3.7 until it was below the surface of the liquid. Then the breech nut was put in position and the hydraulic pump started. The lubrication trials were carried out by increasing the chamber pressure gradually to the maximum pressure of 180 MPa. As the pressure was raised to the required level the powder was compressed into the desired form. After the pressing cycle was completed, the entire assembly was removed from the isostatic press. Fig. 3.8 shows the green compacted sample.

Fig. 3.6: The breech nut of the isostatic press, used to close the chamber.

Fig. 3.7: isostatic press.

Fig. 3.8: Green compact.

3.5 Sintering Unit

In this investigation, a Carbolite tube furnace type, CTF 3 1600 with a maximum temperature of 1600 °C was used. The furnace was supplied with a control system and one control temperature system can enter programmes with varies ramp runs and dwells. Fig. 3.9 shows the tube furnace. The furnace was calibrated using a reference thermocouple; Fig. 3.10 shows the calibration curve curried out by other worker [55]. Insulation plugs were mounted at both ends of the tube to prevent heat loss and ensure good uniformity of the temperature then the tube was closed by means of special metallic closures, Fig. 3.11 shows the insulation inserts and metallic closure. Each closure had a central hole through it connected to a small diameter tube to enable the introduction of gas into, and out of the furnace. Argon gas was used as a inert atmosphere with a flow rate of 0.8 l/min during the sintering period and with a higher flow rate at the beginning of 5 l/min for two minutes to extract the residual air inside the tube [28,39]. The gas was fed through the small diameter tube, to one side of the furnace and removed using the small diameter tube at the other end of the furnace. The outlet was connected to a small diameter flexible tube which led to a fume hood. From Fig. 3.12 it can be seen that the samples were heated from room temperature to 1315°C in argon, using a ramp rate of 10°C per min, held at 1315°C for 45 minutes [27,48]. The samples were then cooled down using a ramp rate 5°C per min to minimize residual stresses [5]. Green compacts were put in the centre of the tube furnace in batches of two, and the machined samples were re-sintered in the tube furnace in batches of ten using the same sintering profile; Fig. 3.13 shows the re-sintered samples.

Fig. 3.9: Tube furnace.

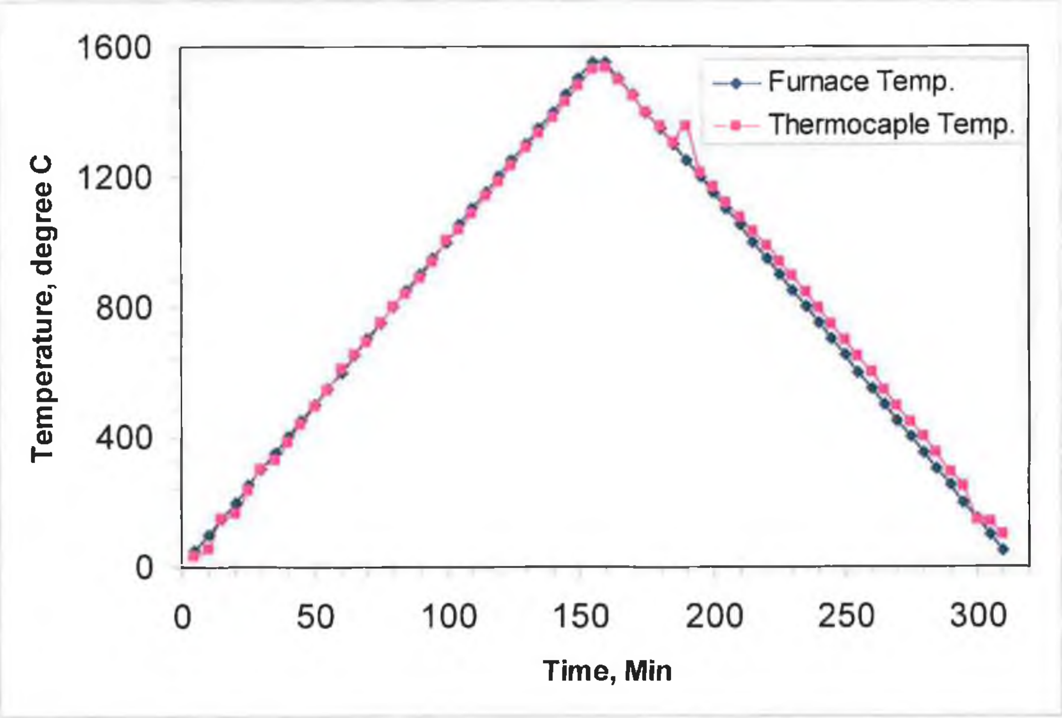

Fig. 3.10: The calibration curve [55].

Fig. 3.11: Insulation plugs and metallic plugs.

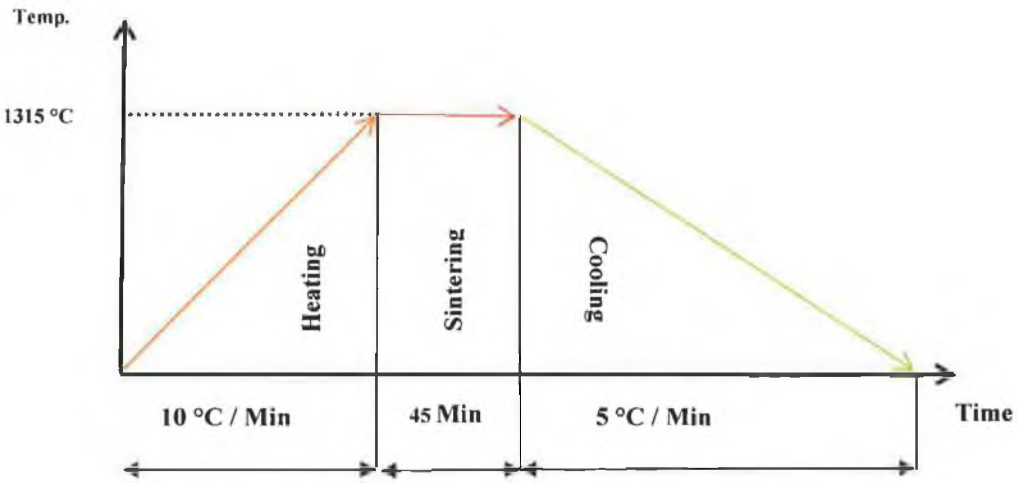

Fig. 3.12: Sintering profile.

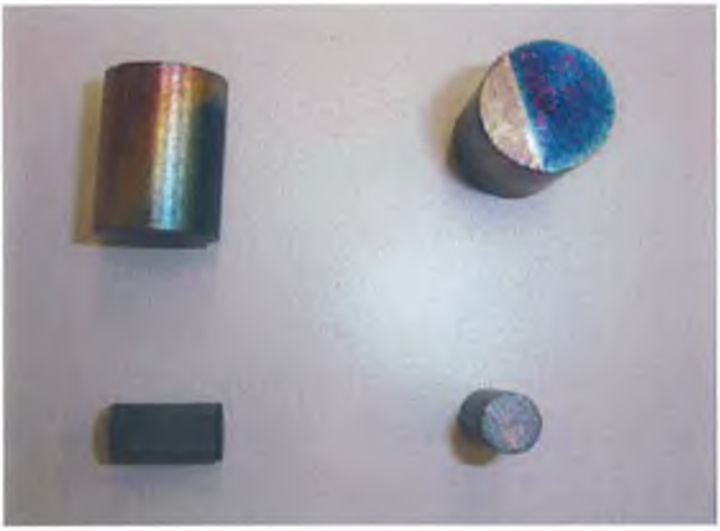

Fig. 3.13: Samples after re-sintering process.

3.6 Machining

After the first sintering of all the samples, it was decided to make the surface smooth by machining them before loading them into the pycnometer chamber; Fig. 3.14a shows the sample after the first sintering. All samples were machined using a CNC machine to the required dimensions for each subsequent test as shown in Fig. 3.14b. A high cutting speed and a low feed rate were used to obtain good surface finish which could be especially important with magnetic properties.

(a)

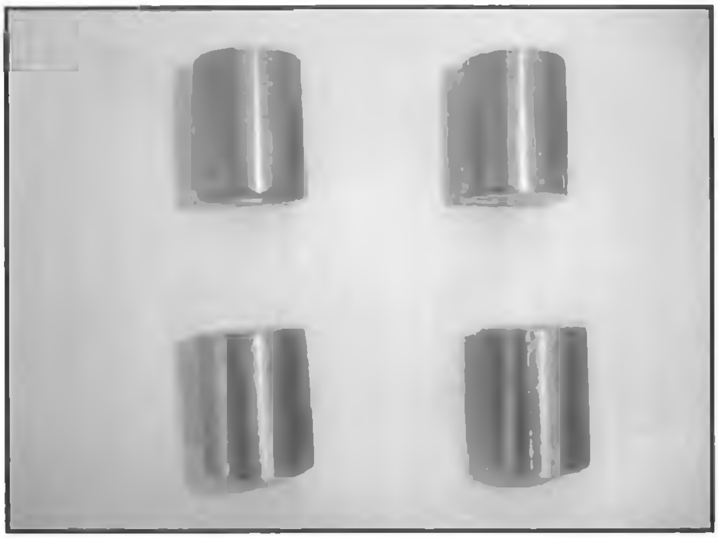

(b)

Fig 3.14: (a) Sample after first sintering and (b) after machining.

3.7 Compression Test

In this work samples were subjected to uniaxial compression tests to determine their compressive strength. Specimens with diameters of 8 mm and Length-to-diameter ratio (L/D) of 2.0 were used for this test [49]. The compression tests were carried out using an Instron Universal Testing machine model 4204, which is designed for testing materials in either tension or compression. The arrangements can be seen in Fig. 3.15. Before the operation of the machine, a load cell for a particular testing application (50 KN in this work) was selected and mounted to calibrate the equipment, the cross head speed was 5 mm/min. The specimens were placed in position as shown in Fig. 3.16 so that the applied load could be measured. Finally, the results were saved in an Excel file. Fig. 3.17 shows a specimen before testing and after 50% height reduction.

Fig, 3.15: Instron Universal testing machine.

Fig. 3.16: Specimen position.

Fig. 3.17: Specimen before testing and after 50% height reduction.

3.8 Metallographic Characterization and Microhardness Measurements

3.8.1 Sample preparation

Transverse sections were cut from all samples before and after the second sintering using a cutter with a coolant liquid shown in Fig. 3.18. The specimens were mounted in Bakelite using Buehler Simplimet 2000 Mounting Press shown in Fig.3.19. A hot-compression mounting procedure was followed to provide a hard mass, which allows fixing of the specimens during the following operations. Grinding was carried out for all specimens using a grinding and polishing wheel, a Buehler type Motopol 2000 shown in Fig. 3.20. The procedure involved starting coarser abrasive Silicon Carbide paper of 240 grain/cm^2 and finishing with the finest paper of 1200 grain/cm^2 for 4 min. the details are given in Table 3.3. Polishing was carried out in three stages using diamond suspensions with different grain sizes as described also in Table 3.3. After polishing, the specimens were cleaned thoroughly by cool running water and alcohol, and then dried. The specimens were etched using Nital (2% HNO_3 + 98 % ethanol) for 10 seconds to reveal the microstructure [50].

Fig. 3.18: Cutter.

Fig. 3.19: Hot mounting press.

Fig. 3.20: Buehler Motopol 2000 Semi-Automatic grinding and polishing wheel

Table 3.3: Grinding and polishing stages.

stage	Type	Size	Time (min)	speed (tr/min)	water
1	Silicon carbide paper	240 grain/cm²	4	150-200	watering
2	Silicon carbide paper	600 grain/cm²	4	150-200	watering
3	Silicon carbide paper	800 grain/cm²	4	150-200	watering
4	Silicon carbide paper	1200 grain/cm²	4	150-200	watering
5	diamond suspension	6 µm	5	250	wet before
6	diamond suspension	3 µm	5	250	wet before
7	diamond suspension	0.05 µm	5	250	wet before

3.8.2 Prepared specimen characterization

a) Microstructure

The microstructures of all specimens before and after the second sintering were examined by means of an optical microscope equipped with a video camera and shown in Fig. 3.21. In this work, two objective lenses were used with magnifications of 8X and 80X with an eye lens of 6X.

Fig. 3.21: Optical microscope.

b) Microhardness measurement

Microhardness measurements were carried out at room temperature with a PMT-3 microhardness tester shown in Fig. 3.22, and equipped with a diamond Vickers indenter. A load of 0.1 kg was applied for fifteen seconds and the size of the indentation was measured using a light microscope supplied as part of the microhardness tester. The Vickers hardness number is based on the force divided by the surface area of the indentation, as can be seen in Eq. 3.4 [49]. Five measurements were made at different positions for each sample ranging from near the centre of one face of the specimen to positions near the corners, and then the average of these five measurements was calculated.

$$HV = 1.8544 \times \frac{P}{d^2} \qquad 3.4$$

Where:

P: load in kgf.

d: indentation length in mm.

Fig. 3.22: Microhardness tester.

3.9 Magnetic Properties Measurements

A series of double sintered specimens were sent over to KJS Associates, Magnetic Instrumentation, Inc, USA for magnetic B vs. H testing. The specimens were cylindrical in shape. The following procedures were carried out:

1. The physical dimensions of each bar were measured and recorded.
2. A secondary (B) winding of #30AWG magnet wire was wound over a layer of 0.0508 mm insulation tape on each bar as shown in Fig. 3.23.
3. The bar under test was placed in the KJS Associates Model YOKE-100 test yoke and clamped using suitable adapters. A calibrated Hall probe was placed at the surface of the sample to measure the applied field H. The search coil

winding was connected to the system fluxmeter to determine the flux density in the sample.

4. Each sample was dynamically demagnetized prior to each test.
5. After demagnetizing, the bar specimen was magnetized to maximum applied field of approximately 1000 Oersted in the yoke fixture. Then the full four-quadrant B vs. H curve was measured at room temperature.
6. The data were analysed using a KJS Associates, Inc. Model SMT-600-5 computer automated soft magnetic hysteresigraph system and YOKE-100 test fixture, which complies with ASTM A773/A773M-01.
7. Data were sent back in form of pdf files and measured data points as .csv comma-separated-variables ASCII data files, which can be made compatible with most magnetic modelling programs.

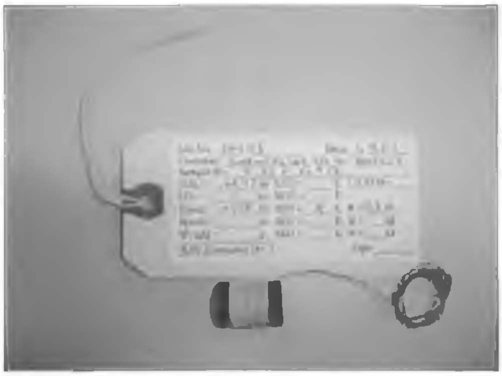

Fig. 3.23: Sample with magnet wire.

CHAPTER IV

FINITE ELEMENT METHOD

4. FINITE ELEMENT METHOD

The Finite Element Method (FEM) is a numerical procedure that was developed in the early 1950s as a tool to obtain solutions to a variety of problems in Engineering. However, Courant in 1943 has been credited with being the first person to develop the FEM, when he published a paper in early 1940 to investigate a torsion problem. Originally FEM was applied to steady state problems or static problems only. Quickly, its application was extended to time dependent problems involving linear or nonlinear characteristics which occur in the analysis of airplane wings. The formative years of its development were between the 1950's and the mid 1960's. At that stage FEM was available only as a large, general purpose software, running mainly on mainframe computers, which had a lower order of capability when compared to those in use now. Consequently, its availability was limited and its development was slow.

Nowadays, with the invention of high speed personal computers and the successful achievement of commercial software design, the commercial availability, application and use of FEM is made possible for different disciplines such as stress analysis, heat transfer and electromagnetism problems and for even more complicated shapes and problems[51, 52].

ANSYS is one of the most common FE computer packages. It was released for the first time in 1971. ANSYS is a comprehensive general-purpose FE computer program that contains over 100,000 lines of code. ANSYS has been the leading FEA program for well over the last 20 years. The current version of ANSYS includes computational structural dynamics, finite element solvers (FE), finite volume solvers for fluid dynamics (CFD), mesh-free particle solvers for high velocity, large deformation and fragmentation problems (SPH), and multi-solver coupling for multi-physics solutions including coupling between FE, CFD and SPH methods [51, 53].

4.1 Model Setup

To describe the analytical models clearly, they have been simplified to a basic profile model. For complete simulation, the profile is expanded through 360° and the force measurement is taken using this volume (Fig 4.1).

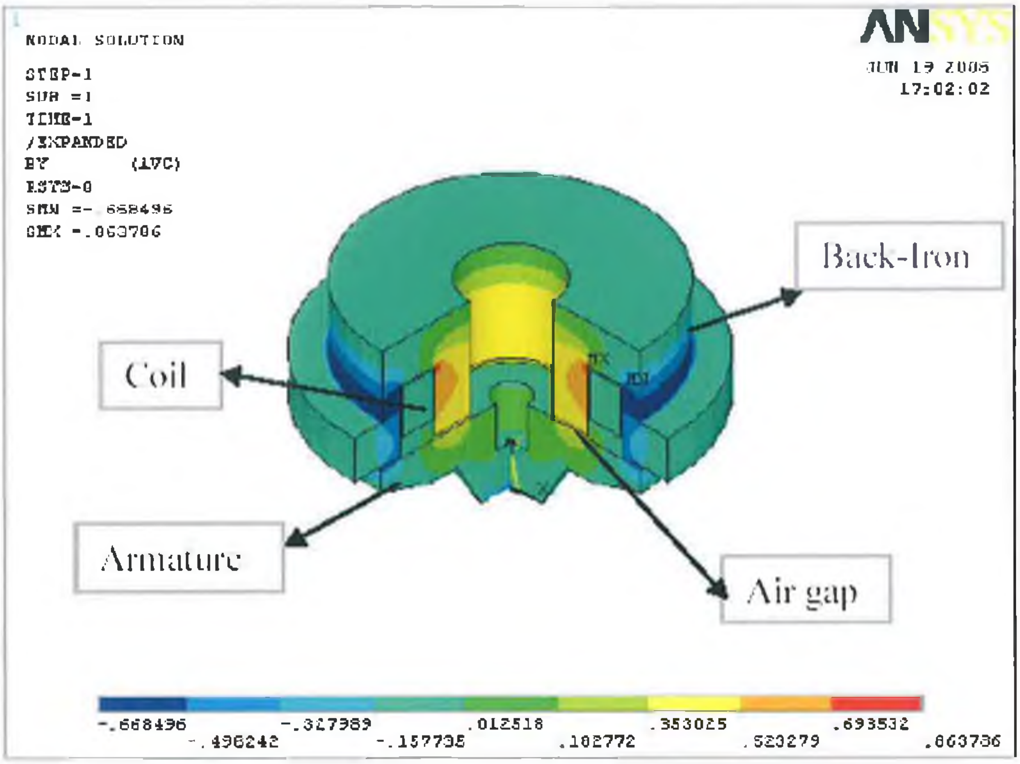

Fig. 4.1: Generated 3D model [40].

The ANSYS program uses Maxwell's equations as the basis for magnetic field analysis. The primary unknowns (degrees of freedom) that the finite element solution calculates are either magnetic potential or flux. Other magnetic field quantities are derived from these degrees of freedom, depending on the option that was chosen.

As described above, a solenoid actuator used in a common rail diesel injector was used for the analysis. The use of a 2-D axisymmetric model greatly reduces the modelling and analysis time compared to that of an equivalent 3-D model [53], and therefore this approach was adapted.

In this work, a system designed as PLANE 13 element was used. PLANE 13 elements have a 2-D magnetic field capability with limited coupling between the fields. The element is defined by four nodes with up to four degrees of freedom per node. The element has nonlinear magnetic capability for modelling B-H curves or permanent magnet demagnetization curves. The geometry is as shown in Fig. 4.2.

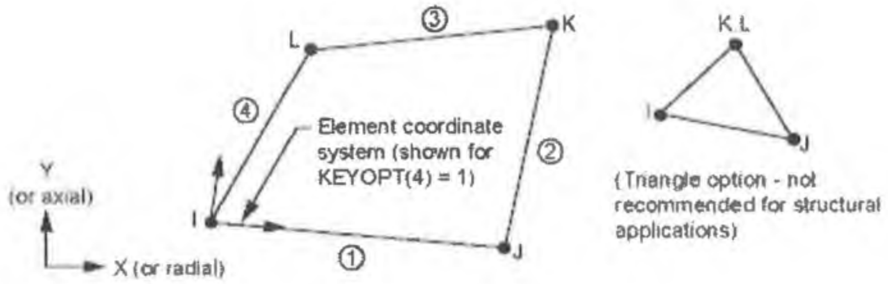

Fig. 4.2: PLANE13 Geometry [54].

The procedure for a static magnetic analysis, consisting of the following five main steps:

1. Define the physical environment.
2. Build and mesh the model.
3. Apply boundary conditions and loads.
4. Obtain the solution.
5. Review the results.

4.1.1 Define the physical environment

To define the physical environment the following steps were undertaken:

a. Specify the type of analysis as magnetic analysis.(magnetic node)
b. Define the element type(element 13)
c. Specify the materials properties: the ANSYS material's library contains data for several materials with magnetic properties. In the current model, the material's properties were introduced to the ANSYS as new material models. The magnetic properties were provided in the form of a B-H curve as shown in Fig.4.3. The same material was chosen for both back iron and the armature. The material properties for the air surrounding the

other components and coil were chosen assuming a constant relative permeability of 1.

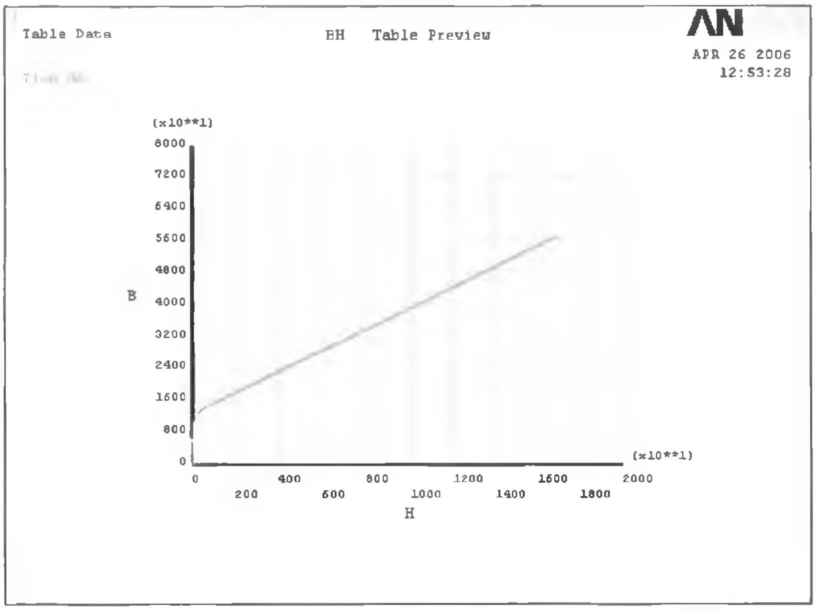

Fig.4.3: B-H curve.

4.1.2 Build and mesh the model

For the construction of the model in two dimensions, keypoints were chosen at all the corners of the two dimensional drawing of the parts and those points were joined together by lines as shown in Fig. 4.4. Areas were then created within these lines as shown in Fig. 4.5.

Then attributes were assigned to each area in the model (Attributes are the element types and options, element coordinates, and material properties). The model was meshed using the Meshing Attributes dialog box. Fig. 4.6 shows the meshed model.

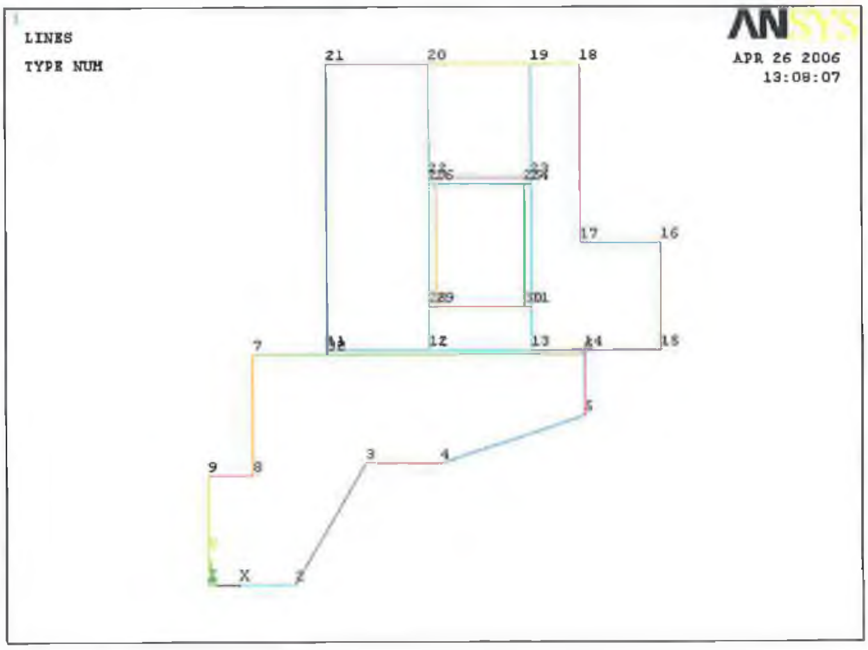

Fig. 4.4: Joining the keypoints by lines.

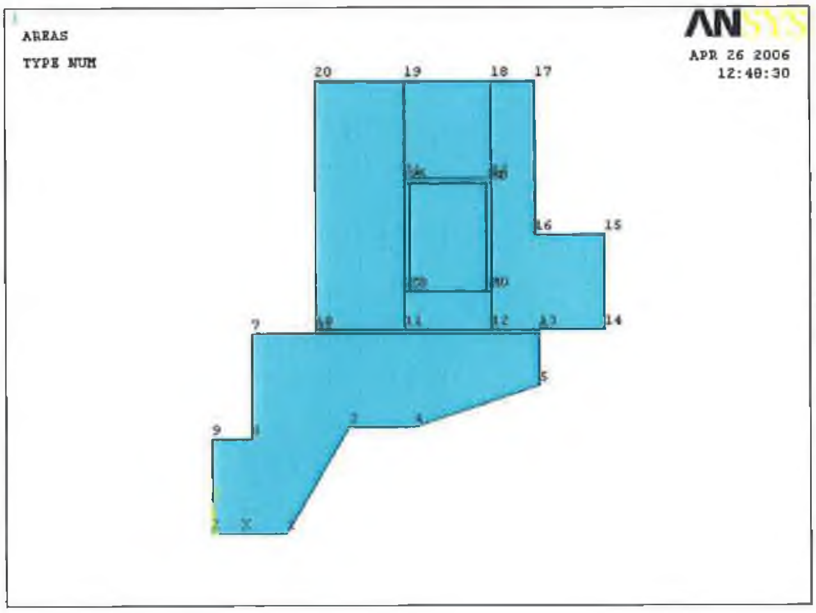

Fig. 4.5: Model construction.

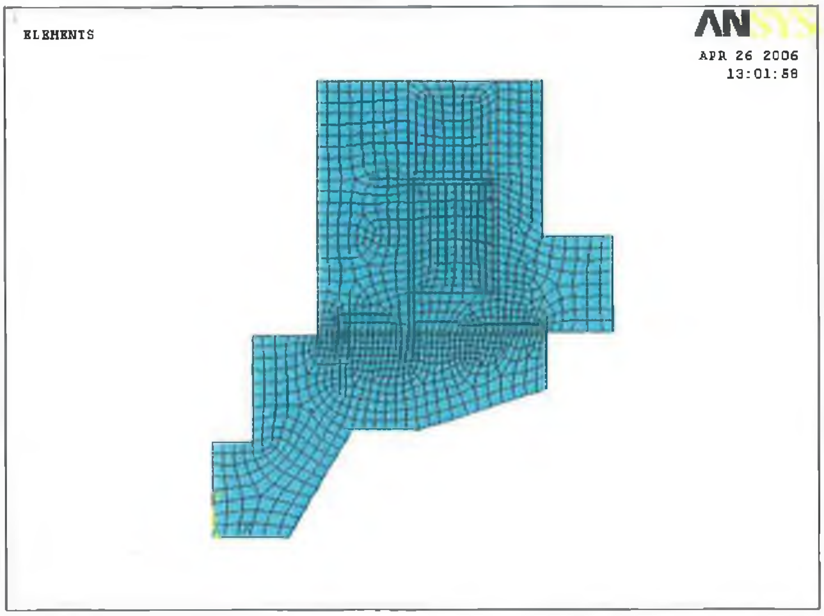

Fig. 4.6: Meshing the model.

4.1.3 Applying boundary conditions and loads

In this study the following boundary conditions were chosen:

a) Flag: The moveable part of the solenoid, the armature, was defined as the moveable part by using an option in the programme.

b) Boundary conditions: Boundary conditions were specified such that no flux escapes. The flux must travel parallel to the boundary lines set by the geometry of the system. This is shown in Fig. 4.7.

c) Excitation: In order to provide details of the excitation current to the model the data was required in the form of current density. The following formula was used to determine the current density. This is the amount of current flowing through an area of 1metre squared.

$$CurrentDensity = \frac{Current \times Turns}{Area} \qquad 4.1$$

Usually, the current density was applied directly to each area.

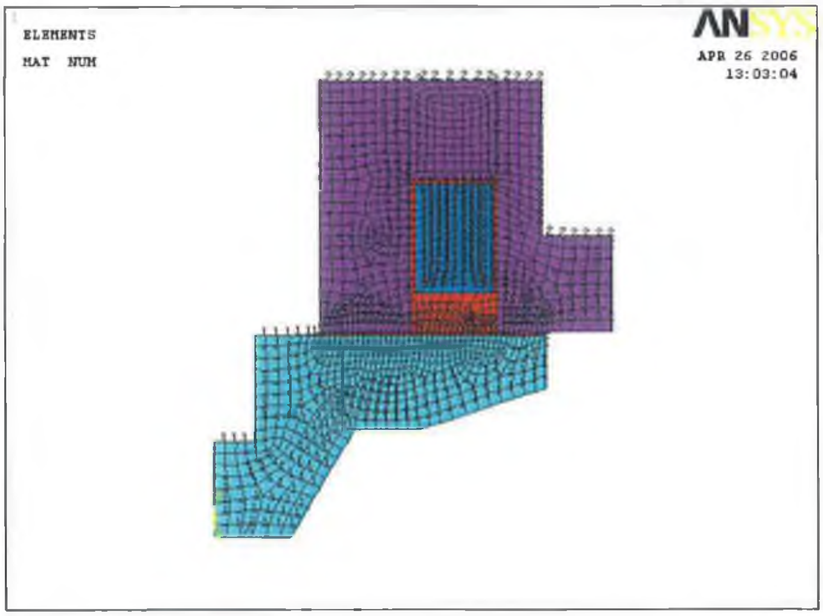

Fig. 4.7: Apply force boundary conditions

4.1.4 Solving the analysis

This section describes the tasks that were performed provide a solenoid to the 2-D static magnetic analysis problem. The magnetic solution options were specified and the solution procedure was initiated.

As the electromagnetic analysis proceeds, ANSYS computes convergence norms with corresponding convergence criteria for each equilibrium iteration. ANSYS considers a solution to be converged whenever specified convergence criteria are met. Convergence checking may be based on magnetic potential, magnetic field, or magnetic flux density

4.1.5 Reviewing results

Reviewing the solutions is made possible by opening the result file. A magnetic flux density plot is made available and the forces acting on the components can be read from the screen, as shown in Fig.4.8 and Fig.4.9. The magnetic flux densities were generated around the electrical coil.

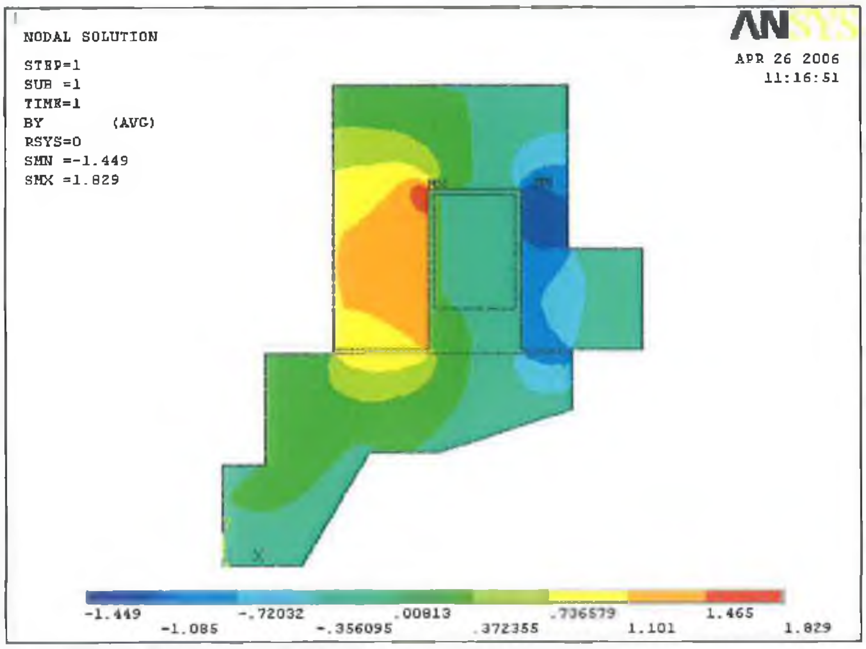

Fig 4.8: Magnetic Flux Density (B_{SUM}).

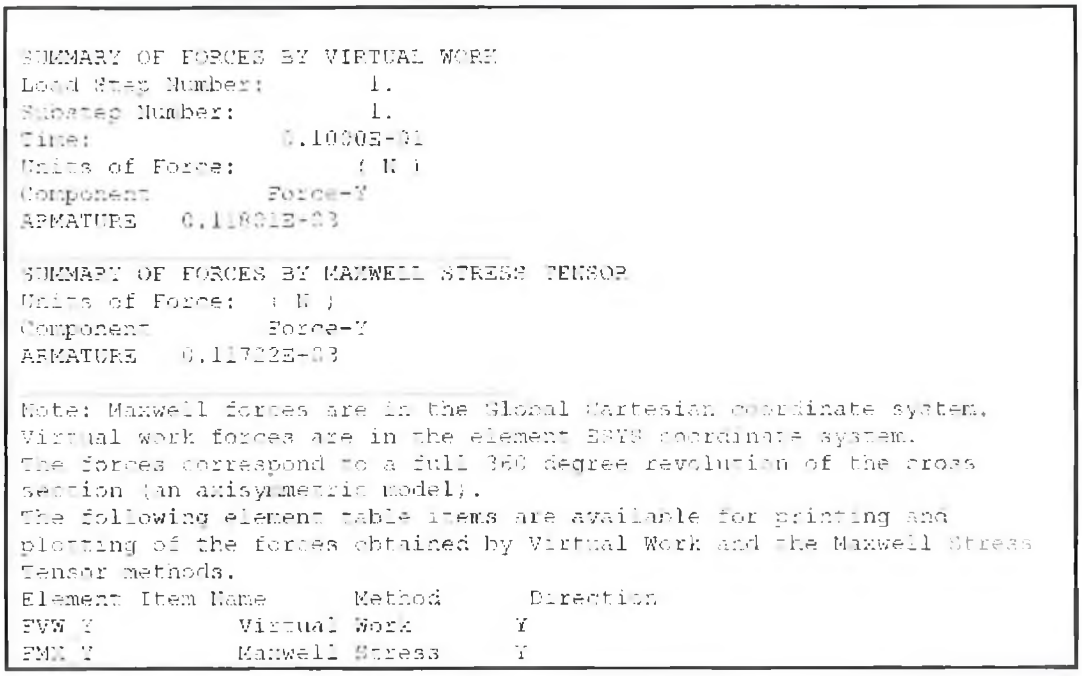

```
SUMMARY OF FORCES BY VIRTUAL WORK
Load Step Number:          1.
Substep Number:            1.
Time:                 0.10000E-01
Units of Force:           ( N )
Component            Force-Y
ARMATURE    0.11801E-03

SUMMARY OF FORCES BY MAXWELL STRESS TENSOR
Units of Force:   ( N )
Component            Force-Y
ARMATURE    0.11722E-03

Note: Maxwell forces are in the Global Cartesian coordinate system.
Virtual work forces are in the element ESYS coordinate system.
The forces correspond to a full 360 degree revolution of the cross
section (an axisymmetric model).
The following element table items are available for printing and
plotting of the forces obtained by Virtual Work and the Maxwell Stress
Tensor methods.
Element Item Name       Method       Direction
FVW Y           Virtual Work        Y
FMX Y           Maxwell Stress      Y
```

Fig. 4.9: Ansys force read out window.

CHAPTER V

EXPERIMENTAL RESULTS AND DISCUSSION

5. EXPERIMENTAL RESULTS AND DISCUSSION

In this chapter, the results of microstructural observations and the measurements of densities, mechanical properties, microstructural characterizations and magnetic properties are presented and discussed. These results were obtained from experiments following the procedures described earlier in chapter three.

5.1 Densification

5.1.1 Raw powder density measurements

A small volume pycnometer was used to measure the raw powders' density. This pycnometer was calibrated to ensure accurate results. The average measured densities for Silicon, Cobalt and Iron powders were 2.3515, 8.9311 and 7.8581 respectively. Values given by supplier were 2.330, 8.9 and 7.860 for Silicon, Cobalt and Iron powder respectively. The results show that the supplier's data sheet is quite accurate.

5.1.2 Theoretical density calculations

Theoretical density (TD) refers to a solid body containing no porosity. The theoretical densities for all mixed samples were calculated according to [47] Eq. 3.1. Eq. 3.2 and Eq. 3.3. Table 5.1 shows the sample numbers with the corresponding average weights percent, percentage volume fractions percent and theoretical densities.

Table 5.1: Elements percentage and theoretical densities for each sample.

Sample No.	Element Wt.%			Element volume fraction %			Theoretical density g/cc
	Si	Co	Fe	Si	Co	Fe	
1	1	-	99	3.265	-	96.735	7.678
2	2	-	98	6.384	-	93.616	7.507
3	3	-	97	9.367	-	90.933	7.342
4	-	1	99	-	0.881	99.119	7.868
5	-	3	97	-	2.649	97.351	7.887
6	-	5	95	-	4.426	95.574	7.906
7	1	1	98	3.269	0.861	95.870	7.687
8	1	3	96	3.277	2.588	94.135	7.706
9	1	5	94	3.285	4.324	92.391	7.723
10	1	7	92	3.292	6.068	90.640	7.741

5.1.3 Sintered density

As mentioned earlier, the current study aims to evaluate the magnetic properties of the developed soft magnetic materials. As it is well known that the higher the density the better the magnetic properties [6, 24], great attention was directed to achieving higher densities for all samples throughout, using high sintering temperatures, suitable sintering atmospheres and controlled sintering profiles [23, 25 29]. It was expected that this would result in high densities which were assumed in terms of being closer to the theoretical densities. After the first sintering operation which was described in chapter 3, the average densities varied from 91 % to 95 % of the theoretical density as presented in Table 5.2 and Table 5.3. In order to improve the densities further, double sintering of all the samples was performed [26 and 27]. Also a slow cooling rate was used to minimize the cooling residual stress [5, 39]. It is clear from Tables 5.2 and 5.3 that the average densities for all samples after the second sintering operation were improved remarkably and varied between 96 % and 98% with an increment ranging between 1.58% and 6.35%. Three different specimens with the same composition were used to determine the density before and after the first sintering of each sample. The density was measured five times for each specimen and the arithmetic average D_{ij} was calculated. Then an overall average was calculated from the three arithmetic averages for each sample using Eq. 5.1.

$$\text{O. Average}_i = \frac{D_{i1} + D_{i2} + D_{i3}}{3}, \quad i = 1, 2 \ldots 10 \qquad 5.1$$

Where:

D_{ij} : Arithmetic average of five measured densities for sample number i.

O. Average i: Overall average for sample number i, calculated from the averages of three different specimens of the same composition.

Table 5.2: Densities after first and second sintering for Fe-Si & Fe-Co alloy.

Sample NO.		First Sintering		Second Sintering		% of increase
		Measured Density g/cc	% of TD	Measured Density g/cc	% of TD	
1	$D_{1.1}$	7.1112	92.6179	7.5381	98.1779	6.0032
	$D_{1.2}$	7.2014	93.7927	7.5317	98.0946	4.5866
	$D_{1.3}$	7.1452	93.0607	7.5291	98.0607	5.3728
O. Average₁		**7.1526**	**93.1571**	**7.5330**	**98.1111**	**5.3209**
	$D_{2.1}$	7.1383	95.0886	7.2518	96.6005	1.5900
	$D_{2.2}$	7.1492	95.2338	7.2234	96.2222	1.0379
	$D_{2.3}$	7.0963	94.5291	7.2462	96.5259	2.1124
O. Average₂		**7.1279**	**94.9505**	**7.2405**	**96.4495**	**1.5801**
3	$D_{3.1}$	7.1211	96.9913	7.2434	98.6570	1.7174
	$D_{3.2}$	7.1462	97.3332	7.2856	99.2318	1.9507
	$D_{3.3}$	7.1128	96.8782	7.2518	98.7715	1.9542
O. Average₃		**7.1267**	**97.0676**	**7.2603**	**98.8868**	**1.8742**
4	$D_{4.1}$	7.1857	91.3282	7.6348	97.0361	6.2499
	$D_{4.2}$	7.1754	91.1973	7.6525	97.2611	6.6491
	$D_{4.3}$	7.2015	91.5290	7.6461	97.1797	6.1737
O. Average₄		**7.1875**	**91.3515**	**7.6445**	**97.1590**	**6.3573**
5	$D_{5.1}$	7.1835	91.0803	7.5624	95.8844	5.2746
	$D_{5.2}$	7.2543	91.9779	7.5596	95.8489	4.2085
	$D_{5.3}$	7.2488	91.9082	7.6021	96.3877	4.8739
O. Average₅		**7.2289**	**91.6555**	**7.5747**	**96.0403**	**4.7841**
6	$D_{6.1}$	7.1902	90.9461	7.6534	96.8050	6.4421
	$D_{6.2}$	7.2014	91.0878	7.6480	96.7367	6.2016
	$D_{6.3}$	7.2537	91.7493	7.6625	96.9201	5.6357
O. Average₆		**7.2151**	**91.2611**	**7.6546**	**96.8206**	**6.0919**

Table 5.3: Densities after first and second sintering for Fe-Si-Co alloy.

Sample No.		First Sintering		Second Sintering		% of increase
		Measured Density g/cc	% of TD	Measured Density g/cc	% of TD	
7	$D_{7.1}$	7.0760	92.0515	7.5104	97.7026	6.139
	$D_{7.2}$	7.1021	92.3910	7.5074	97.6636	5.707
	$D_{7.3}$	7.1485	92.9947	7.5224	97.8587	5.230
O. Average		**7.1089**	**92.4791**	**7.5134**	**97.7416**	**5.691**
8	$D_{8.1}$	7.0786	91.8583	7.5146	97.5162	6.159
	$D_{8.2}$	7.1245	92.4539	7.4729	96.9751	4.890
	$D_{8.3}$	7.1546	92.8445	7.5273	97.6810	5.209
O. Average		**7.1192**	**92.3856**	**7.5049**	**97.3908**	**5.418**
9	$D_{9.1}$	7.2940	94.4452	7.5099	97.2407	2.960
	$D_{9.2}$	7.2657	94.0787	7.5284	97.4803	3.616
	$D_{9.3}$	7.3218	94.8051	7.5227	97.4064	2.744
O. Average		**7.2938**	**94.4430**	**7.5203**	**97.3758**	**3.105**
10	$D_{10.1}$	7.2834	94.0886	7.5339	97.3246	3.439
	$D_{10.2}$	7.3256	94.6338	7.4705	96.5056	1.978
	$D_{10.3}$	7.2748	93.9775	7.5481	97.5081	3.757
O. Average		**7.2946**	**94.2333**	**7.5175**	**97.1128**	**3.056**

5.2 Compression Test

The compression tests were carried out for all samples after the re-sintering process. The tests were continued until the specimen length reduced to 50% of its original length as shown in Fig. 3.14. The average of two compression loads regard to produce a 50% reduction in length for each of the samples was calculated and presented in Table 5.4. It is clear from these results that the compression strength increased remarkably for samples 1-2 as the silicon content increased from 1 % to 2% and increased slightly as the silicon percent is increased further to 3 %. This is due to the fact that increasing the silicon content tends to increase the hardness which is reflected in a hardened structure as described in [2, 5 and 31]. On the other hand, as the cobalt percentage increases the compression strength decreases slightly as presented in Table 5.4 for samples 4 to 6. For the ternary alloy system, the compression strength was almost the same for samples 7 to 10 as shown in Table 5.4.

Table 5.4: Compression test results.

Sample No.	Compression load at 50 % reduction in length, kN		Average compression load kN	Average compression strength MPa
	1	2		
1	37.583	37.248	37.416	744.294
2	46.630	45.986	46.308	921.188
3	48.986	49.365	49.176	978.325
4	28.483	28.483	28.483	566.598
5	29.570	26.201	27.886	554.716
6	26.376	24.805	25.590	509.057
7	34.214	34.080	34.147	679.276
8	33.396	34.268	33.832	673.002
9	34.818	33.704	34.261	681.546
10	35.932	36.094	36.013	716.391

5.3 Microstructural Characterization

5.3.1 Microstructure

The microstructure of all the samples was observed using an optical microscope before and after the re-sintering operation. Transverse sections were cut from all specimens for metallographic characterization by following the procedure described in chapter 3. Fig. 5.1 shows the effect of the Silicon percentage on the microstructure, Fig. 5.1 a, c and e reveal the microstructures of the samples with Silicon contents of 1%, 2% and 3% respectively after first sintering. It is clear that the Silicon tends to form black flakes, while the white areas are ferrite grains; these figures also indicate that the black flakes increase as the Silicon percentage increases. Fig. 5.1 b, d and f reveal the microstructures of the same samples but after re-sintering. It is clear that the Silicon distribution becomes more homogeneous and the Silicon tends to form nodular grains. The results are in a good agreement with the results obtained by Rulz and Jansson [34, 36], which indicate that iron-Silicon alloys need higher sintering temperatures, 1260 -1315 °C, and longer sintering times, 45-60 min, to homogenize the Silicon content.

Fig. 5.2 shows the effect of the Cobalt content on the microstructure, Fig. 5.2 a, c and e shows the microstructure of samples containing 1%, 3% and 5% Cobalt respectively after the first sintering. It is clear that the microstructure consists of predominantly ferrite (white) and Cobalt flakes (dark) regions. The percentage of these dark regions increases as the Cobalt content increases. Fig. 5.2 b, d and f reveal the microstructure of the same samples but after the application of double sintering. It is clear that after this process, the distribution of the dark regions becomes more homogenous, and most of the dark flake shapes changed to a nodular shape.

Similarly, Fig. 5.3 a, c, e and g show a series of ternary alloy systems of Fe-Co-Si with 1% Si content and 1%, 3%, 5% and 7% cobalt contents. It is clear that the microstructure consists of two regions, the white zones represent predominantly ferrite grains and the dark flakes represent the Cobalt and Silicon grains. In this study, there was no attempt to distinguish between the cobalt flakes and the Silicon ones, since this requires more sophisticated techniques such as X-Ray diffraction techniques. Fig. 5.3 b, d, f and h reveal the microstructure of the same samples of the ternary alloys but after the application of double sintering. It is evidence that the dark flakes have become smaller in size and are well distributed in the cross-section.

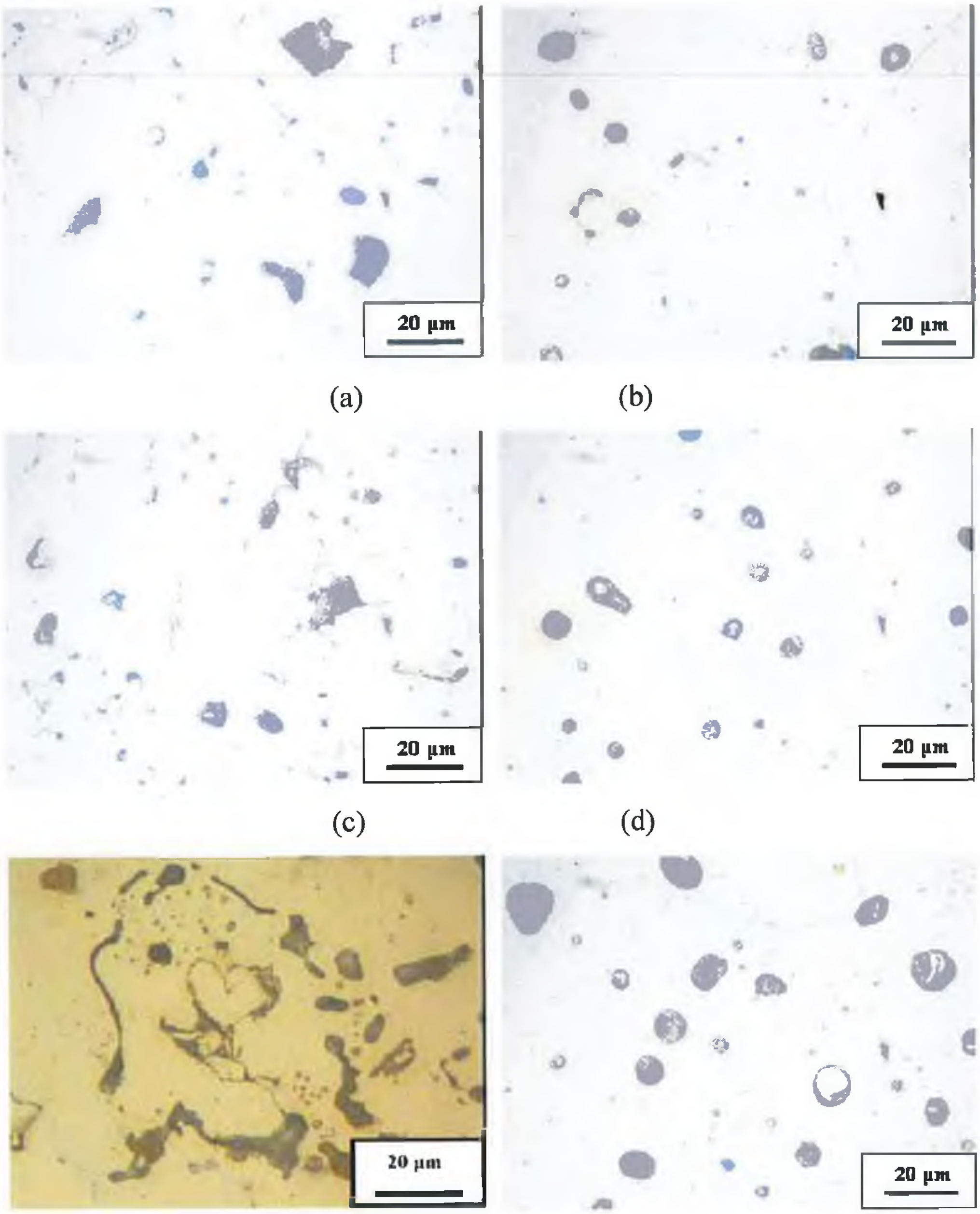

(a) (b)

(c) (d)

(e) (f)

Fig. 5.1: Micrographs showing the microstructures of Fe-Si alloys, (a), (c) and (e) 1%, 2% and 3 %Si alloys respectively after the first sintering. (b), (d) and (f) the 1 %, 2% and 3% Si respectively after re-sintering.

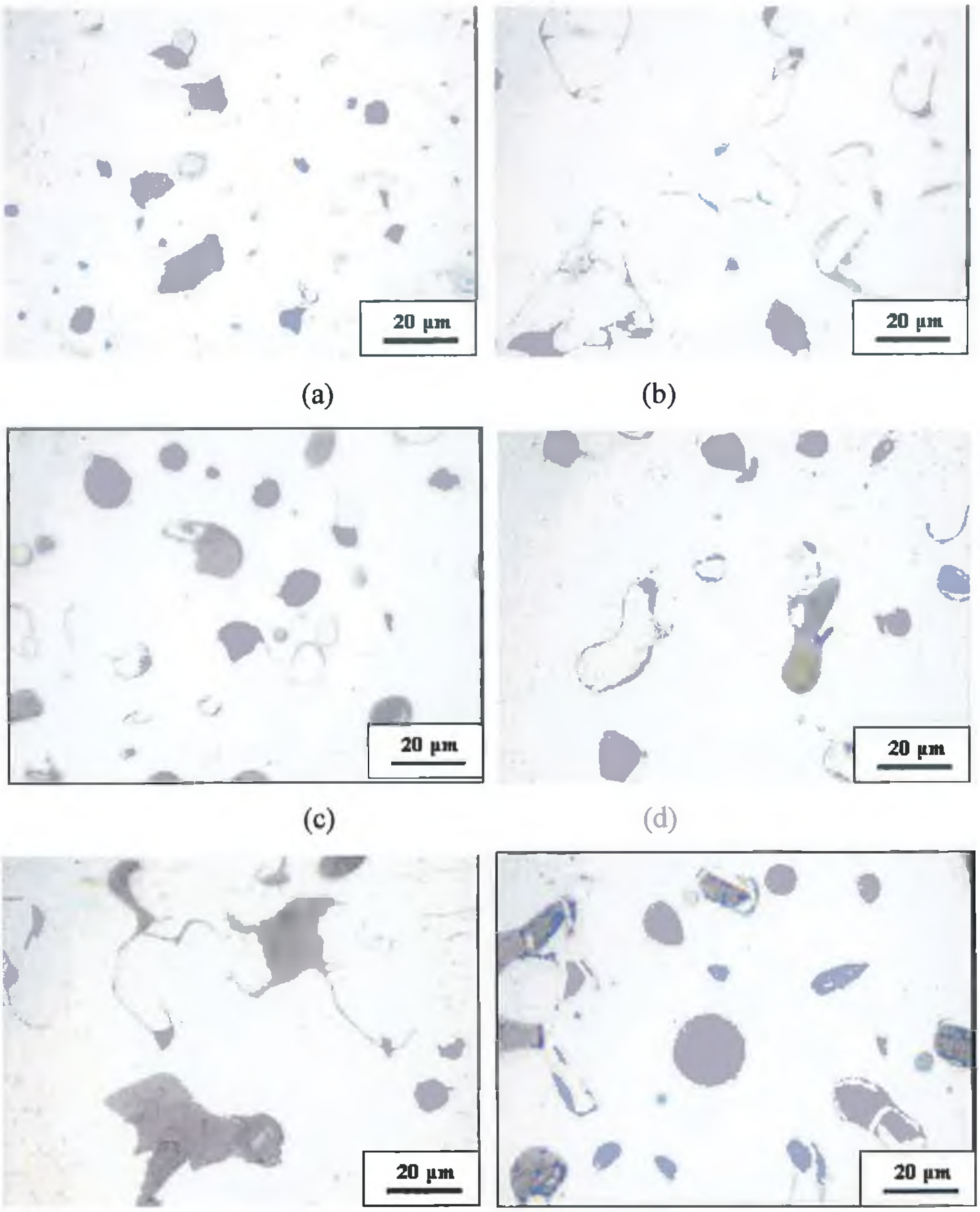

(a) (b)

(c) (d)

(e) (f)

Fig. 5.2: Micrographs showing microstructures of Fe-Co alloys, (a), (c) and (e) 1%, 3% and 5 %Co alloys respectively after the first sintering. (b), (d) and (f) the 1 %, 3% and 5 Co respectively after re-sintering.

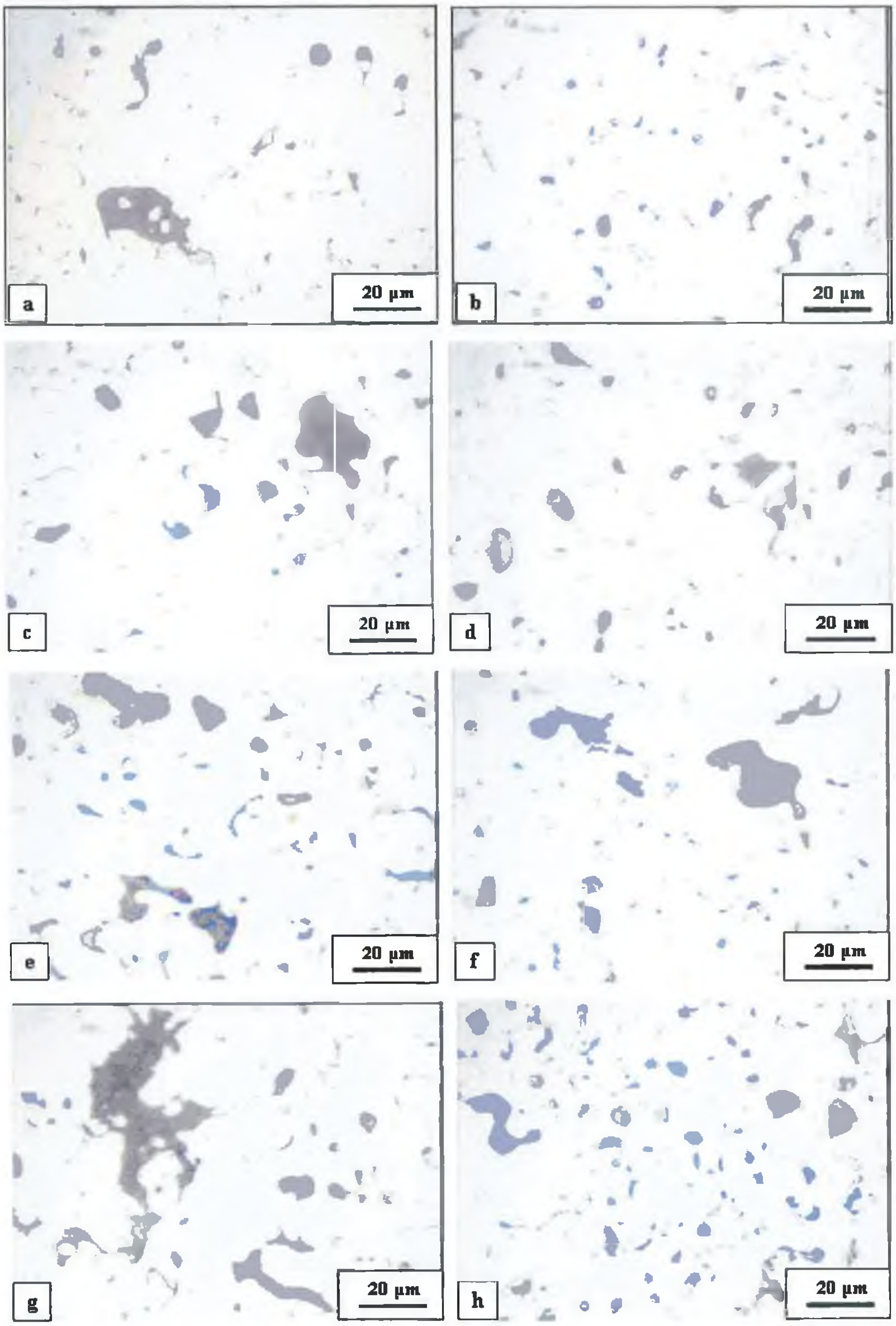

Fig. 5.3: Micrographs showing microstructures of Fe-Co-Si alloys, (a), (c), (e) and (g) consists of 1% Si and 1%, 3%, 5% and 7 % Co respectively after the first sintering. (b), (d), (f) and (h) the same samples but after re-sintering.

5.3.2 Microhardness

Vickers microhardness tests were carried out on the samples which had been prepared for metallographic characterization. Fig. 3.21 shows the Vickers microhardness tester used in this investigation; it uses a load of 0.1 kg applied according to ASTM standards for iron and steel alloys. At least five measurements were recorded for each sample before and after re-sintering. Then an arithmetic average of these five measurements was calculated for all tested samples. These averages were plotted on different graphs to show the effect of each alloying element on the microhardness. Fig. 5.4 shows the effect of Silicon content on the microhardness before and after the second sintering. There is evidence that the microhardness increases as the Silicon percentage increases. These results are in good agreement with that published in [2 and 5]. From Fig. 5.4 it is noticeable that the microhardness number is higher after the re-sintering for each of the samples. This trend is related to the fact that there is an increase in the sample density after the double sintering.

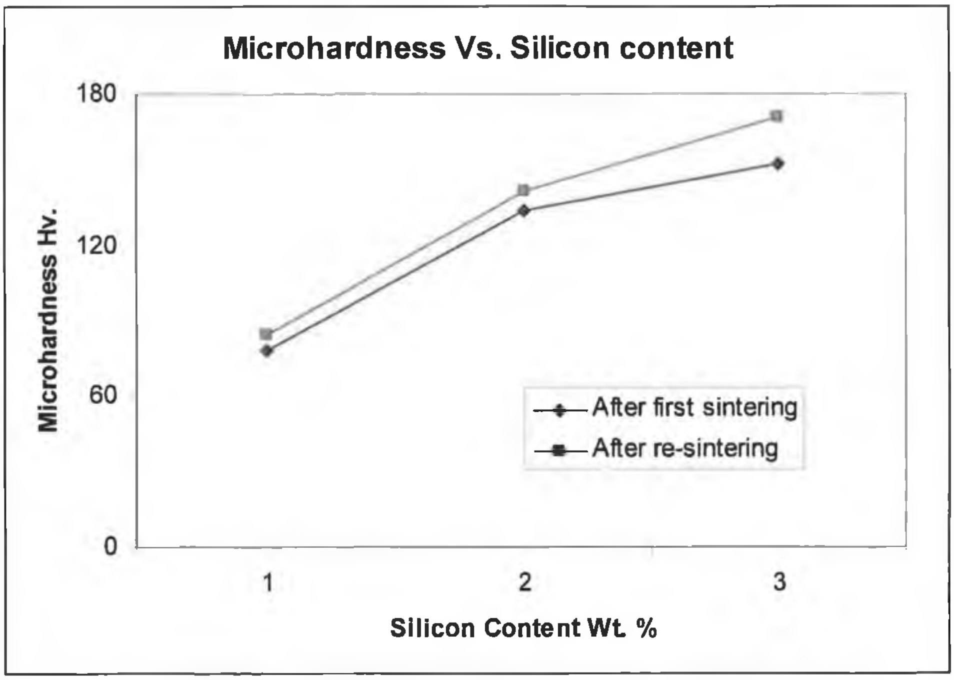

Fig. 5.4: Effect of Silicon content on the microhardness before and after re-sintering.

Similarly, Fig. 5.5 and Fig. 5.6 show the effect of Cobalt percentage on the microhardness for the binary and ternary alloys. It is clear that the Cobalt has no overall effect on the microhardness in both Fe-Co and Fe-Co-Si alloys. As the Cobalt content increases the microhardness decreases slightly. As above, the microhardness numbers of the re-sintered samples are higher than the samples of the same composition after only the first sintering. This can be attributed to the increase in the samples density [2, 5 and 6]. Comparing Fig. 5.5 and Fig. 5.6, there is evidence that the microhardness is higher in the ternary alloy system especially for low Cobalt content. This is due to the fact that the ternary alloy system consists of 1% Silicon which tends to increase the microhardness as discussed above.

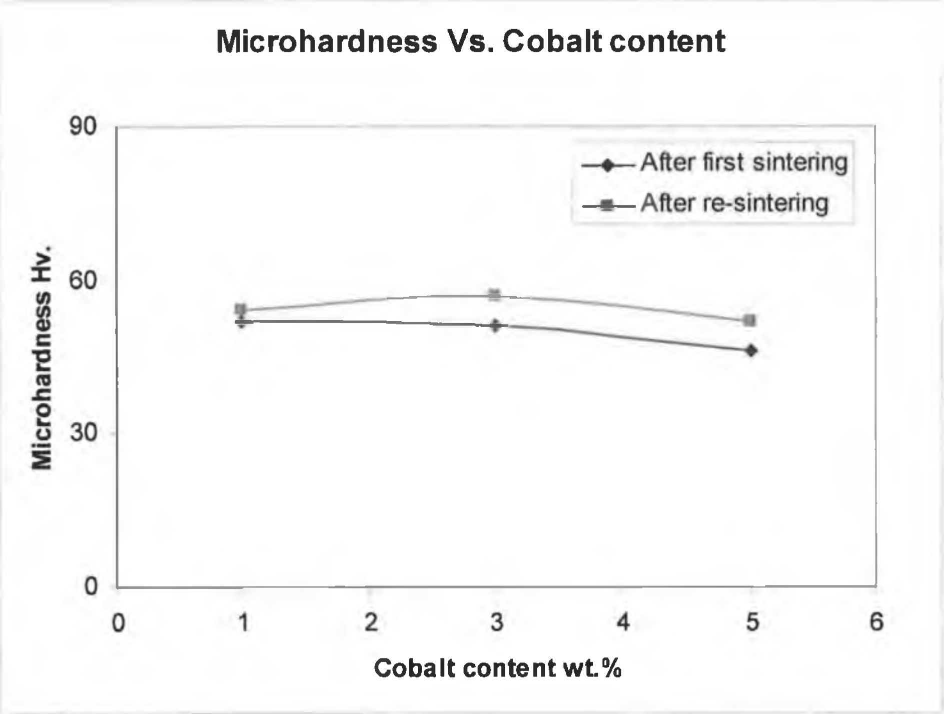

Fig. 5.5: Effect of Cobalt content on the microhardness before and after re- sintering.

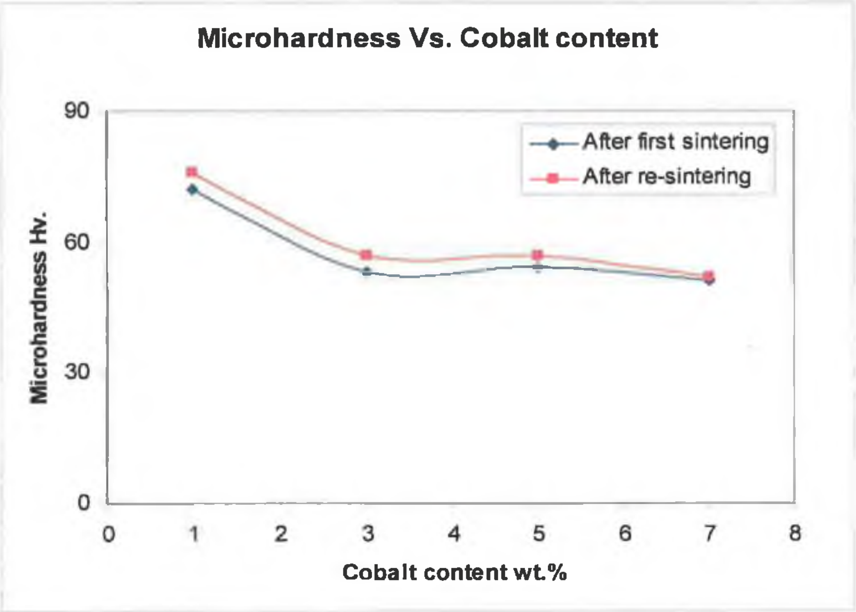

Fig. 5.6: Effect of Cobalt content on the microhardness before and after re-sintering for the ternary alloys.

5.4 Soft Magnetic Properties

DC magnetic B vs. H testing on the cylindrical samples were completed by KJS Associates Inc. according to ASTM A773/A773M-01 standard test. This has been described in chapter 3. Each sample was identified by a KJS in-house catalogue number as presented in Table 5.5. Fig. 5.7 shows a photograph of some tested samples.

Fig. 5.7: Photograph of some tested cylindrical samples with coils.

Table 5.5: KJS in-house catalogue numbers.

KJS ID	Customer sample ID
MS14671	Sample 1, 1 % Si 99% Fe
MS14672	Sample 2, 2 % Si 98% Fe
MS14673	Sample 3, 3 % Si 97% Fe
MS14674	Sample 4 , 1% Co 99% Fe
MS14675	Sample 5 , 3% Co 97% Fe
MS14676	Sample 6, 5 % Co 95% Fe
MS14677	Sample 7, 1% Co 1 % Si 98% Fe
MS14678	Sample 8 , 3% Co 1 % Si 96% Fe
MS14679	Sample 9 , 5% Co 1 % Si 94% Fe
MS14680	Sample 10, 7% Co 1 % Si 92% Fe

5.4.1 Si-Fe samples

For the first three samples the magnetic test results indicate that the higher the Silicon percentage the better the soft magnetic properties, as can be seen in Table 5.6 and in the hysteresis loops shown in Fig. 5.11. There is evidence from Table 5.6 that as the Silicon percentage increases the maximum permeability increases from 715 to 1102, while the Remanence B_r decreases from 5792 to 4108 G and the coercivity decreases from 3.7 to 2.08 Oe. These results show that the Silicon has a positive effect on the soft magnetic properties. The trends in the results are in a good agreement with the results presented in the literature, but it is also reported that the material will be extremely brittle as stated in [36, 38 and 39]. Full magnetic results for Si-Fe alloys are presented in appendix A.

Table 5.6: The magnetic test results for the first three samples.

Property, unit \ Sample No.	1	2	3
Max. measured B, G	15351	19606	19551
Max. measured H, Oe	1040	1033	1055
Remanence B_r, G	5792	5069	4108
Coercive field Hc, Oe	3.7	2.34	2.08
Max. permeability μmax	715	1098	1102
B @ Max. permeability, G	5364	7759	7267
H @ Max. permeability, Oe	7.505	7.065	6.592

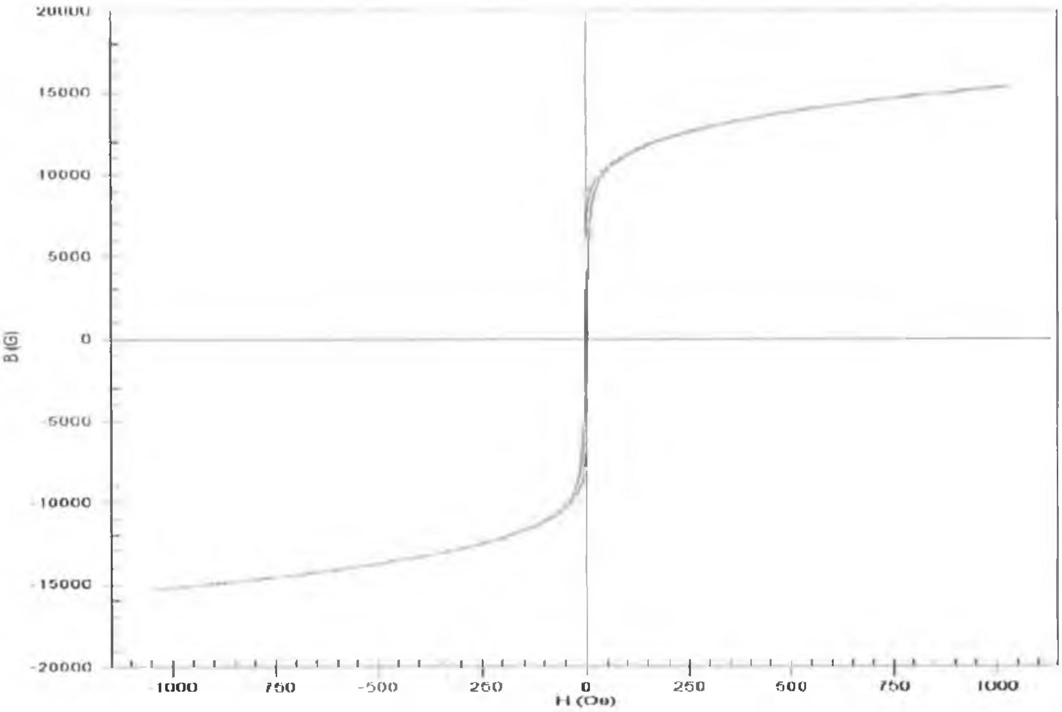

Fig. 5.8: Hysteresis loop for 1 %Si.

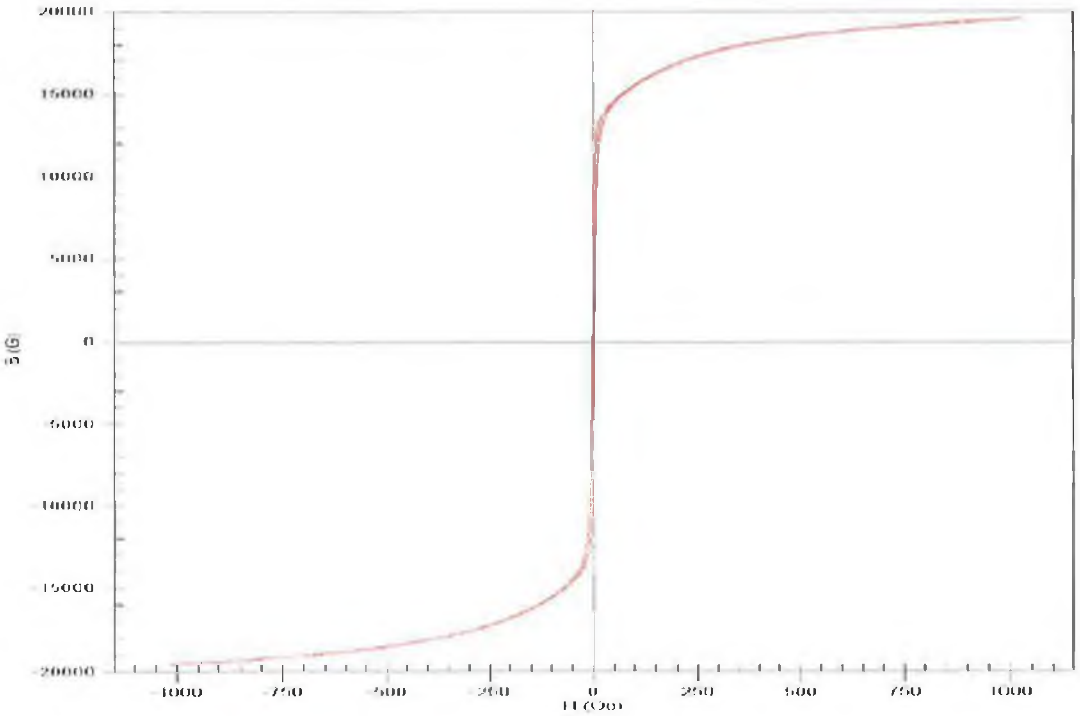

Fig. 5.9: Hysteresis loop for 2 %Si.

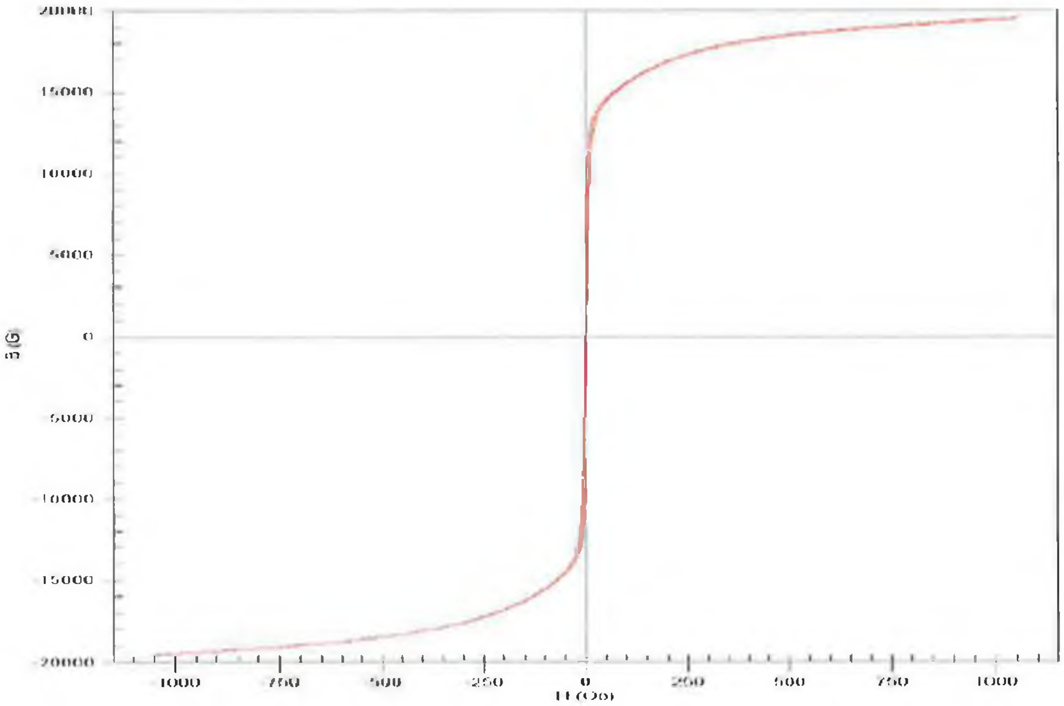

Fig. 5.10: Hysteresis loop for 3 %Si.

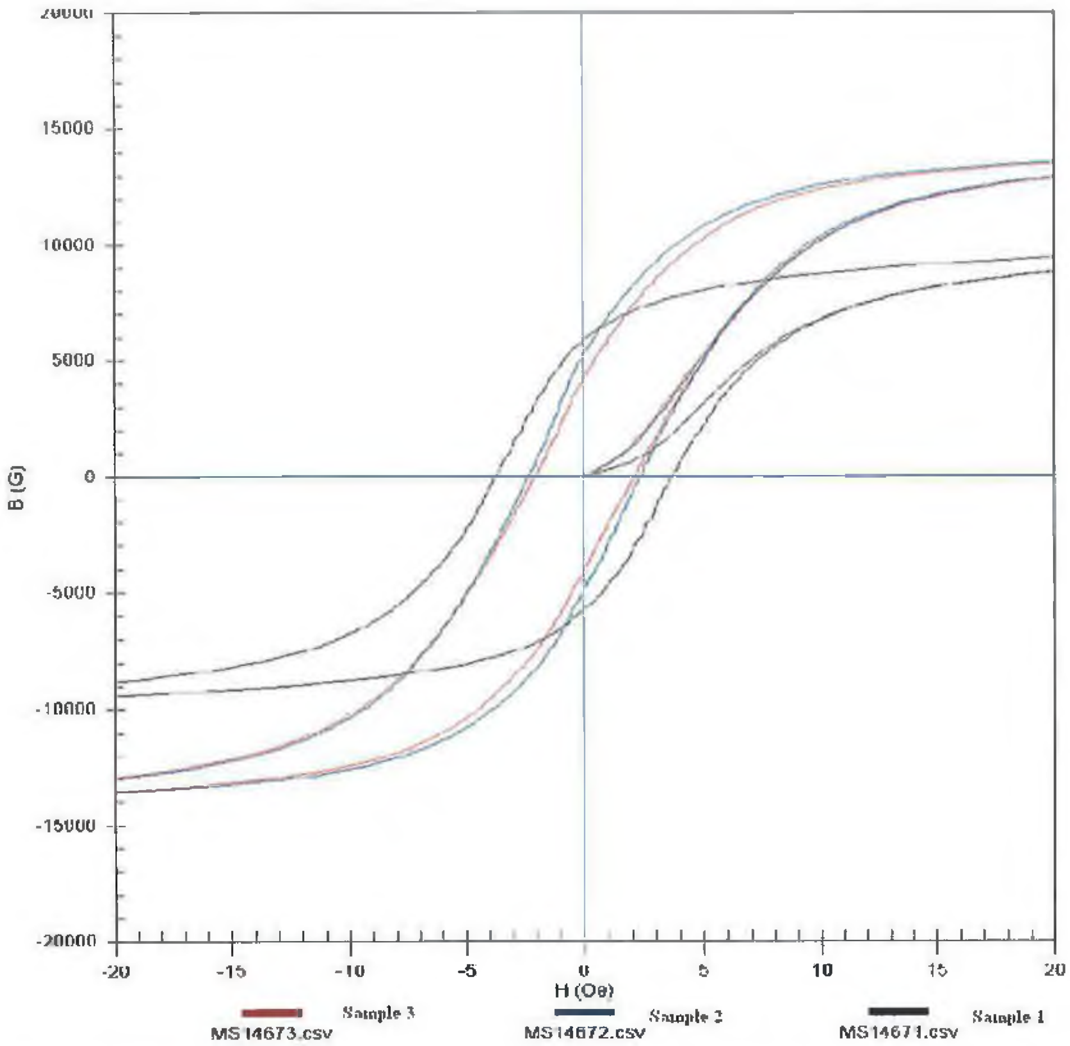

Fig. 5.11: Three hysteresis loops of samples 1, 2 and 3, at a higher magnification.

5.4.2 Co-Fe samples

The results indicate that alloying iron with Cobalt (samples 4 to 6) improves its soft magnetic properties up to certain Cobalt percentage then the alloy becomes harder in terms of its magnetic properties as can be seen in Table 5.7. The typical hysteresis loops of these samples are presented in Figs. 5.12 to 5.15. There is evidence that as the Cobalt percent increases from 1% to 3% the maximum permeability increases from 885 to 10550. Whilst, the remanence or the residual magnetism decreases from 6155 G to 5407 G and the coercivity decreases from 3.1 to 2.42 Oe. As the percentage of Cobalt is further increased to 5% the results show that the maximum permeability decreases to 701 and coercive force increases to 2.7 Oe, but the remanence decreases to 3639 G. Appendix B presents full magnetic properties of the Co-Fe alloys.

Table 5.7: The magnetic test results for the samples No. 4-6.

Sample No. Property, unit	4	5	6
Max. measured B, G	15703	16185	15560
Max. measured H, Oe	1028	1033	1041
Remanence B_r, G	6155	5407	3639
Coercive field Hc, Oe	3.1	2.42	2.7
Max. permeability μmax	885	1055	701
B @ Max. permeability, G	5935	5915	3667
H @ Max. permeability, Oe	6.708	5.609	5.228

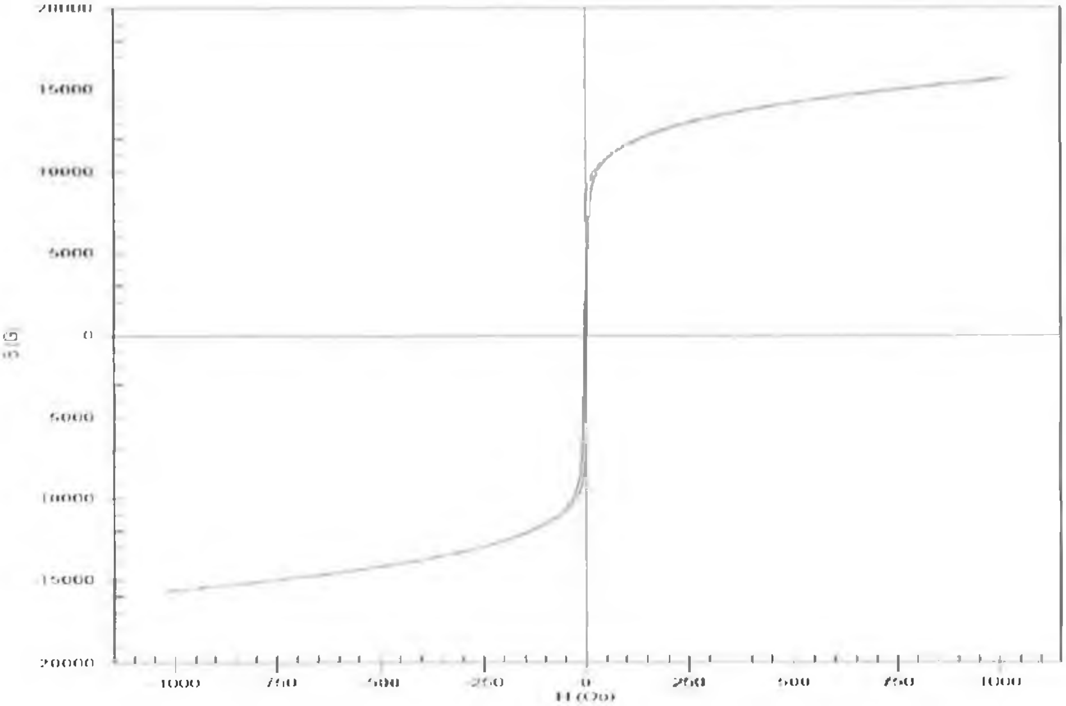

Fig. 5.12: Hysteresis loop for 1 % Co.

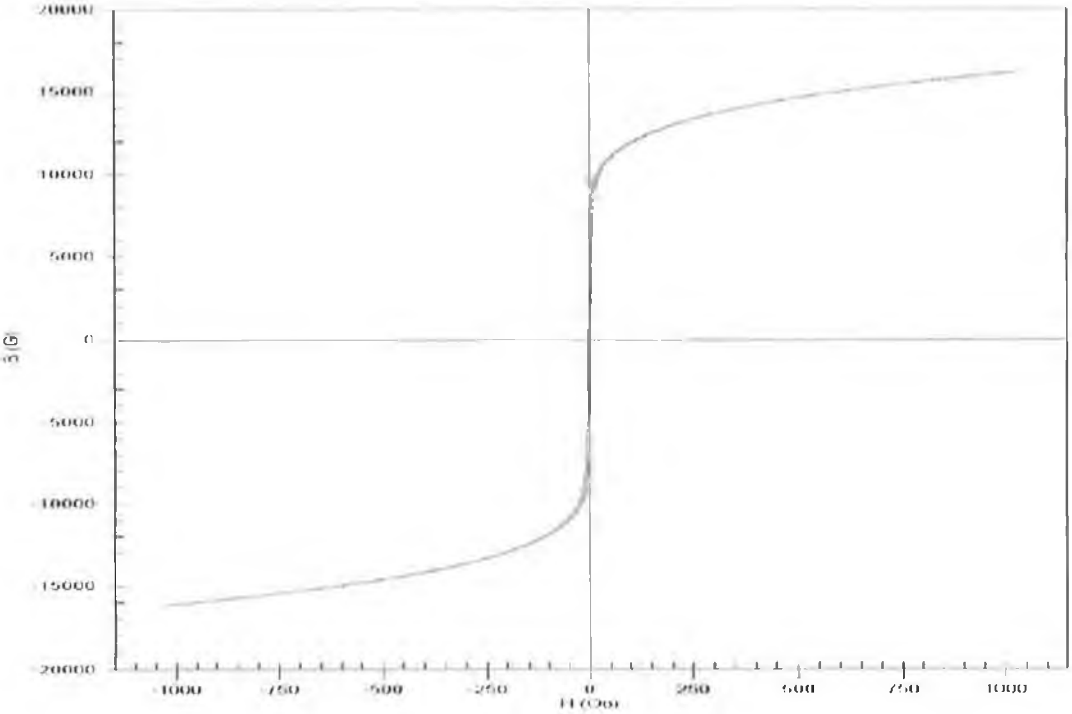

Fig. 5.13: Hysteresis loop for 3 % Co.

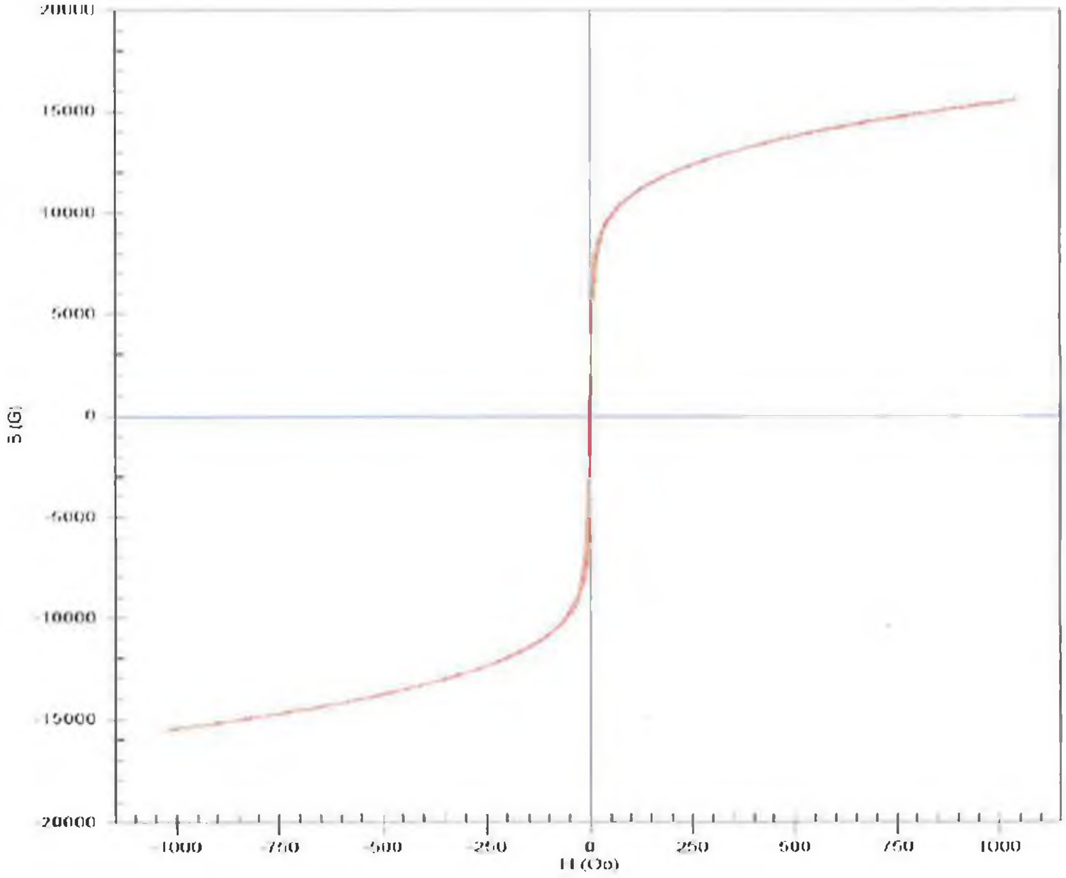

Fig. 5.14: Hysteresis loop for 5 % Co.

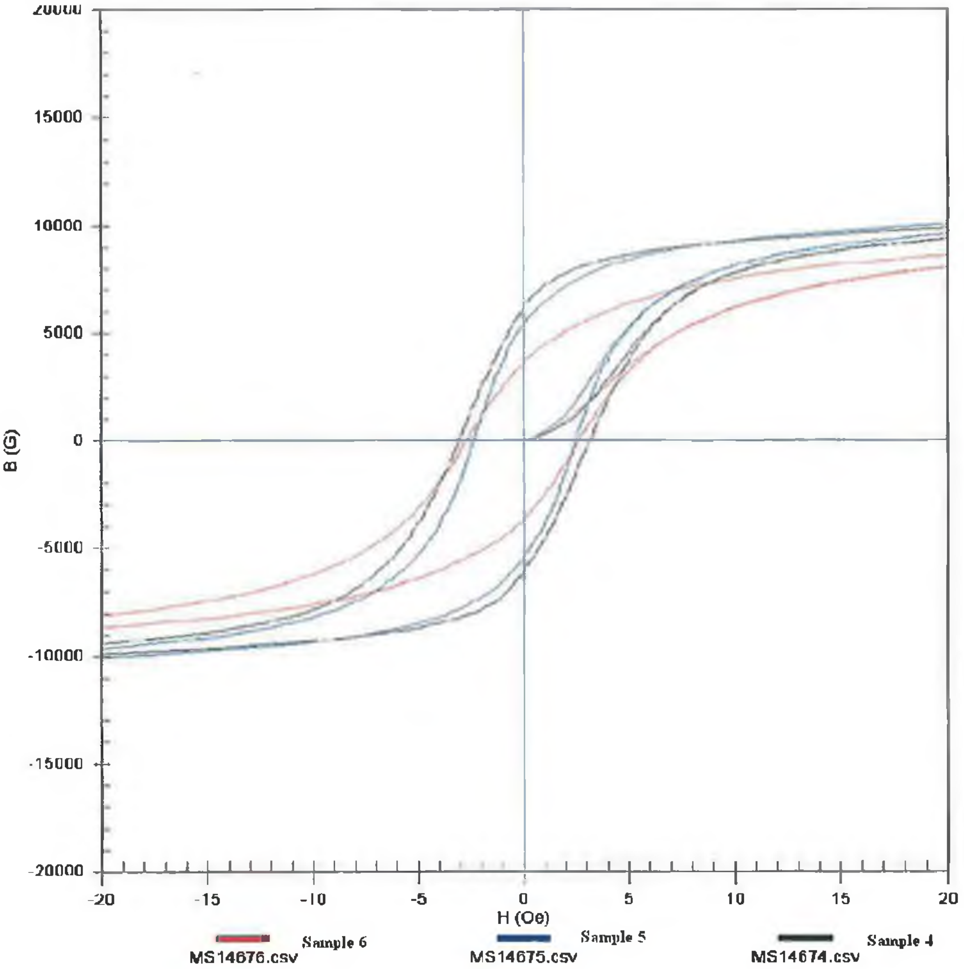

Fig. 5.15: Three hysteresis loops of samples 4, 5 and 6, at a higher magnification.

5.4.3 Co-Si-Fe samples

The results indicate that alloying iron with Cobalt and Silicon (samples 7 to10) makes the magnetic properties harder as shown in Table 5.8. The typical hysteresis loops of these samples are presented in Figs. 5.16 to 5.19. There is evidence that as the Cobalt percentage increases from 1% to 7% the maximum permeability decreases from 771 to 499. Whilst, the remanence or the residual magnetism decreases from 5630 G to 4284 G and the coercivity increases from 3.3 to 4.28 Oe. The magnetic properties for Co-Si-Fe alloys are presented in appendix C.

Table 5.8: The magnetic test results for the samples No. 7-10.

Property, unit \ Sample No.	7	8	9	10
Max. measured B, G	15350	15048	15116	15114
Max. measured H, Oe	1053	1018	1059	1021
Remanence B_r, G	5630	5067	4972	4284
Coercive field Hc, Oe	3.3	3.72	4.11	4.28
Max. permeability μmax	771	656	591	499
B @ Max. permeability, G	5856	4567	4288	4109
H @ Max. permeability, Oe	7.596	6.958	7.26	8.237

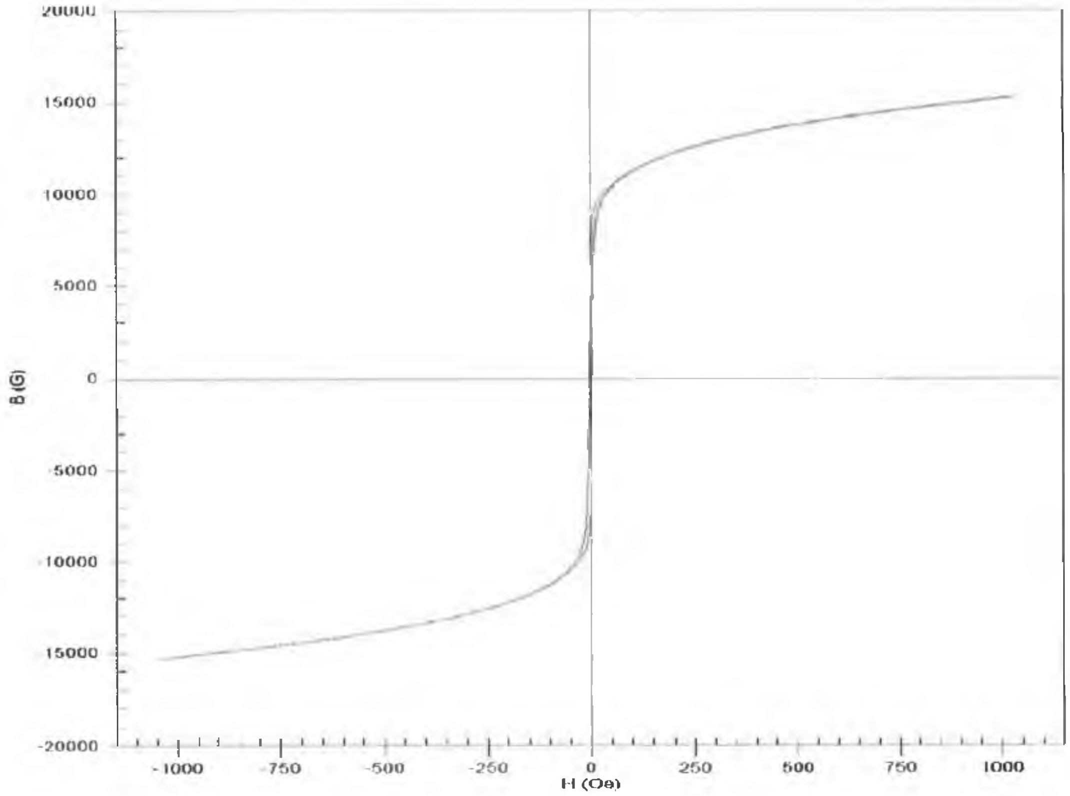

Fig. 5.16: Hysteresis loop for 1 % Co + 1 %Si.

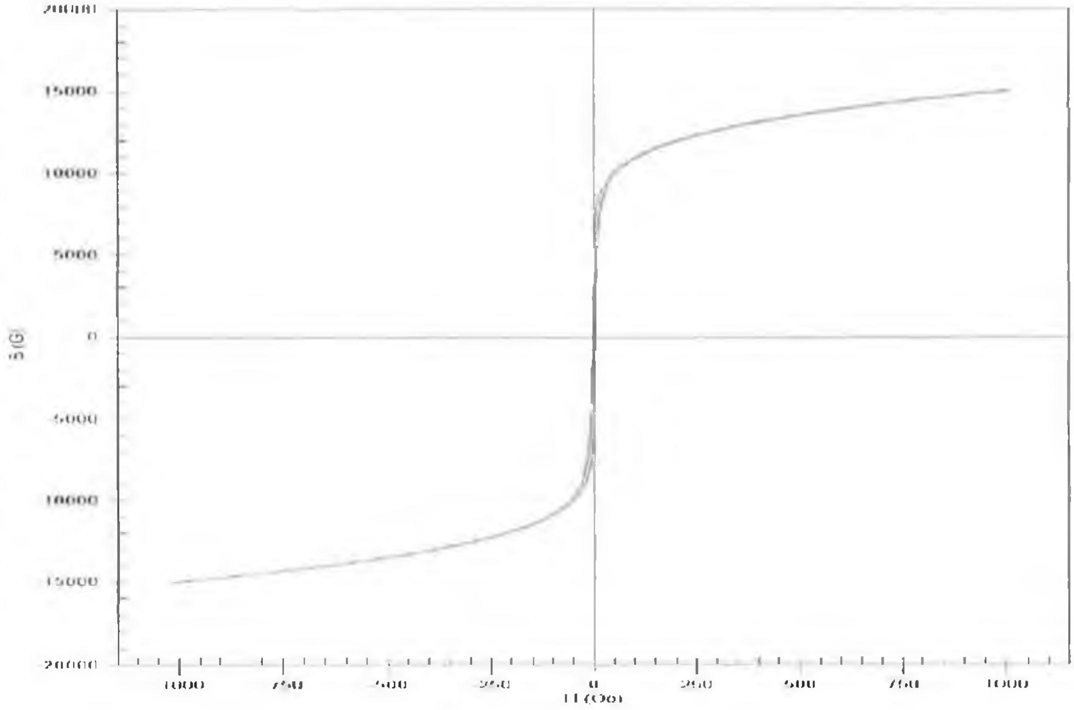

Fig. 5.17: Hysteresis loop for 3 % Co + 1 %Si.

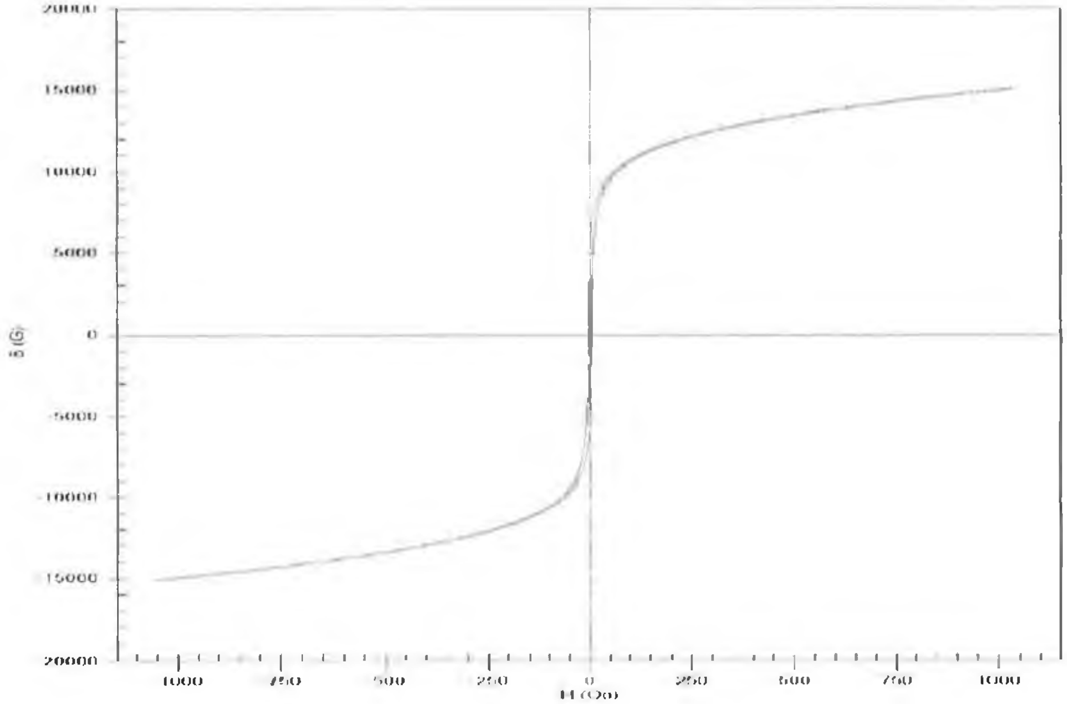

Fig. 5.18: Hysteresis loop for 5 % Co + 1 %Si.

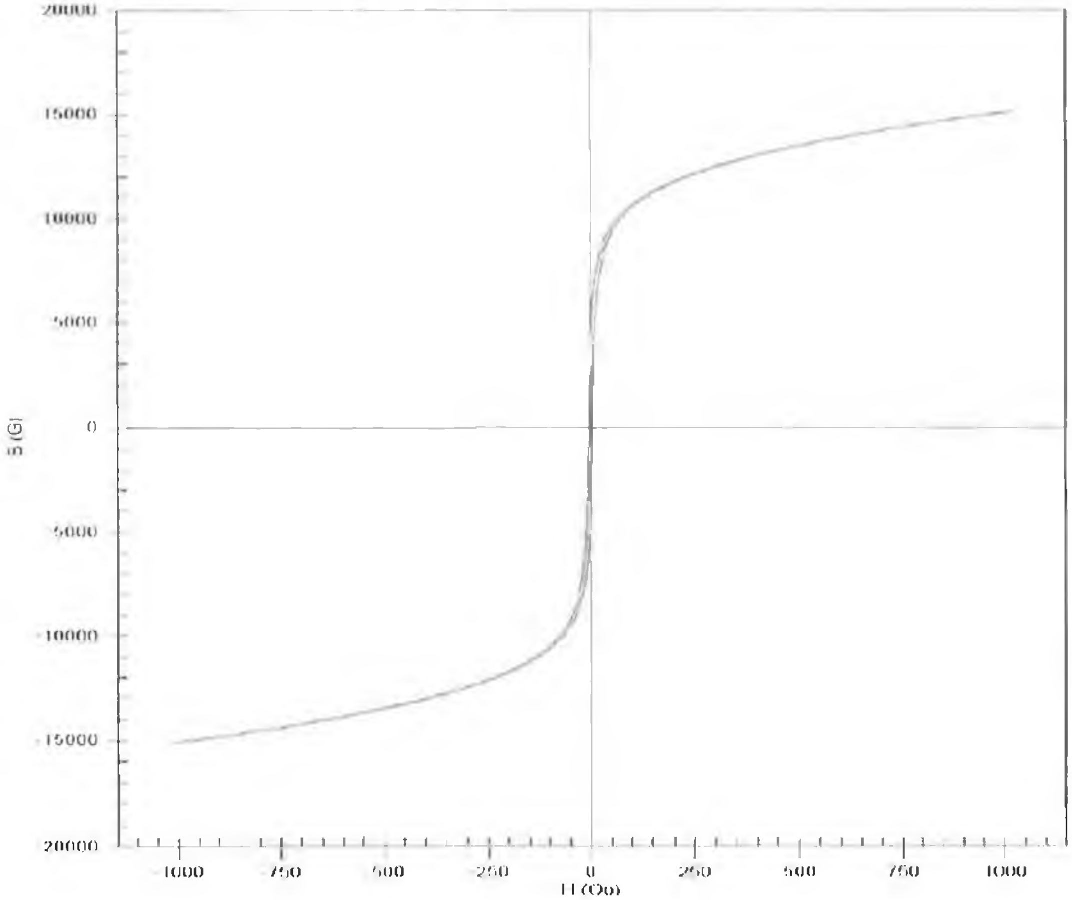

Fig. 5.19: Hysteresis loop for 7 % Co + 1 %Si.

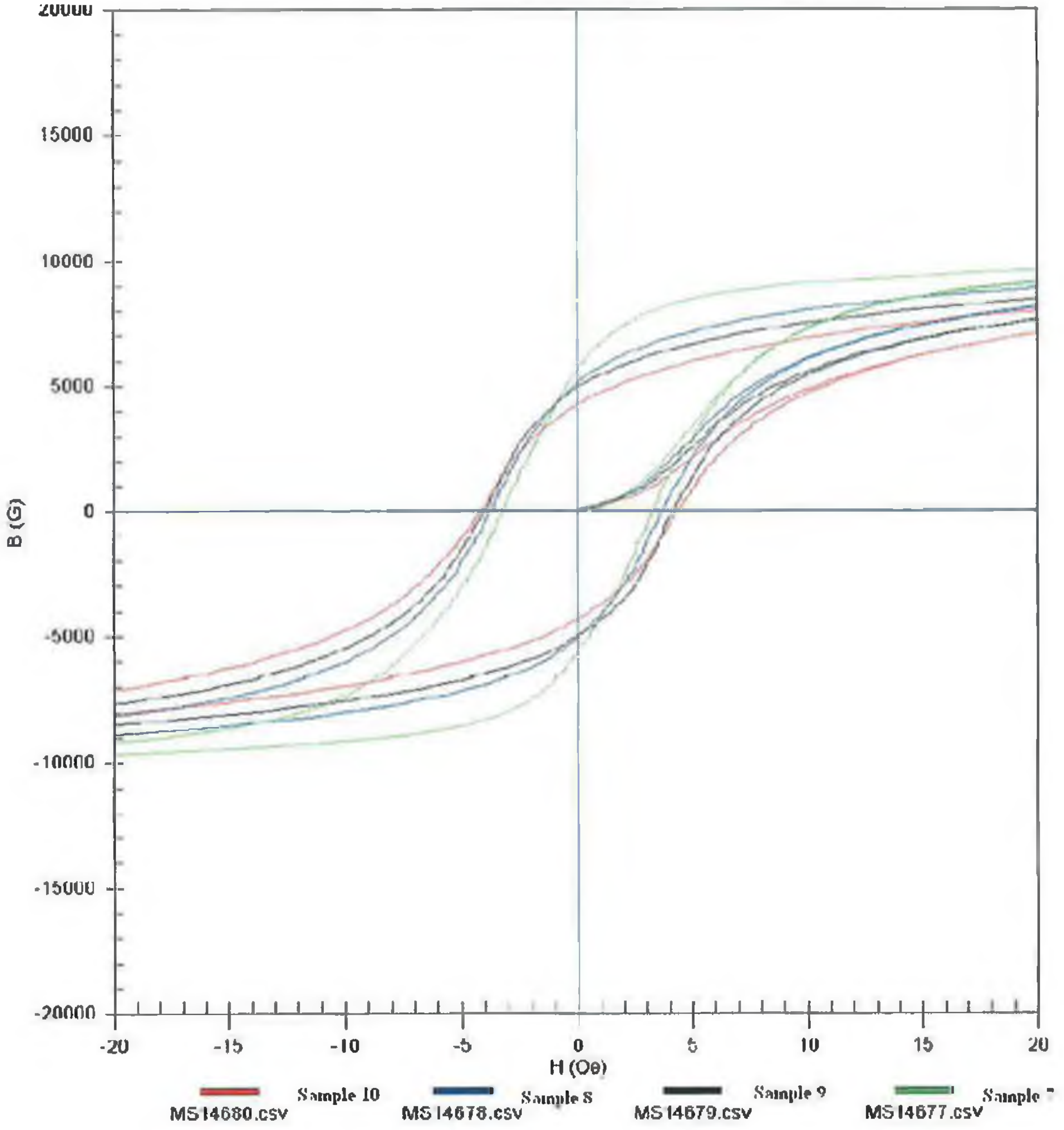

Fig. 5.20: Four hysteresis loops of sample 7, 8, 9 and 10, at a high magnification.

5.4.4 Comparison between the magnetic properties

a) Maximum permeability

In the literature [29, and 33-35] it is agreed that the Silicon content increases the maximum permeability when Silicon is added to iron. Fig. 5.21 shows the maximum permeability for the all samples with different composition. It is clear that sample number 3 has the highest permeability of 1102 G/Oe, while sample number 10 has the lowest permeability. However, sample number 4 which contains 1 %Co + 99% Fe has a maximum permeability of 885 which is higher than the 715 G/Oe of sample number 1, which contains 1% Si + 99% Fe. This shows that Cobalt in small concentrations has an even grater effect than Silicon. In general, the results show that the Silicon content tends to increase the permeability, and the cobalt content initially improves the permeability up to 2% Co and then tends to reduce the permeability, as in sample number 6, which contains 5% Co + 95% Fe. For the ternary alloys the maximum permeability decreases as the Cobalt content increases.

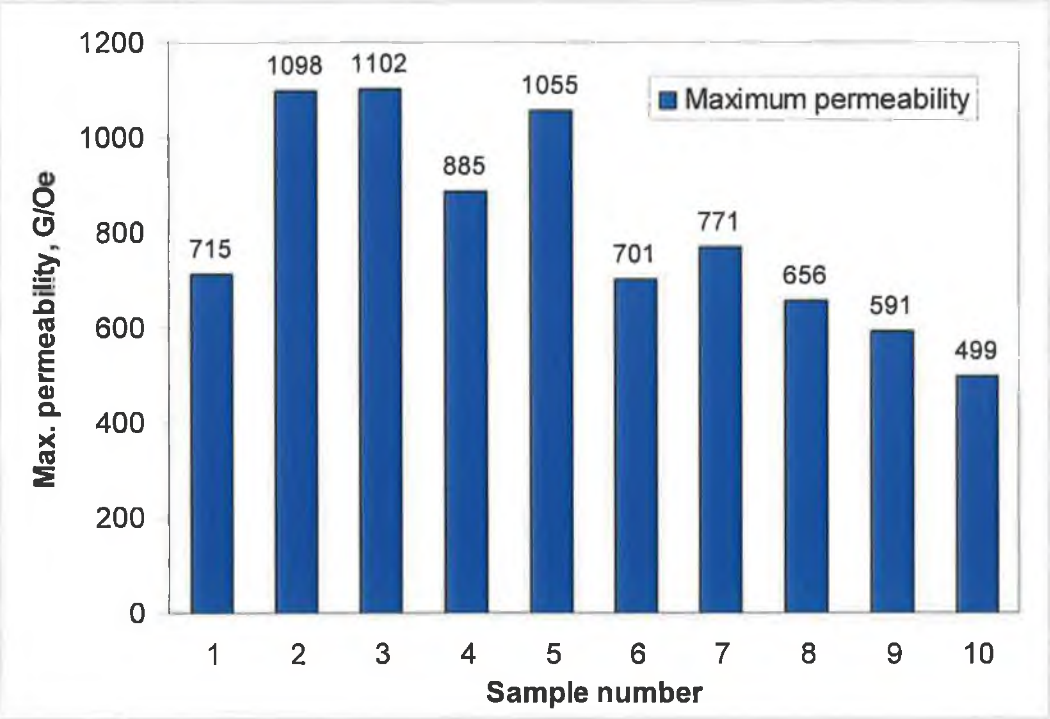

Fig. 5.21: Maximum permeability for the ten samples.

b) Coercive force

In terms of coercive force, additions of up to 3% Si reduce the coercive force down to 2.08 Oe shown in Fig. 5.22. On the other hand, the addition of 7% Co +1% Si + 92% Fe increases the coercive force up to 4.28 Oe. The data shows that additions of Silicon lead to a decrease in the coercive force from 3.7 down to 2.08 Oe. This result is in good agreement with that of Haneko [35]. However, the powders used in this study had lower purities and this resulted in higher values of the coercive force when compared to those of Haneko with the same Silicon percent [35]. The addition of Cobalt up to 3% tends to decrease the coercive force from 3.1 to 2.42 Oe, but as the Cobalt percentage was increased still higher to 5% the coercive force increases to 2.7 Oe. Also, the addition of Cobalt and Silicon together tends to increase the coercive force as the Cobalt content increases as shown in Fig. 5.22 sample 7 to 10. Again in the comparison between sample 1 and 4 it was found that the coercive force decreased by 0.6 Oe, indicating that the addition of small amount of Cobalt has a greater effect in decreasing the coercive force than Silicon.

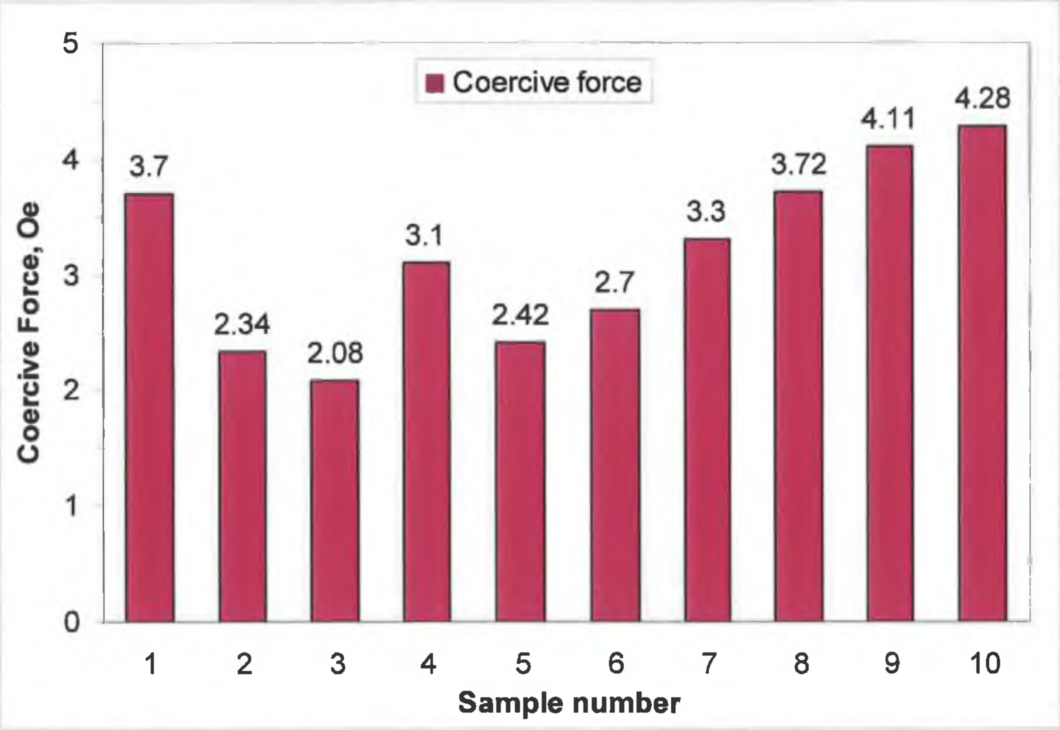

Fig. 5.22: Coercive force for the ten samples.

c) Induction

The best soft magnetic materials have a narrow area for the hysteresis loop in the H-B curve as stated in [29]. All of the B-H curves obtained in the current work have this feature of a narrow hysteresis loop. Also, it is beneficial to have a saturation induction, B_{max}, obtained with the minimum magnetic field input (H) for those considered materials. The values of B_{max} of 19606 and 19551 G were obtained with an applied magnetic field input of 1033 and 1055 Oe for samples 2 and 3 respectively as shown in Fig. 5.23. For samples 4 – 6 the maximum magnetic induction obtained was 16185 G with maximum field strength of 1033 Oe in sample number 5. For the rest of the samples the maximum magnetic saturation was varying around an average value of 15157 G at an average field strength of 1038 Oe. The magnetic saturation for these samples decreases as the Cobalt content increases. In regard to B_r, it should be as small as possible for these materials [29]. As can be seen in Fig. 5.23, B_r value decrease as the percentage of silicon and Cobalt increased in samples 1 to 3 and samples 4 to 6 respectively.

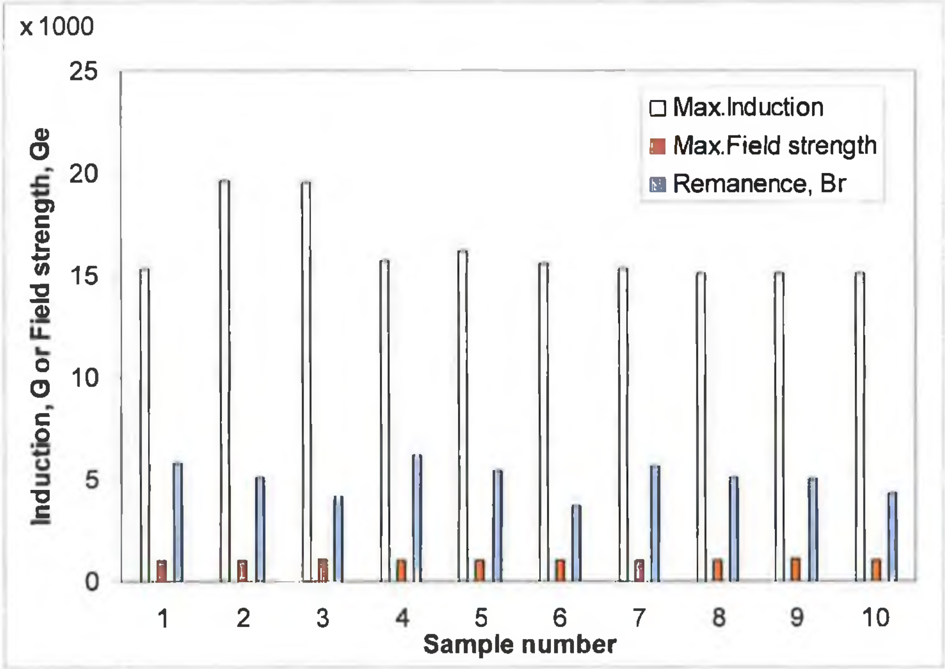

Fig. 5.23: B_{max}, B_r and H_{max} for the ten samples.

CHAPTER VI
FINITE ELEMENT ANALYSIS RESULTS AND DISCUSSION

6. FINITE ELEMENT ANALYSIS RESULTS

This chapter presents all the results generated by the finite element analysis model described earlier in chapter four. Different models were created using ANSYS version 9 to simulate the effect of material properties, a parameter involving the current and the number of turns of the coil ampere x coil turns and the gap between the armature and the back-iron. The effects of these parameters were to be assessed with reference to the force generated in the solenoid. The magnetic properties of the solenoid material have been presented already in chapter 5. Different ampere values were used with a coil of 32 turns. The current density was calculated by using equation 6.1.

$$\text{Current density} = \frac{I \times N}{A} \qquad 6.1$$

Where:

I: Applied current.

N: Coil turns.

A: Coil Area considered equal to $5.5 \text{ X } 10^{-6} \text{ m}^2$, this based on a coil radius of 1.3 mm.

The effects of three different gap sizes were assessed for the type of solenoid for automotive fuel injection. They were 0.1, 0.15 and 0.20 mm. A comparison between all the different materials with the three gap sizes was made at a flux density around the saturation limit of the materials "1.5- 2 Tesla". After some initial work the current was fixed at 5 amps, to allow the materials to reach close to their saturation limit. Therefore the parameters of current times the number of turns of the coil was fixed at 160. The results show that the magnetic force ranged between 16 and 66N. Details of these results are described in the following sections.

6.1 Results of Fe-Si Samples

Three different Silicon percentages varying between 1% and 3%Si were studied to investigate their effect on the solenoid performance used in automotive and biomedical applications.

6.1.1 Material 1 (1%Si + 99%Fe)

Many models were built up to simulate the effect of magnetic properties on the solenoid functionability. Three different gap sizes were simulated with the magnetic properties of material 1 and the parameter of current times number of turns of the coil was chosen to be 160 to compare between the forces generated by magnetism resulting from the different magnetic fields in all cases. The magnetic density for all the above cases was selected to be slightly lower than the saturation value for all cases. Fig. 6.1 shows the magnetic flux diagram for ampere times turns parameter of 160. The results show that the force is about 42 N after simulating the solenoid with a gap of 0.1 mm. Fig. 6.2 presents the magnetic density with gap of 0.15 mm. In this case the results indicate that the force is reduced to about 20 N. Finally, Fig. 6.3 presents the magnetic density with a gap of 0.2 mm, the force was about 12 N. Fig. 6.4 is a comparison diagram for the forces for the same current times turns parameter of 160 with the different gap sizes in the Ferro-solenoid with 1%Si. It is clear from this figure that as the gap increases from 0.1 to 0.2 mm the force decreases dramatically. By choosing the system with an air gap of 0.1 mm the resulting force would be larger by a factor of 3.61 times when compared with the force produced using an air gap of 0.2 mm for the same coil turns and current.

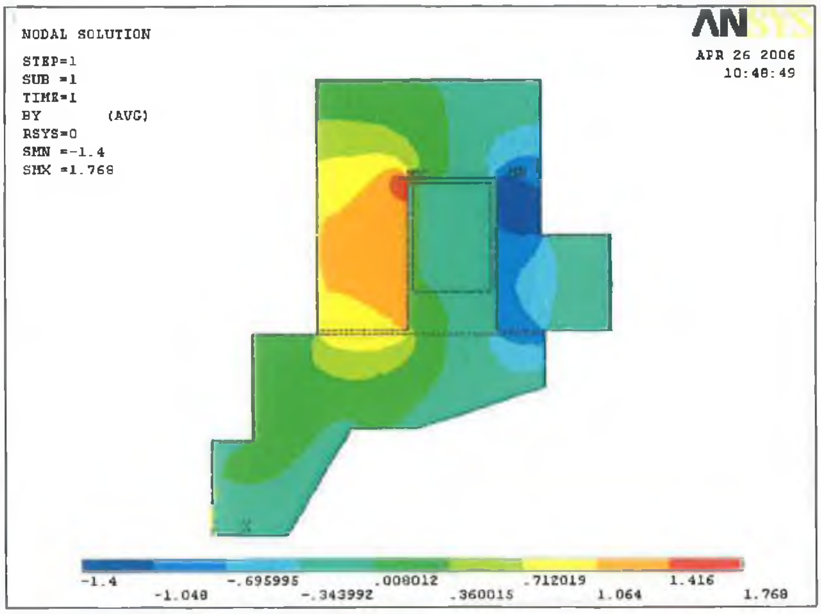

Fig. 6.1: Magnetic flux density for material1 current times turn parameter = 160 and gap = 0.10 mm.

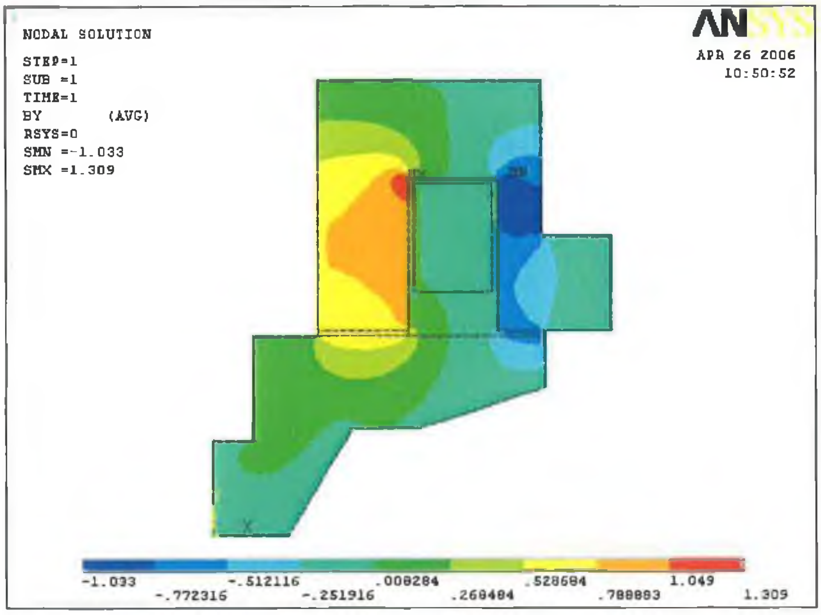

Fig. 6.2: Magnetic flux density for sample 1 current times turn parameter = 160 and gap = 0.15mm.

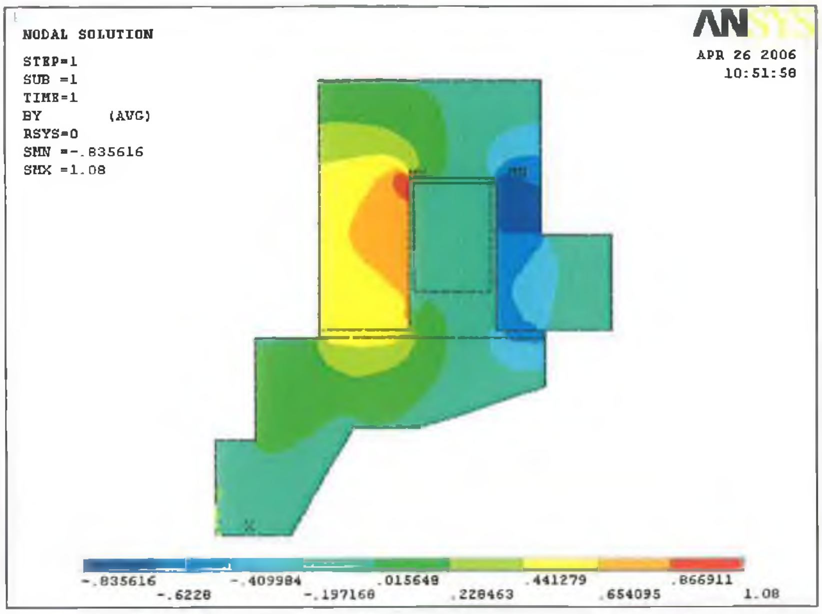

Fig. 6.3: Magnetic flux density for sample 1 current times turn parameter = 160 and gap = 0.20mm.

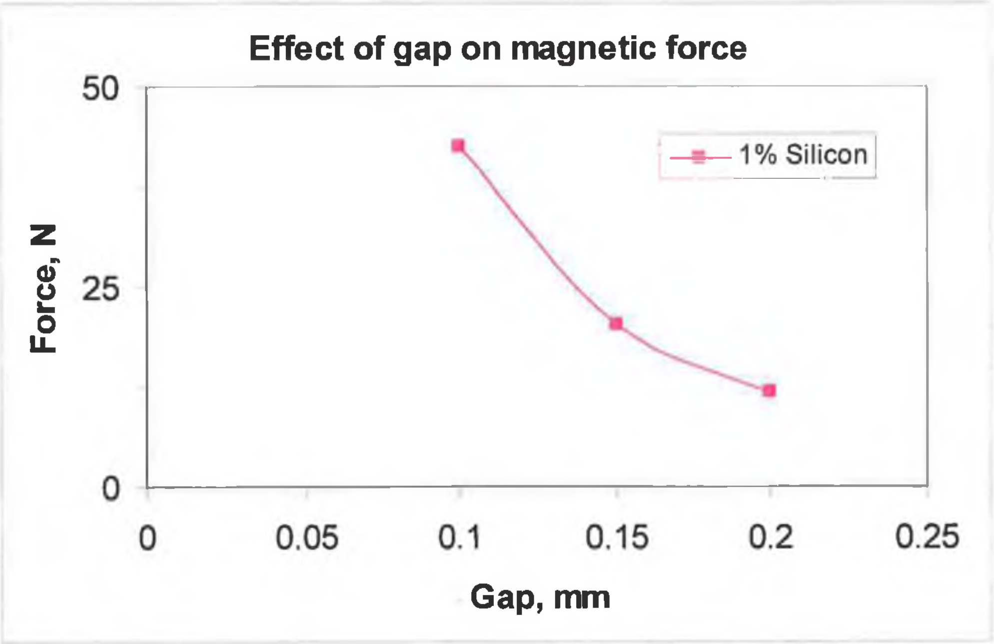

Fig. 6.4: Predicted force verses gap size for material 1 at current times turn parameter of 160.

6.1.2 Material 2 (2%Si + 98%Fe)

Similarly, several models were constructed to model the effect of magnetic properties on the solenoid performance using the second material. The same three different gap sizes were simulated using the magnetic properties of material 2 and current/turns parameter of 160. The magnetic flux density for all the above cases was selected to be lower than the saturation. Fig. 6.5 illustrates the magnetic flux diagram produced by ANSYS with a gap of 0.1 mm, the results demonstrate that the force is about 46 N. Fig. 6.6 displays the magnetic flux density with gap of 0.15 mm; in this case the magnetic force is around 21 N. Finally, Fig. 6.7 presents the magnetic flux density with a gap of 0.2 mm. The force here is about 12 N. Fig. 6.8 is a comparison for the force with different gap sizes for a solenoid material made from Fe-2%Si. It is clear from this figure that by increasing the gap between the armature and the back-iron from 0.1 to 0.2 mm the magnetic force decreases considerably.

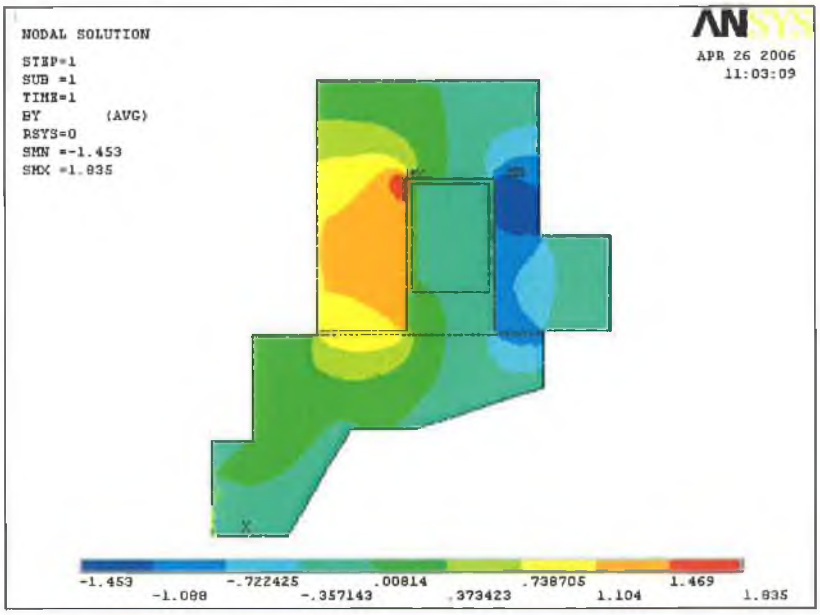

Fig. 6.5: Magnetic flux density for material 2 current times turn parameter = 160 and gap = 0.1mm.

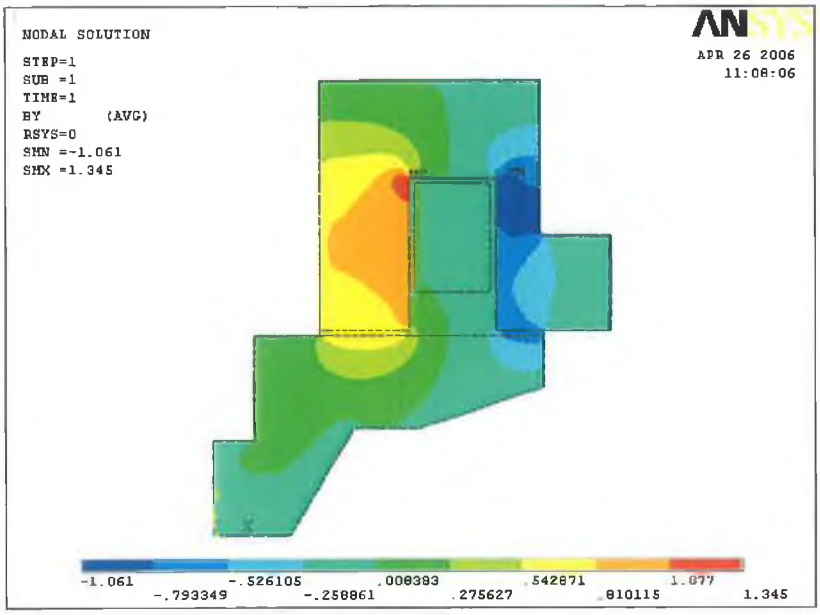

Fig. 6.6: Magnetic flux density for material 2 current times turn parameter = 160 and gap = 0.15mm.

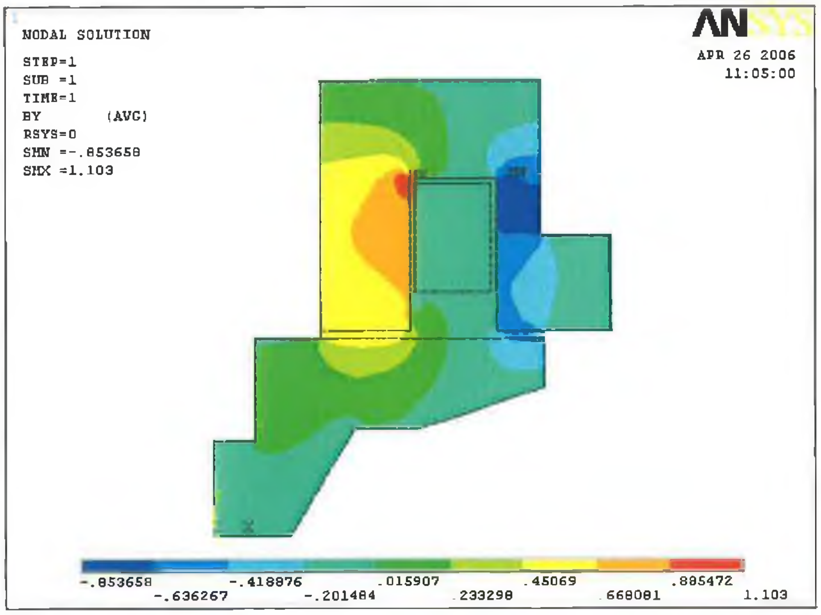

Fig. 6.7: Magnetic flux density for material 2 current times turn parameter = 160 and gap = 0.2mm.

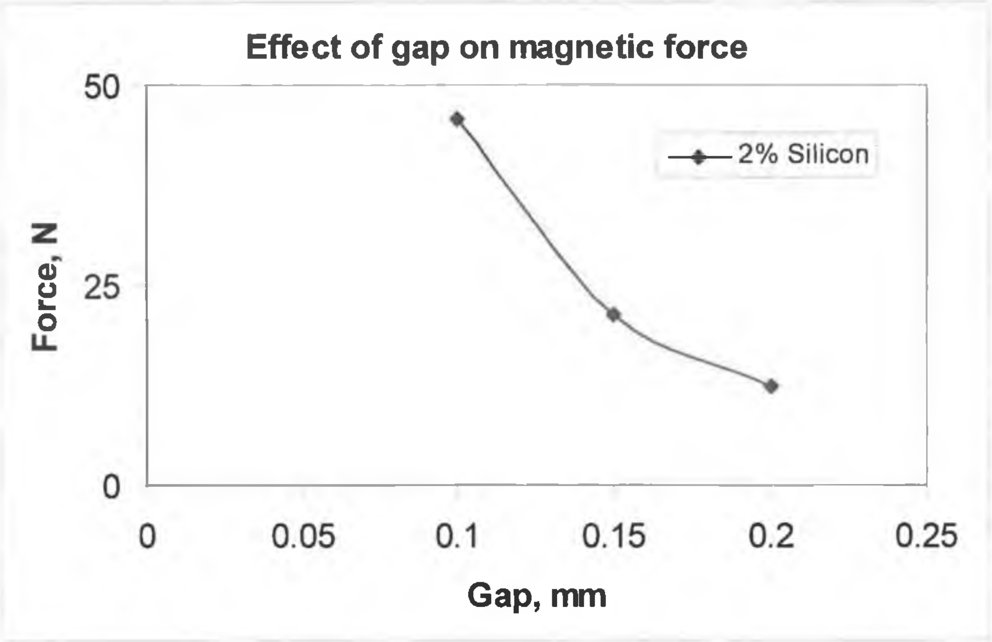

Fig. 6.8: Predicted force verses gap size for material 2 at current times turn parameter of 160.

6.1.2 Material 3 (3%Si + 97%Fe)

Again the same procedure was followed to simulate the effect of the magnetic properties on the solenoid functionability for material 3. Again the three different gap sizes were simulated for material 3 with the same current/turns parameter. Again the magnetic flux density for all the above cases was selected to be slightly lower than the saturation for all cases. Figs. 6.9 to 6.11 show the magnetic flux for three different gap sizes. The result indicates that the forces were about 45, 21 and 12 N for gaps of 0.1, 0.15 and 0.2 mm respectively. Fig. 6.12 presents the effect of gap size on the force.

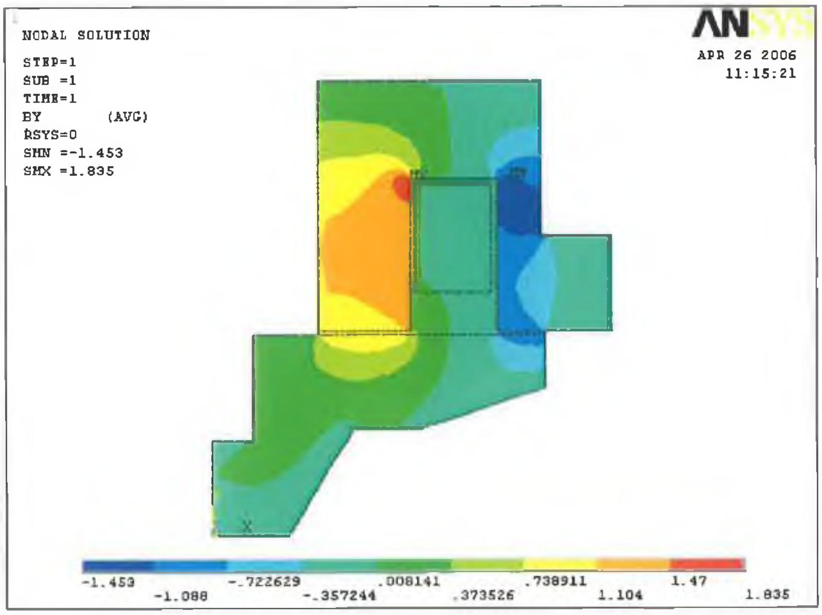

Fig. 6.9: Magnetic flux density for material 3 current times turn parameter = 160 and gap = 0.1mm.

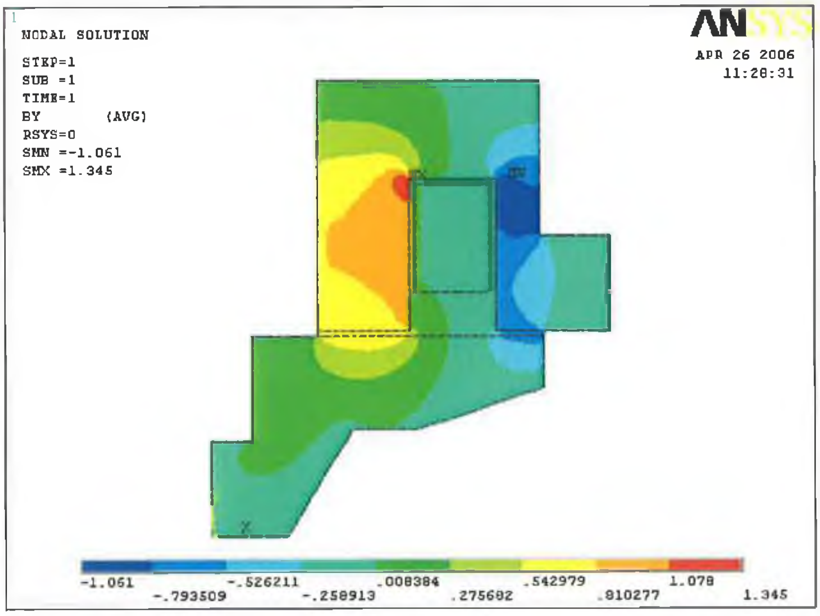

Fig. 6.10: Magnetic flux density for material 3, current times turn parameter = 160 and gap = 0.15mm.

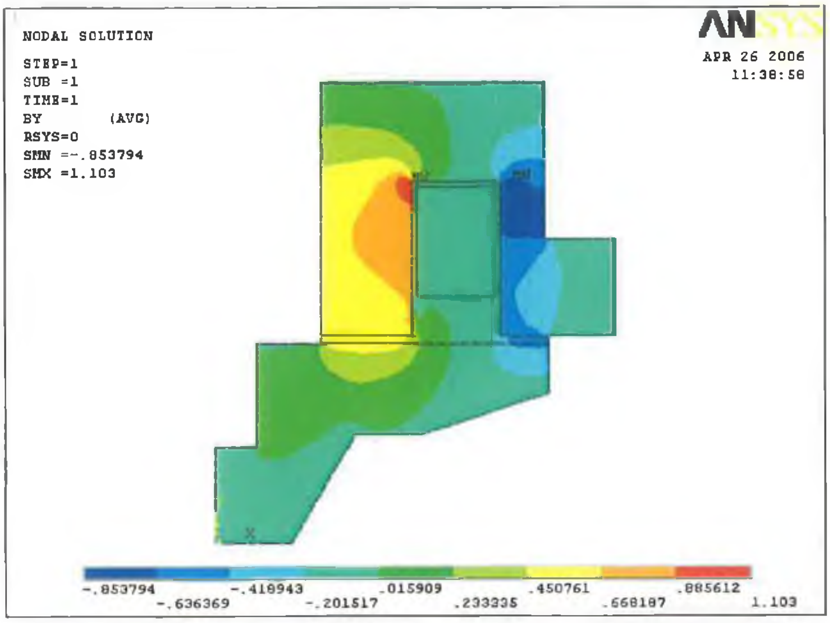

Fig. 6.11: Magnetic flux density for material 3, current times turn parameter = 160 and gap = 0.2mm.

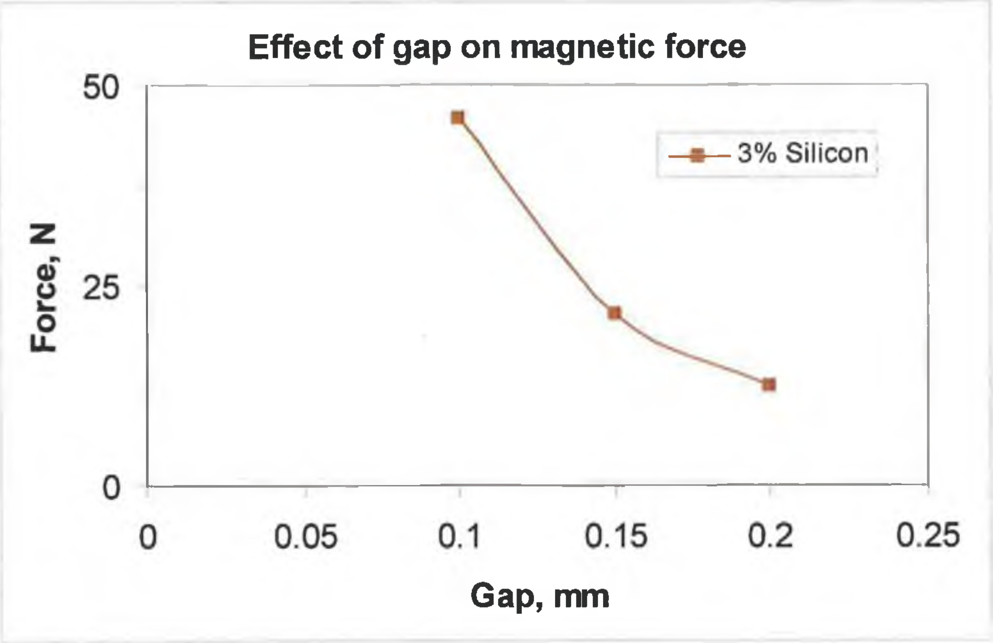

Fig. 6.12: Predicted force verses gap size for material 3 at current times turn parameter of 160.

It is noticeable that the force increases as the Silicon content increases due to the enhancement in the soft magnetic properties as shown in Fig. 6.13. This result is in a good agreement with the experimental and analytical results obtained by Olabi and Recco [40] and Ricco et al. [42]. The result also demonstrates that a maximum force of 46 N could be achieved with Fe-3%Si.

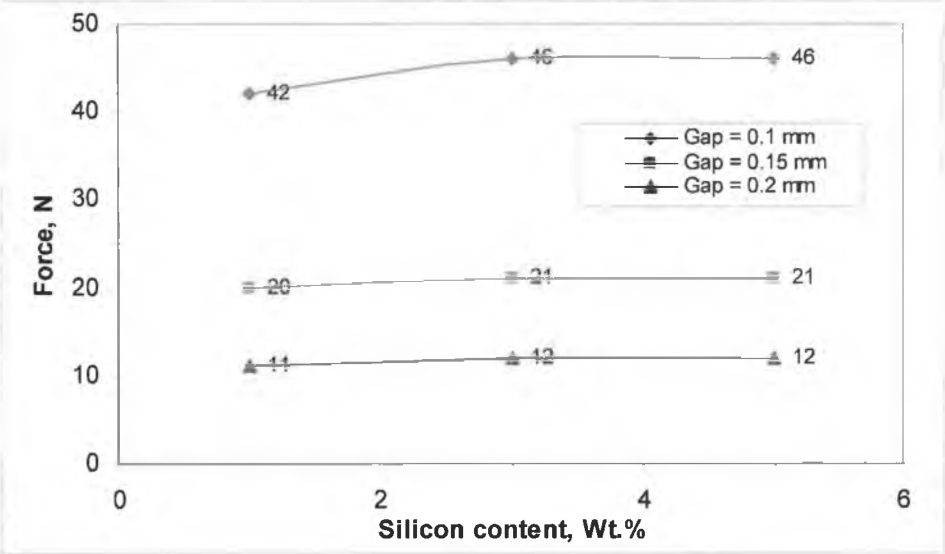

Fig. 6.13: Effect of Silicon content on the force at different air gap sizes.

6.2 Results of Fe-Co Samples

The three different Cobalt alloys with percentages varying between 1% and 5%Co were studied to investigate the effect on the magnetic properties.

6.2.1 Material 4 (1%Co + 99%Fe)

The same procedure was followed for material 4. Fig. 6.14 shows the magnetic flux chart created by ANSYS with a gap of 0.1 mm. The results demonstrate that the force is about 44 N after simulating the solenoid with a gap size of 0.1 mm. Fig. 6.15 shows the magnetic density with gap size of 0.15 mm. The results indicate that the magnetic force is around 21 N. Finally, Fig. 6.16 presents the magnetic density with a gap size of 0.2 mm, the results show that the force is about 12 N. Fig. 6.17 presents a comparison between the magnetic forces with different gap sizes.

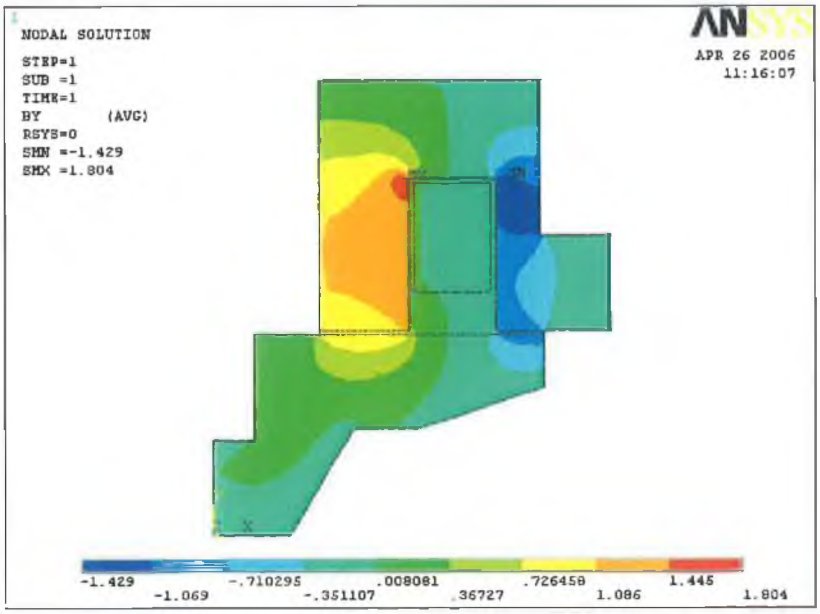

Fig. 6.14: Magnetic flux density for material 4 current times turn parameter = 160 and gap = 0.10mm.

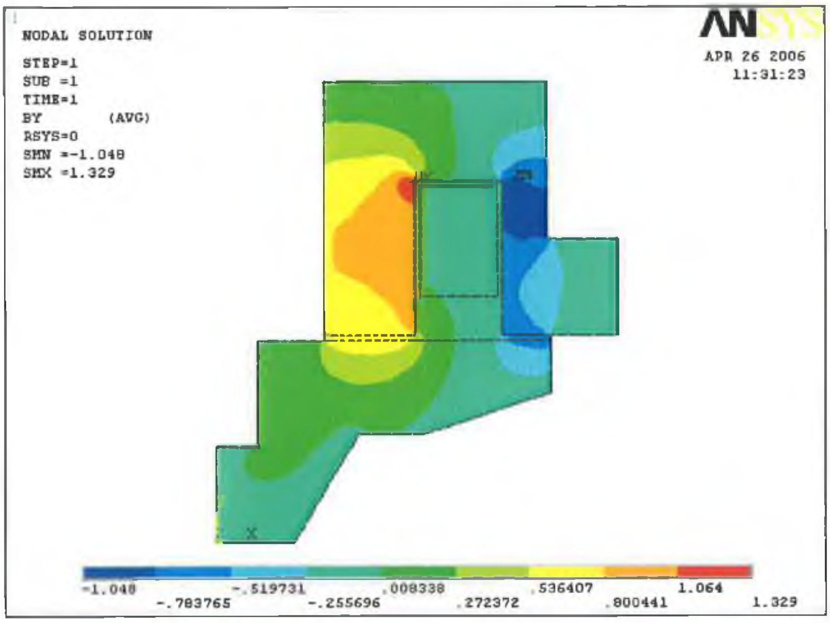

Fig. 6.15: Magnetic flux density for material 4 current times turn parameter = 160 and gap = 0.15mm.

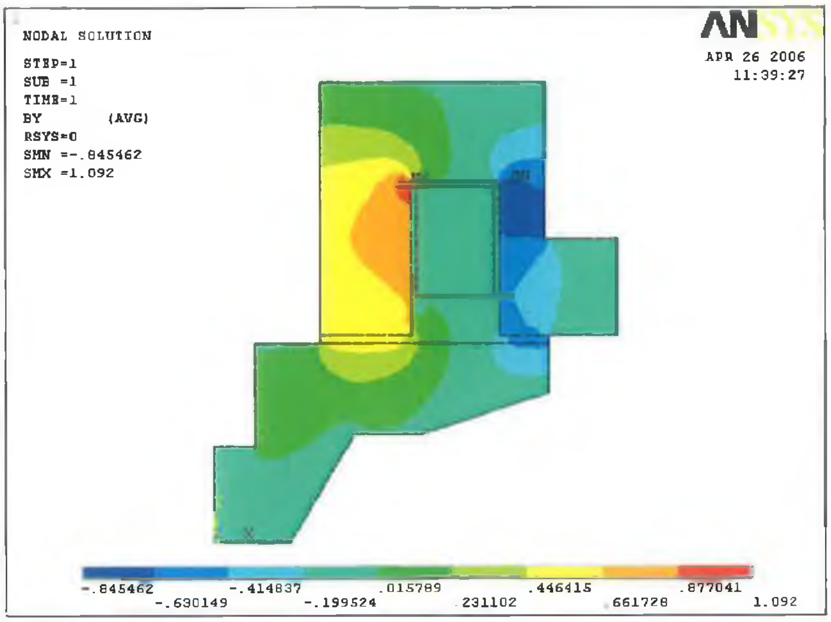

Fig. 6.16: Magnetic flux density for material 4 current times turn parameter = 160 and gap = 0.20mm.

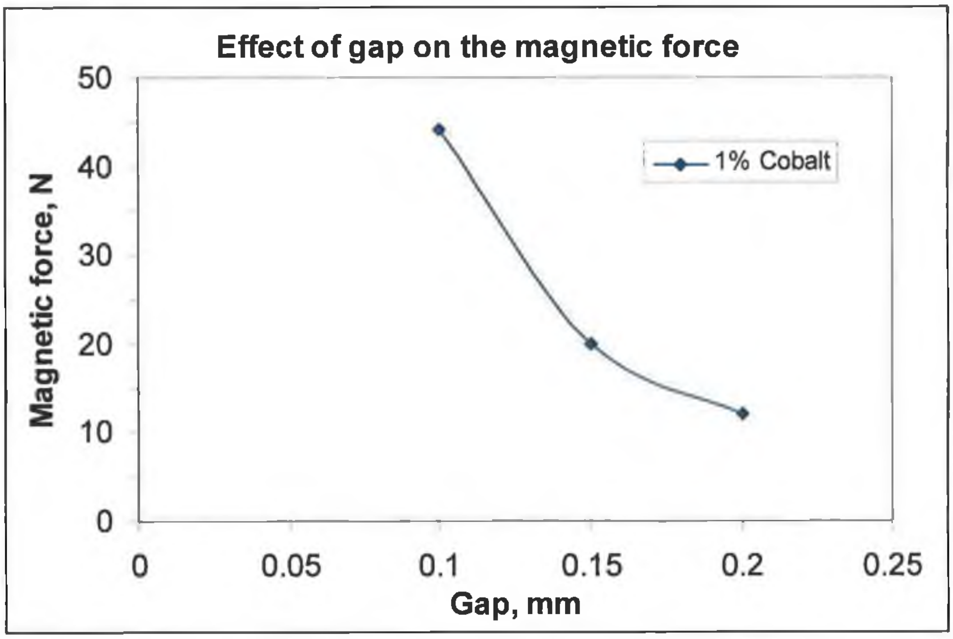

Fig. 6.17: Predicted force verses gap size for material 4 at current times turn parameter of 160.

6.2.2 Material 5 (3%Co + 97%Fe)

Again the same procedure was followed for material 5. Fig. 6.18 presents the magnetic flux diagram generated by ANSYS with a gap of 0.1 mm. The results reveal that the magnetic force is about 45 N. Fig. 6.19 displays the magnetic flux density with gap size of 0.15 mm. The results show that the force is around 21 N. Finally, Fig. 6.20 shows the magnetic flux density with a gap size of 0.2 mm. The results indicate that the force is about 12 N. A comparison for the forces of the solenoid made from Fe-3%Co is presented in Fig. 6.21.

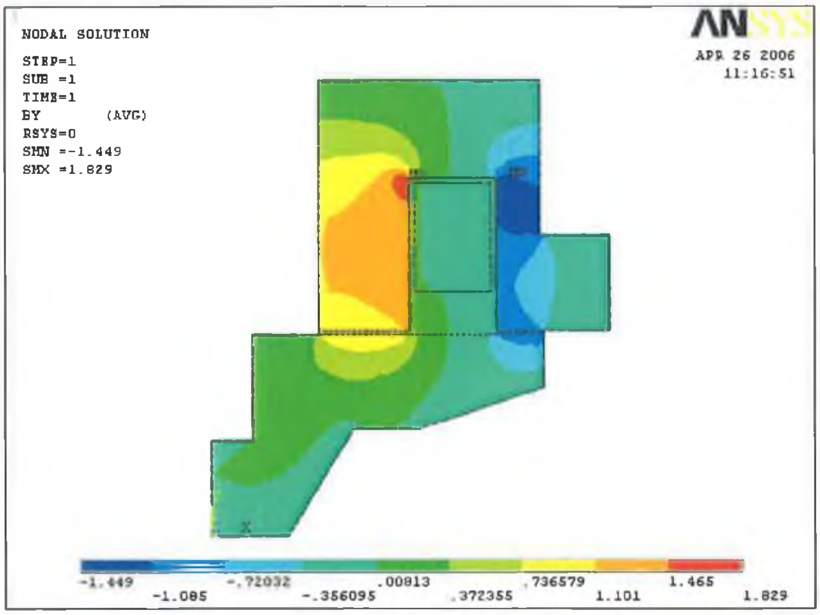

Fig. 6.18: Magnetic flux density for material 5 current times turn parameter = 160 and gap = 0.10mm.

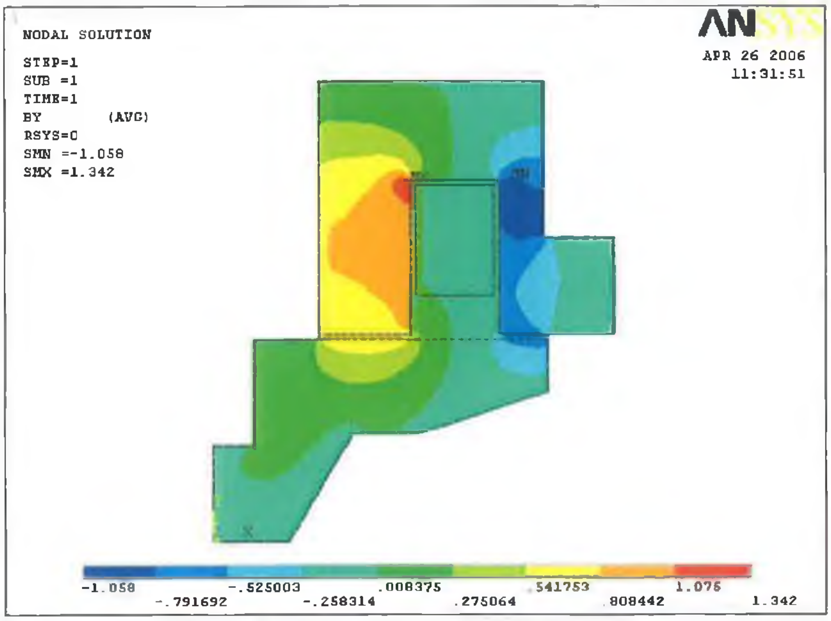

Fig. 6.19: Magnetic flux density for material 5 current times turn parameter = 160 and gap = 0.15mm.

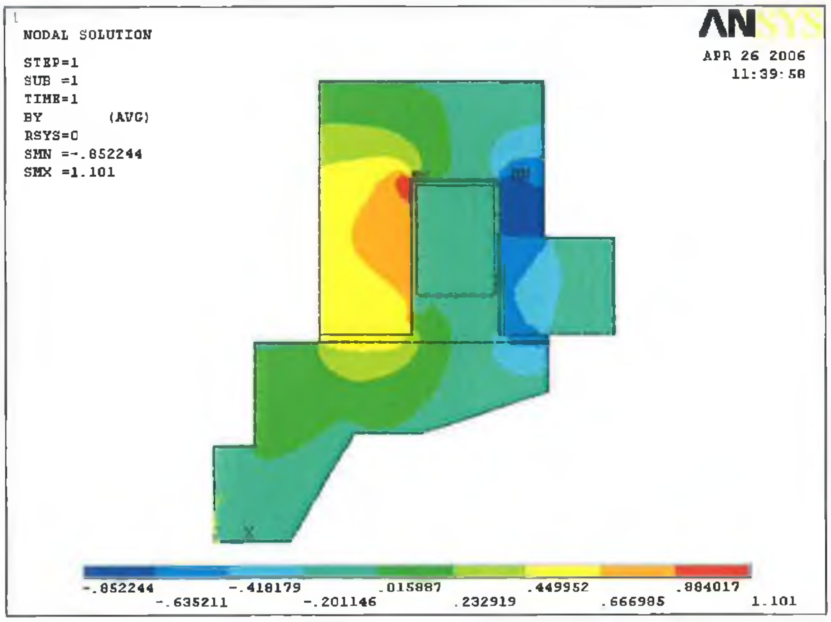

Fig. 6.20: Magnetic flux density for material 5 current times turn parameter = 160 and gap = 0.20mm.

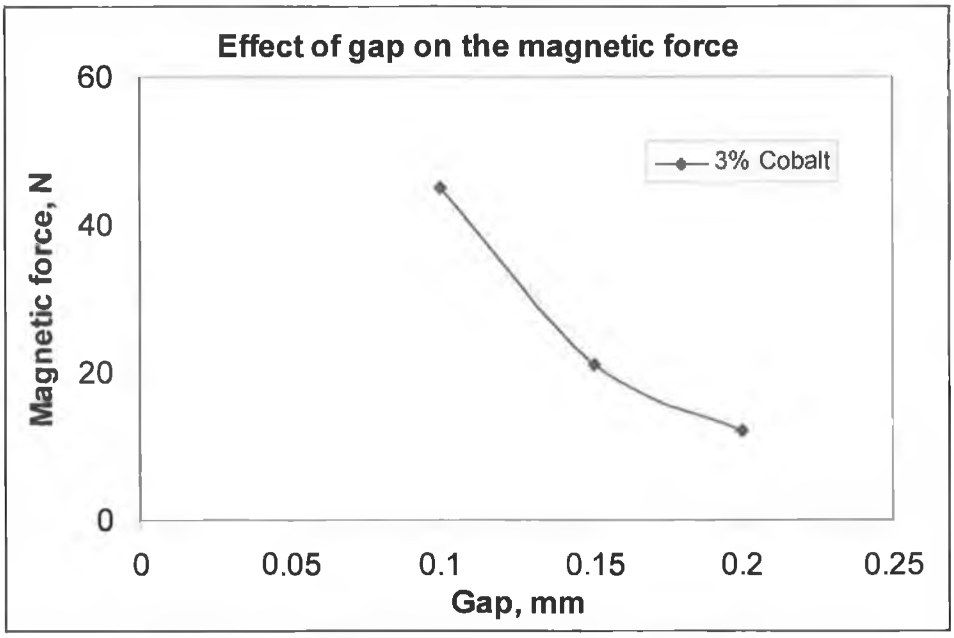

Fig. 6.21: Predicted force verses gap size for material 5 at current times turn parameter of 160.

6.2.3 Material 6 (5%Co + 95%Fe)

Again the same procedure was followed. Fig. 6.22 shows the magnetic flux chart using a gap of 0.1 mm. The results show that the force is approximately 42 N. Fig. 6.23 displays the magnetic flux density with gap size of 0.15 mm; in this case the results indicate that the magnetic force is around 20 N. Finally, Fig. 6.24 shows the magnetic flux density with a gap size of 0.2 mm. The force here is around 11 N. Fig. 6.25 is a comparison of the forces with the difference between the gap sizes.

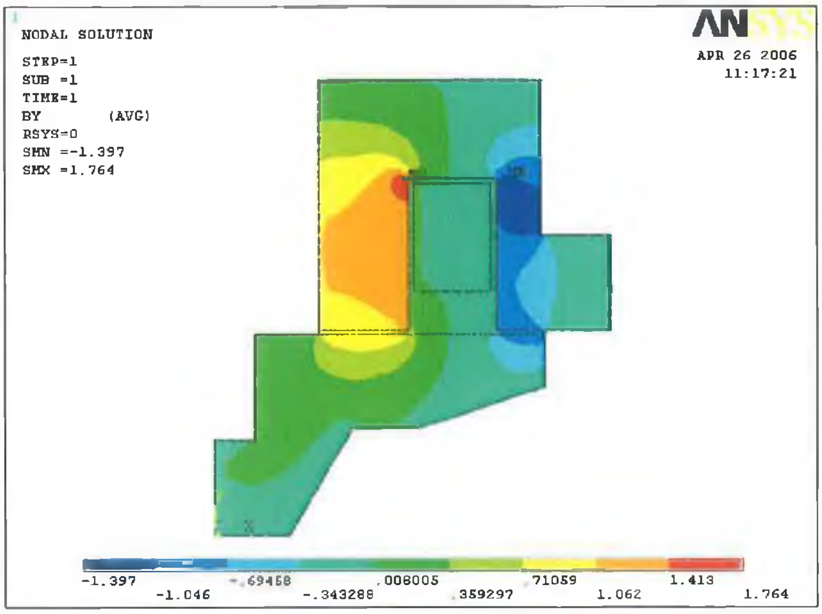

Fig. 6.22: Magnetic flux density for material 6 current times turn parameter = 160 and gap = 0.10 mm.

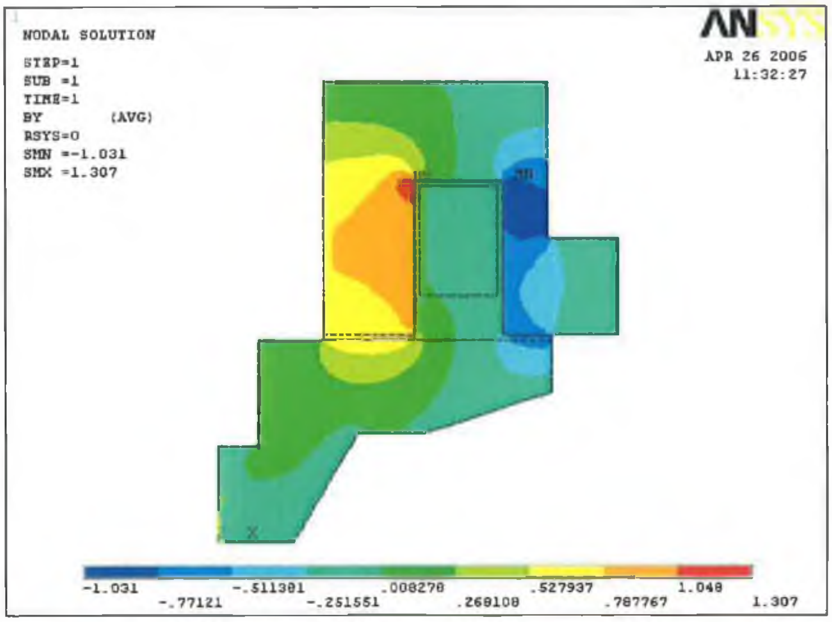

Fig. 6.23: Magnetic flux density for material 6 current times turn parameter = 160 and gap = 0.15 mm.

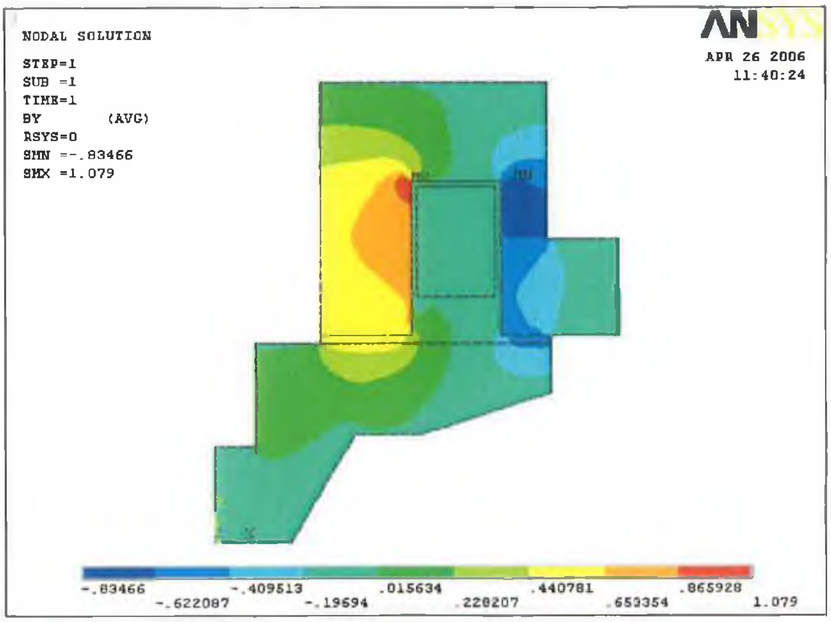

Fig. 6.24: Magnetic flux density for material 6 current times turn parameter = 160 and gap = 0.20 mm.

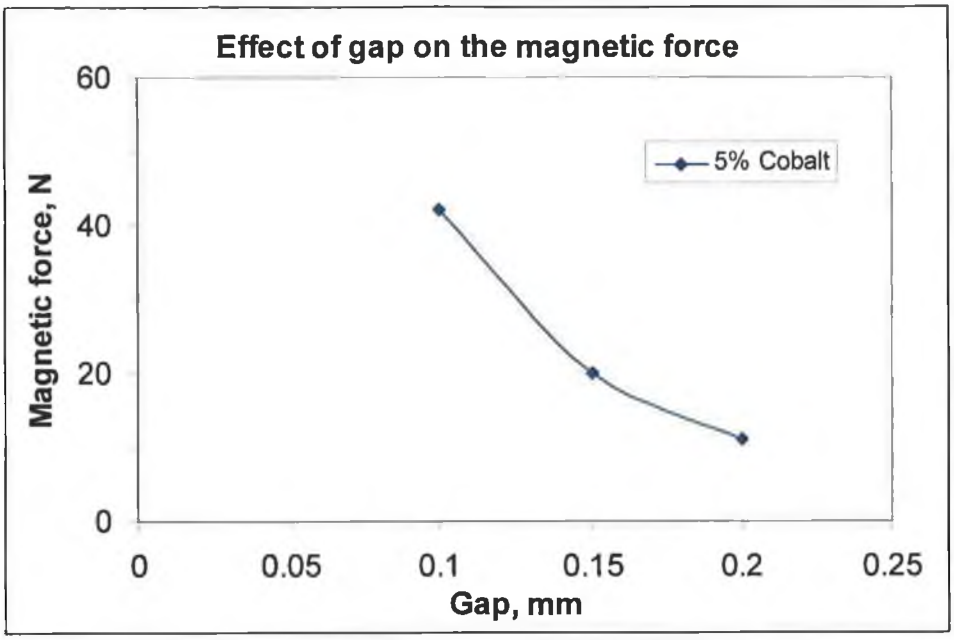

Fig. 6.25: Predicted force verses gap size for material 6 at current times turn parameter of 160.

Comparing the magnetic performances of the Co-Fe materials, it is obvious that material 5 has the best magnetic properties among the three materials and the forces produced by the solenoid made from this material are always the highest. Fig. 6.26 shows the effect of Cobalt on the force at different air gap sizes. The results show that by increasing the Cobalt percentage above 3% the magnetic properties decrease. It can be noted that the Cobalt tends to produce magnetically harder properties when added to iron at higher percentages as described by Yu et al. [54]. On the other hand, addition of Cobalt to iron is effective in maintaining the magnetic properties in high temperature applications as presented in Ref. [54].

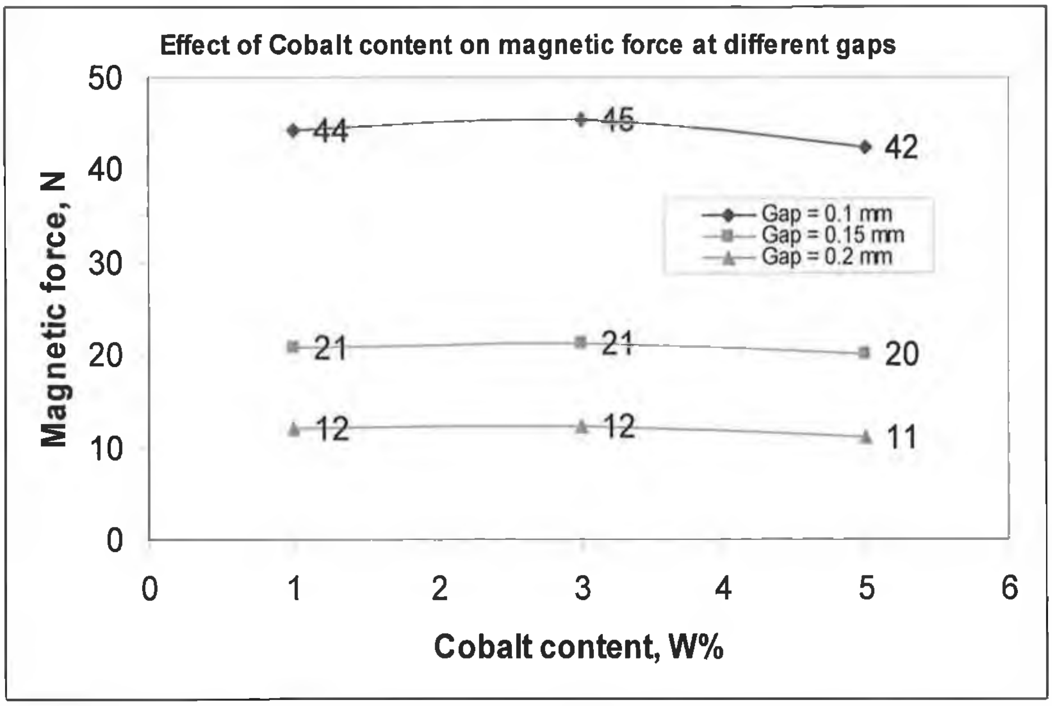

Fig. 6.26: Effect of Cobalt content on force at different air gap sizes.

6.3 Results of Fe-Co-Si Samples

Four different alloys of Iron Cobalt and Silicon, with the percentage of Cobalt varying between 1% and 7%Co and the Silicon content fixed at 1% were studied to investigate their effect on the magnetic properties.

6.3.1 Material 7 (1%Co + 1%Si + 98%Fe)

Again the same procedure was followed. Fig. 6.27 shows the magnetic flux diagram with a gap size of 0.1 mm. The results demonstrate that the force is about 43N. Fig. 6.28 shows the magnetic density with gap size of 0.15 mm. The results indicate that the force is about 20 N. Finally, Fig. 6.29 presents the magnetic density with a gap size of 0.2 mm. The result shows that the force is about 12 N. Fig. 6.30 presents the comparison of results for the forces with different gap sizes.

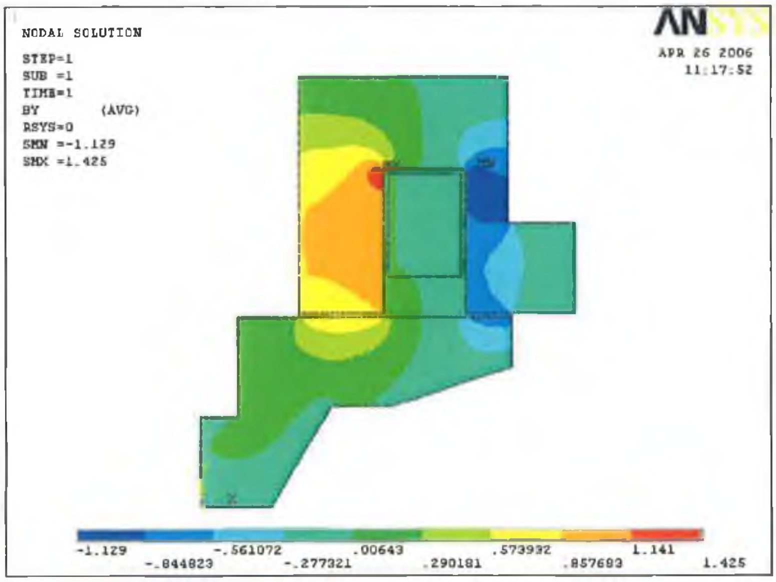

Fig. 6.27: Magnetic flux density for material 7 current times turn parameter = 160 and gap = 0.10 mm.

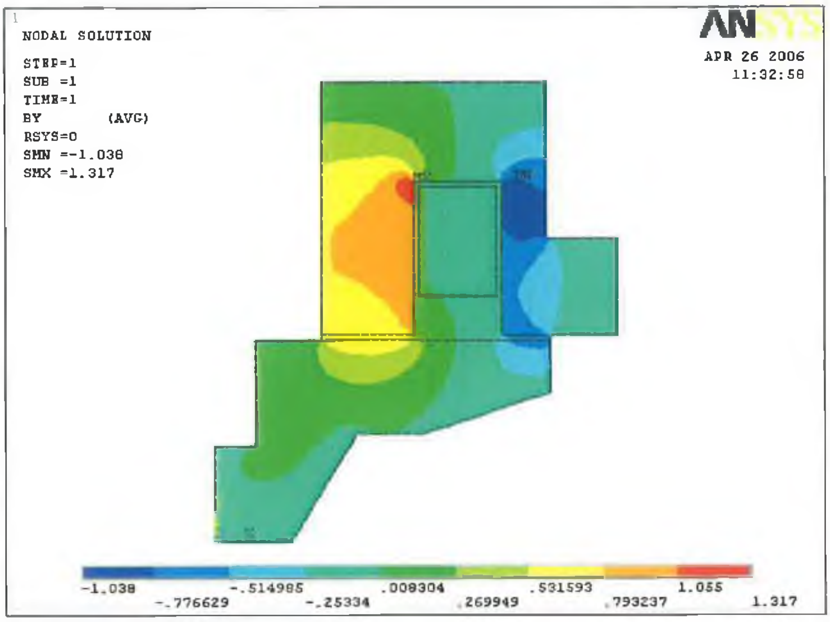

Fig. 6.28: Magnetic flux density for material 7 current times turn parameter = 160 and gap = 0.15 mm.

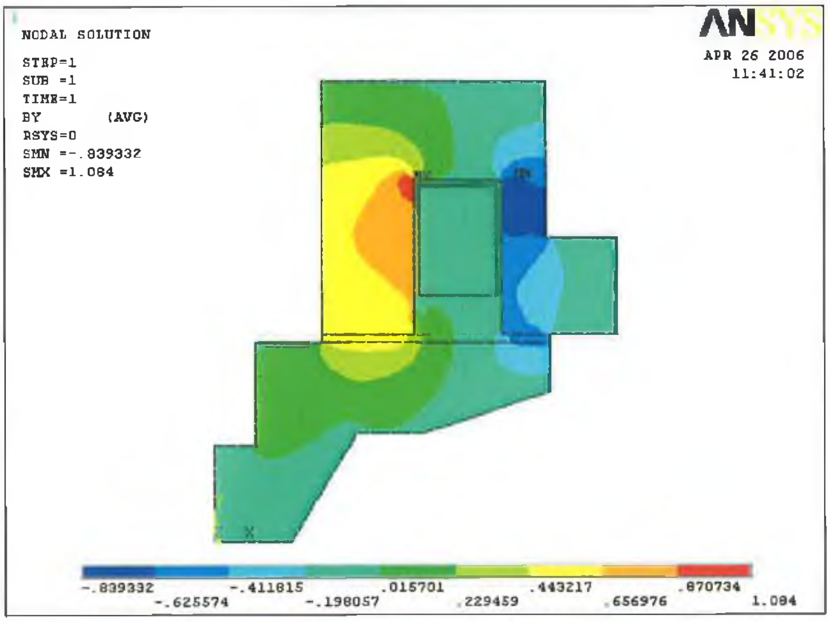

Fig. 6.29: Magnetic flux density for material 7 current times turn parameter = 160 and gap = 0.20 mm.

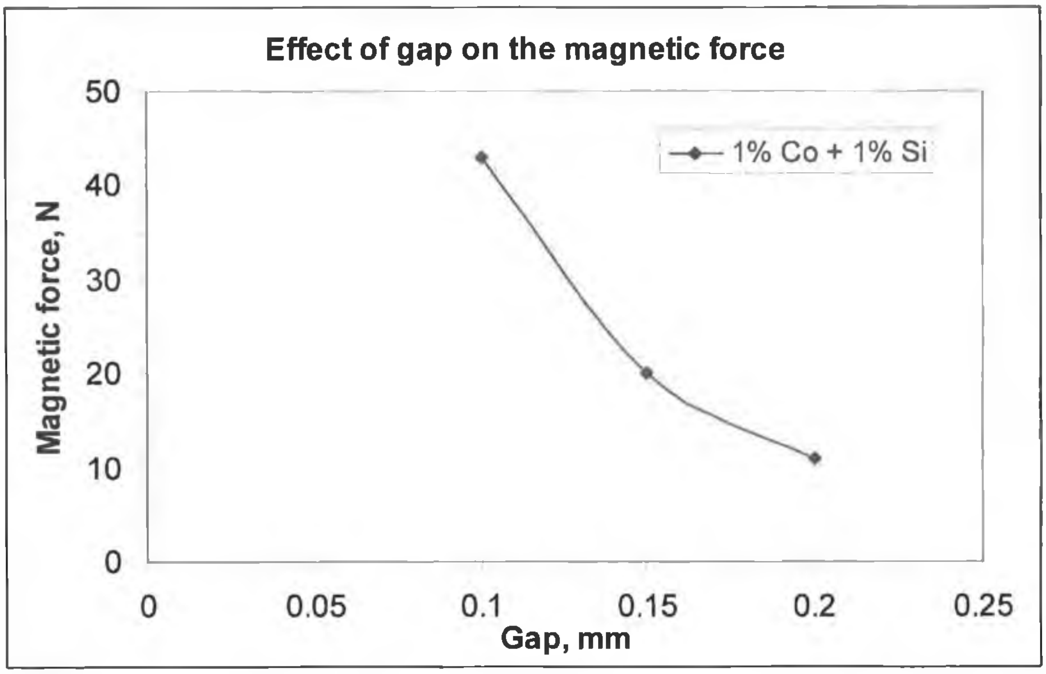

Fig. 6.30: Effect of Cobalt and Silicon content on magnetic force at different air gap sizes.

6.3.2 Material 8 (3%Co + 1%Si + 96%Fe)

The same procedure was followed. Fig. 6.31 shows the magnetic flux diagram with a gap size of 0.1 mm; the results reveal that the force is about 42 N. Fig. 6.32 indicates that for a magnetic density with a gap size of 0.15 mm, the force is 19 N. Finally, Fig. 6.33 presents the magnetic density using a gap size of 0.2 mm, with the force exhibiting a value of 11 N. The magnetic forces produced by a solenoid made from Fe-3%Co-1%Si with the different three gap sizes are presented in Fig. 6.34.

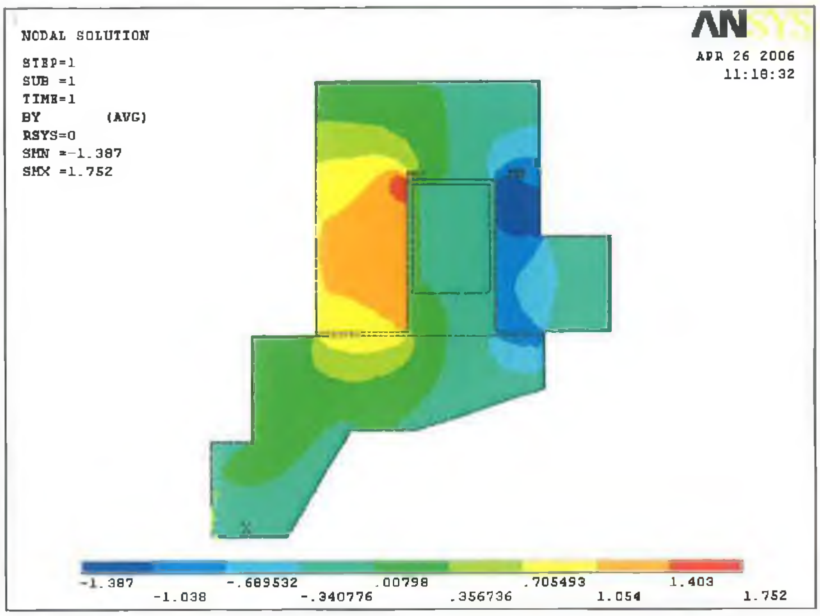

Fig. 6.31: Magnetic flux density for material 8 current times turn parameter = 160 and gap = 0.10mm.

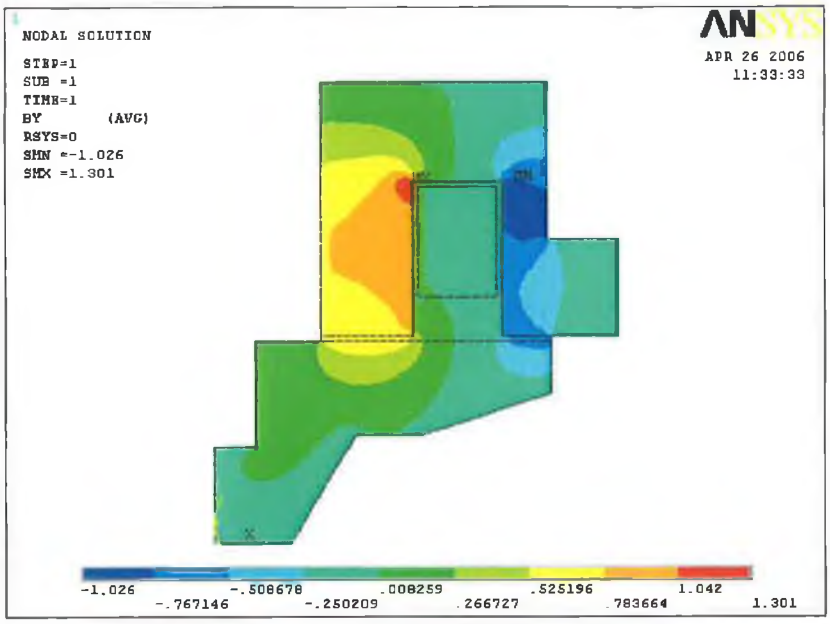

Fig. 6.32: Magnetic flux density for material 8 current times turn parameter = 160 and gap = 0.15mm.

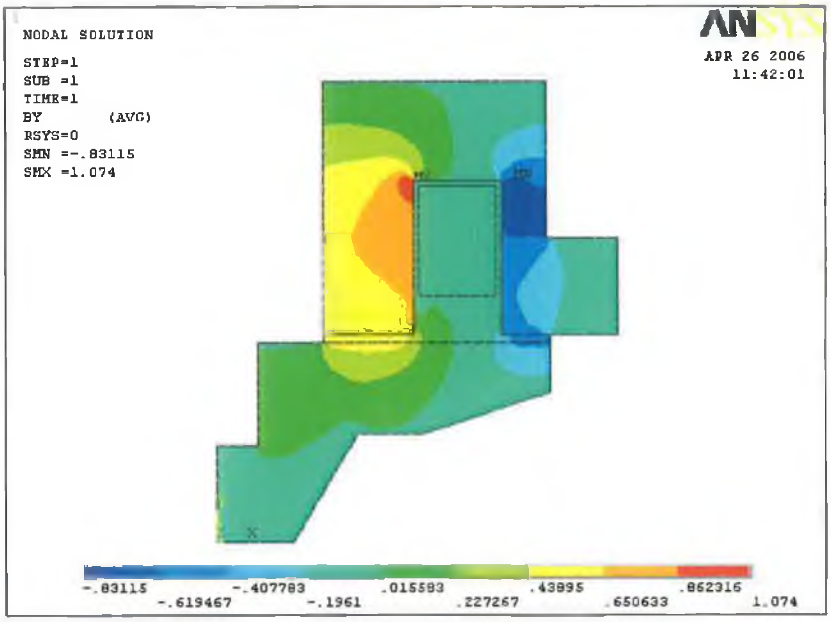

Fig. 6.33: Magnetic flux density for material 8 current times turn parameter = 160 and gap = 0.20mm.

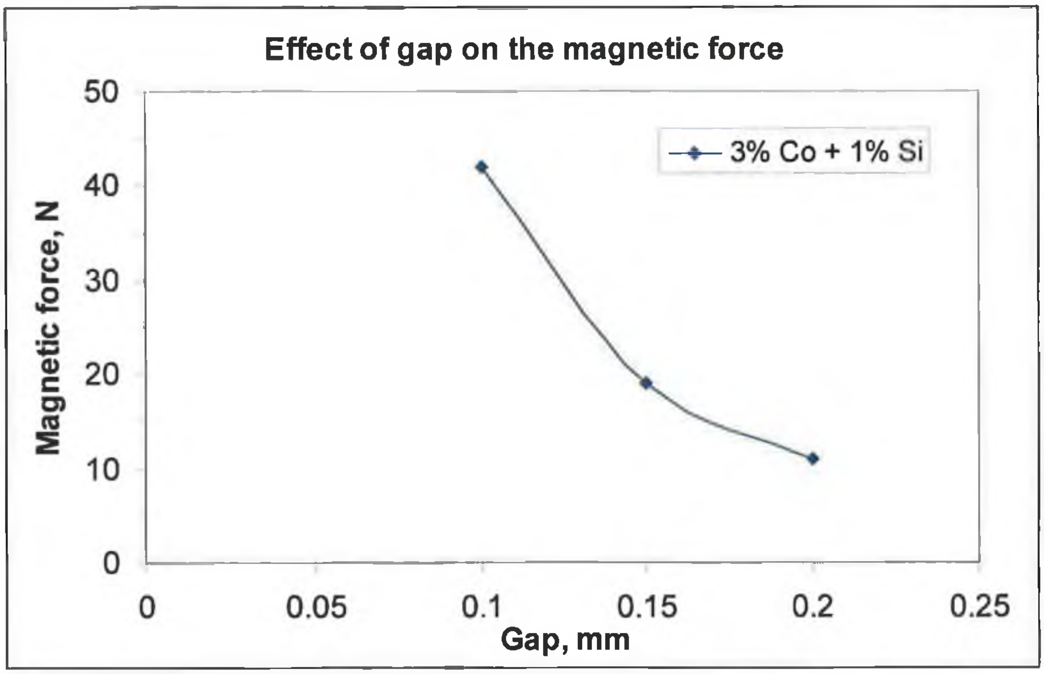

Fig. 6.34: Effect of Cobalt and Silicon content on magnetic force at different air gap sizes.

6.3.3 Material 9 (5%Co + 1%Si + 94%Fe)

Again the same procedure was followed. Fig. 6.35 shows the magnetic flux chart generated from ANSYS using a gap of 0.1 mm; the results show that the magnetic force is about 40 N. Fig. 6.36 presents the magnetic density with a gap size of 0.15 mm. The results indicate that the force is around 19 N. Fig. 6.37 presents the magnetic density using a gap of 0.2 mm. The results show that the magnetic force is about 11 N. The effect of using different gap sizes on the forces.

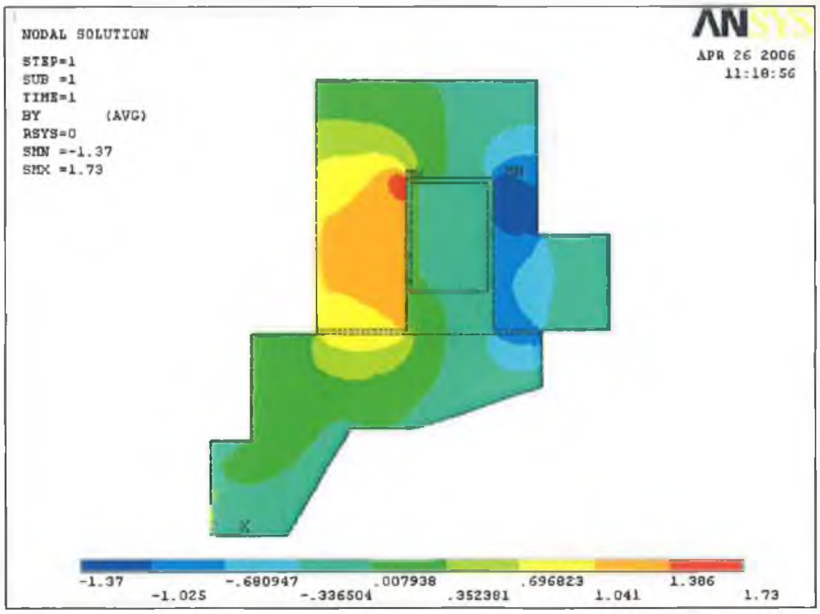

Fig. 6.35: Magnetic flux density for material 9 current times turn parameter = 160 and gap = 0.10mm.

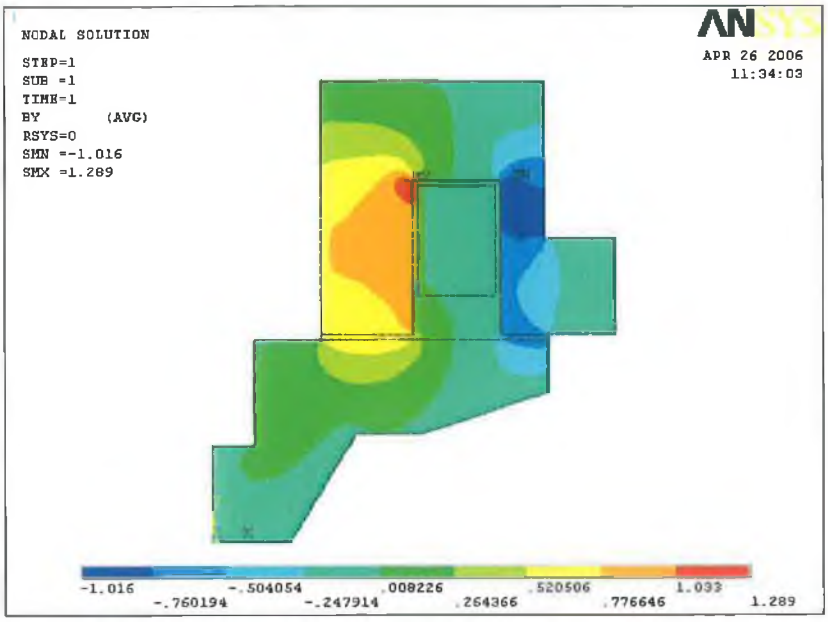

Fig. 6.36: Magnetic flux density for material 9 current times turn parameter = 160 and gap = 0.15mm.

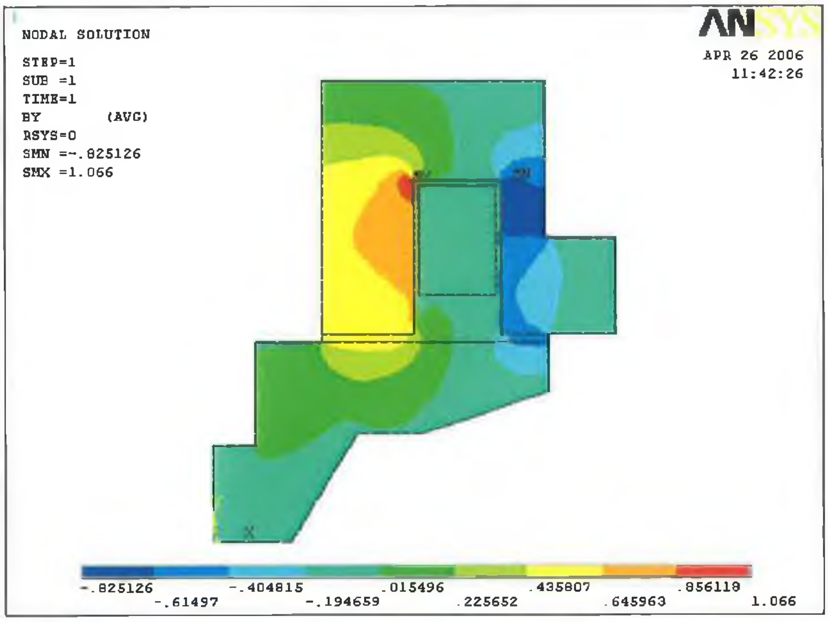

Fig. 6.37: Magnetic flux density for material 9 current times turn parameter = 160 and gap = 0.20mm.

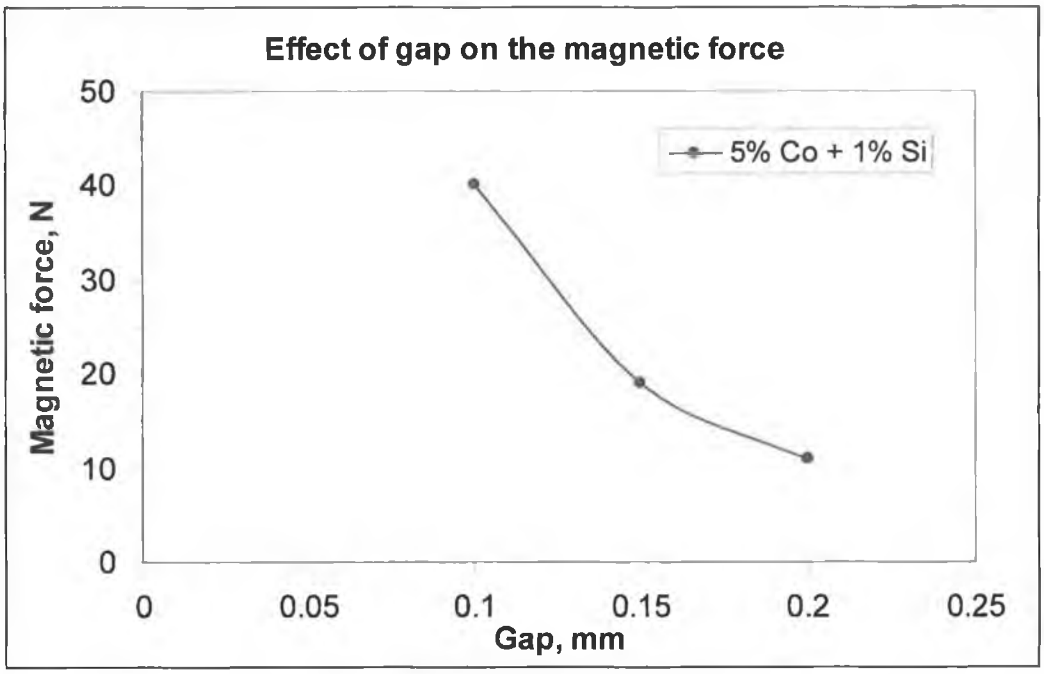

Fig. 6.38: Effect of Cobalt and Silicon content on magnetic force at different air gap sizes.

6.3.3 Material 10 (7%Co + 1%Si + 92%Fe)

The same procedure was followed. Fig. 6.39 shows the magnetic flux chart using a gap size of 0.1 mm, the results indicate that the magnetic force is about 38 N. Fig. 6.40 illustrates the magnetic density diagram with a gap of 0.15 mm. The results show that the force is approximately 19 N. Fig. 6.41 presents the magnetic density diagram with a gap size of 0.2 mm. The results show that the force is about 11 N. The effect of using different gap sizes on the forces produced by the solenoid made from Fe-7%Co-1%Si is presented in Fig. 6.42.

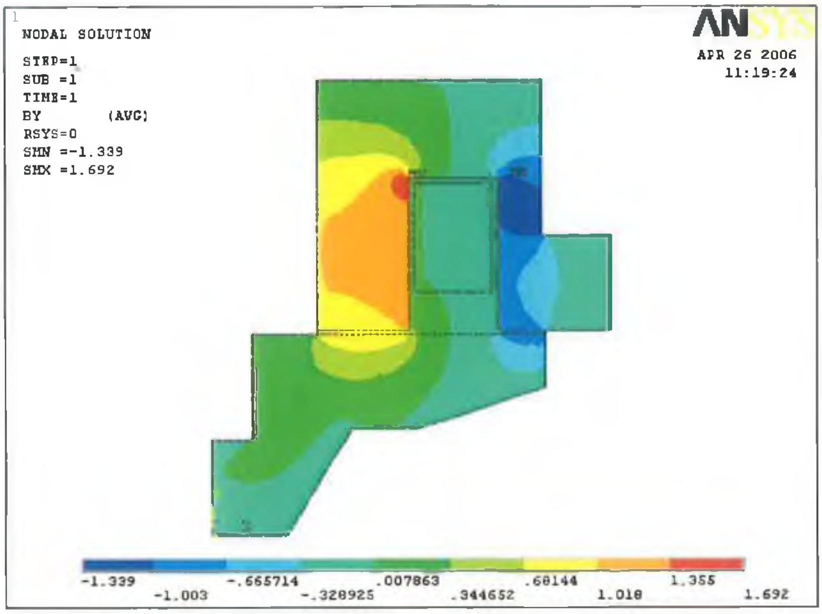

Fig. 6.39: Magnetic flux density for material 10 current times turn parameter = 160 and gap = 0.10mm.

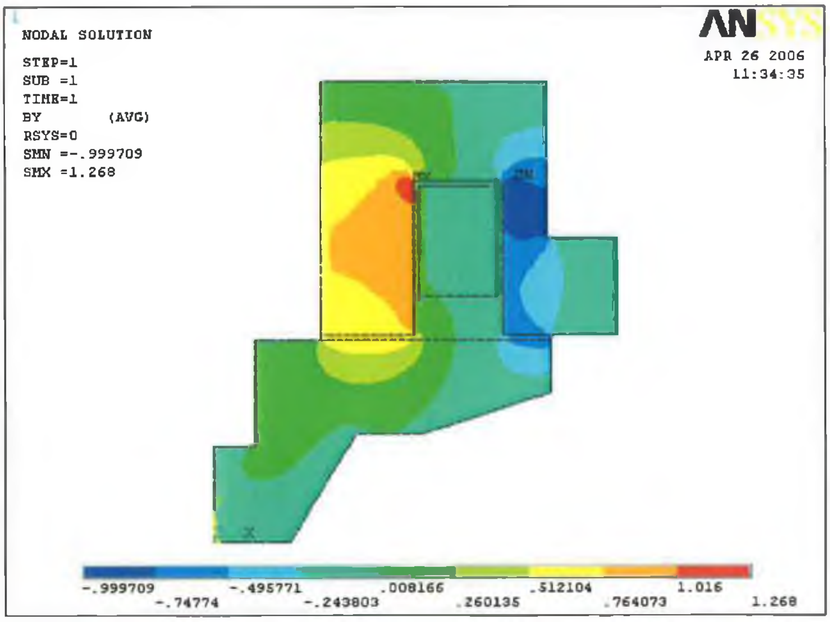

Fig. 6.40: Magnetic flux density for material 10 current times turn parameter = 160 and gap = 0.15mm.

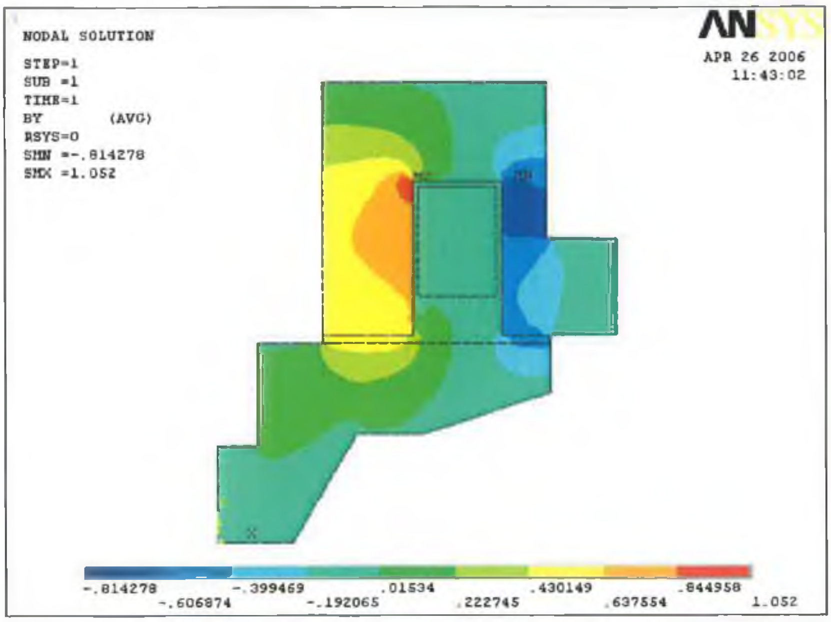

Fig. 6.41: Magnetic flux density for material 10 current times turn parameter = 160 and gap = 0.20mm.

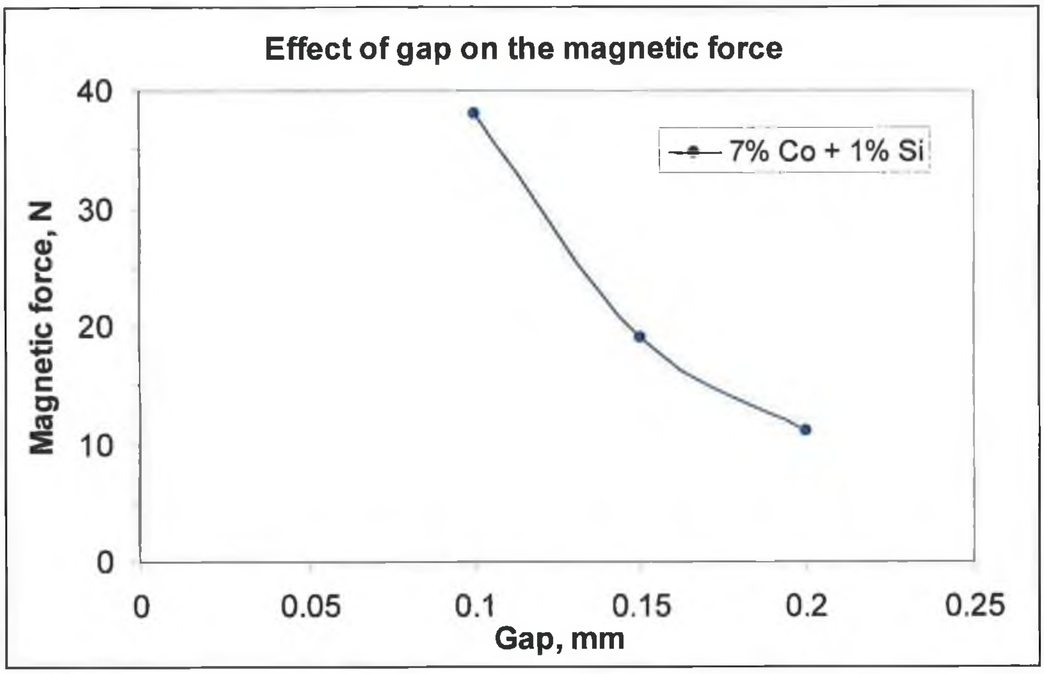

Fig. 6.42: Effect of Cobalt content on magnetic force at different air gap sizes.

It can be seen from the results of the last four materials that the force produced by the solenoid made from 1%Co+1%Si+98Fe was relatively higher than the forces produced by the solenoid made from the other ternary alloys, as illustrated in Fig. 6.43. It is evident that material 7 has relatively the softness magnetic properties among these ternary alloys.

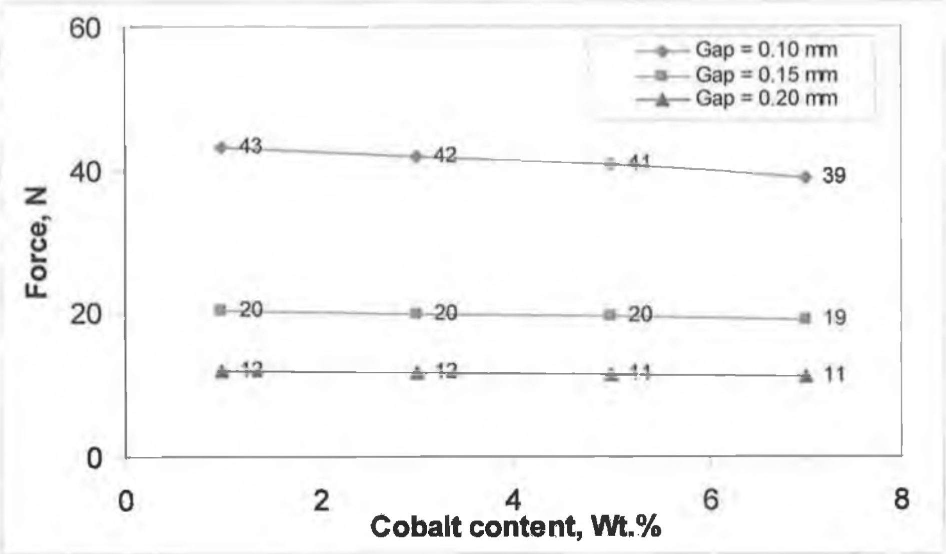

Fig. 6.43: Effect of Cobalt and 1%Si contents on magnetic force at different air gaps.

CHAPTER VII

CONCLUSION AND RECOMMENDATIONS FOR FUTURE WORK

7. CONCLUSIONS AND RECOMMENDATIONS FOR FUTURE WORK

7.1 Conclusions

The following conclusions can be drawn from this investigation:

1. High densities varying from 96% to 98% of the theoretical density can be achieved by using a high sintering temperature and a double sintering operation.
2. The Silicon content has a remarkable effect on both the compression strength and the microhardness, while Cobalt has no significant effect on either the compression strength or the microhardness.
3. A sintering temperature of 1315 °C and a sintering time of 45 min have been shown to be excellent conditions to homogenize the Silicon and the Cobalt content in the alloys.
4. Argon gas with a flow rate of 0.8 l/min during the sintering cycle has been shown to produce a good sintering atmosphere and produces parts that easy to machine.
5. All the materials developed in the study are soft magnetic materials and have narrow hysteresis loops in their B-H curves.
6. The higher the Silicon percentage the better the soft magnetic properties that are produced. A maximum permeability of 1102 is achieved for the 3% Silicon + 97%Fe alloy. Cobalt tends to improve the soft magnetic properties if added to iron up to 3%.
7. Alloying iron with Cobalt percentages of 1% or 3% leads to soft magnetic materials with better magnetic properties.
8. Alloying iron with Cobalt and 1%Si leads to soft magnetic materials but their magnetic properties become harder as the Cobalt content increases.
9. Good electromagnetic performances and higher forces can be obtained using the materials with 2% or 3%Silicon + Fe Balance.
10. The FEA has demonstrated good results for estimating the magnetic field in the solenoid used in this work.

11. The same FEA procedure can be used to predict the magnetic field and the force for many other types of solenoid.

7.2 Recommendations for Future Work

1. Since the purity of the iron powder, which was used was only 97%. It is recommended that metal powders with higher purity (i.e. higher than 99%) should be used to developed soft magnetic materials which would have even better magnetic properties.
2. It is recommended that the solenoid performance could be improved further by establishing an optimal design method using procedures such as Design of Experiment (DOE) or Response Surface Methodology (RSM), considering the structural parameters of the solenoid, the applied current, the coil position and a range of soft magnetic materials.
3. It is recommended that the effect of alloying iron with different percentages of Silicon (2 and 4%) and different percentages of Cobalt (2 and 3%) could be investigated following the same procedure that was applied in this study.

REFERENCES

REFERENCES

---

[1] A Metal Powder Industries Foundation, http://www.mpif.org, on .08.2005.

[2] R. M. German, Powder metallurgy of iron and steel, John Wiley & Sons, Inc., (1998).

[3] http://www.materials.uq.edu.au/powdermetallurgy/background.html, on 08.2005.

[4] European Powder Metallurgy Association. http://www.epma.com, on 08.2005.

[5] R. M. German, Powder Metallurgy Science, Princeton, N. J; Metal Powder Industries Federation, (1984).

[6] T. Hummler and R. Oberacker, AN introduction to powder metallurgy, London; Institute of Materials, (1993).

[7] Cold isostatic pressing-CIP http://www.designinsite.dk/htmsider/p1007.htm, 05-01-2006.

[8] B. D. Cullity, Introduction to Magnetic Materials, Addison-Wesley, 1962.

[9] Magnetic Properties Chapter (18) http://www.ie.sharif.edu/~ramez/em/chap18-c, on 09.2005.

[10] http://www.aacg.bham.ac.uk/magnetic_materials/soft_magnets.htm on 09.2005

[11] NDT Resource centre. Hysteresis Loop, 30th January 2004. http://www.ndt-ed.org/EducationResources/CommunityCollege/MagParticle/Physics/HysteresisLoop.htm.

[12] http://www.wisegeek.com/what-is-a-solenoid.htm?referrer=adwords_campai, on 08.2005.

[13] F. J. Semel and S. H .Luk, Continuing improvements in binder treatment technology, Journal of Advances in Powder Metallurgy & Particulate Materials, (1996), Vol. 4. No. 13, pp. 353-362.

[14] V. A. Gaidarov and A. T. Mamedov, Effect of zinc stearate on the properties of sintered products, Journal of Soviet powder metal & Metal ceramics, (Aug 1987), Vol. 29, No. 8, pp. 636 - 640.

[15] K. Ueda, T. Machida, M. Iwakiri and H. Fukagawa, Effects of powder lubricants and compaction temperature on the higher density of iron-based green compacts, Hitachi Powdered Metals Technical Report, Vol. 1, (2002), pp. 29 – 38.

[16] A. I. Lawrence, S. H. Luk and J. A. Hamill, A performance comparison of current P/M lubricants and routes to improvement, International Conference on Powder Metallurgy & Particulate Materials, June 29-July 2, 1997 Chicago, IL USA, pp. 1- 22.

[17] A. Kao and M. J. Koczak, Mixing and compacting behaviour of ferrous powders, International Journal of Powder Metal and Powder Technology, (1980), Vol.16, No.2, pp. 105-121.

[18] J. M. Wheatley and G .C .Smith, the fatigue strength of sintered iron compacts, International Journal of Powder Metal, Vol. 6,(1963), pp.141.

[19] A. T. Mamadov, procedure for compaction using gas removal from moulds-mathematical analysis, Journal of Powder Metallurgy, No. 5/6, (1994), pp.34-39.

[20] D.T. Gethin, An investigation of powder compaction processes, International Journal of powder Metallurgy, Vol.30, No. 4, (1994), pp. 385-398.

[21] A. Eksi and S. Saritas, Effects of powder hardness and particle size on the densification of cold isostatically pressed powders, Turkish Journal of Eng. Environmental Science, Vol. 26, (2002), pp 377-384.

[22] P. Wiest, Symposium sur la metallurgyie de poudres, Saint Germain edition metaux (1964), pp. 329.

[23] A. Munitz, Z. Livne, J. C. Rawers, J. S. Adams, and R. J. Fields, Effect of nitrogen on the mechanical properties and microstructure of hot isostatically pressed nanograined Fe, Journal of Nanostructured Materials, Vol. 11, No. 2, (1999), pp. 159-177.

[24] J. A .Bas, J. A. Calero, M. J. Dougan, Sintering soft magnetic materials properties and applications, Journal of Magnetism and Magnetic Materials, Vol. 254-255, (2003), pp. 391-398.

[25] H. G. Rutz and F.G. Hanejko, High density processing of high performance ferrous materials, Advances in Powder Metallurgy & Particulate Materials, Vol. 5, (1994), pp. 117- 133.

[26] G. Roberts, A. Davidson, S. Gair and J. Hajto, An overview of the powder processing of soft magnetic composites, Engineering Science and Education Journal, Dec. (2001), pp. 237- 240.

[27] J. W. Schaberl, M. C. Baran, M. L. Marucci and R. A. Posteraro, Economics and benefits of high temperature sintering of high performance alloys, Inter. Conference on Powder Metallurgy & Particulate Materials, June 16 -21, 2002, Orlando, Florida USA.

[28] J. A. Varela and O. J. Whittemore, Pore size evolution during sintering of ceramic oxides, Ceramics International Journal, Vol. 16, (1990), pp. 177-189.

[29] C Lall, Soft Magnetism Fundamentals for Powder Metallurgy and Metal Injection Molding, Metal Powder Inductries Federation, USA, (1992).

[30] L. P. Lefebvre, S. Pelletir and C. Gelinas, Effect of electrical resistivity on core losses in soft magnetic iron powder materials, Journal of Magnetism and Magnetic Materials, Vol. 176, (1997), pp. L93-L96.

[31] C. W. Chen, Magnetism and Metallurgy of Soft Magnetic Materials, 2nd Edition, Dover publications, Inc, New York, (1986).

[32] J. A. Bas, J. Puing and C. B. Molins, Soft magnetic materials in P/M current applications and state-of-the-art, Proceedings of the 1988 International Powder Metallurgy Conference, June 5-10, 1988 Orlando, Florida, pp. 745- 756.

[33] E. Gumlich and P. Goerens, Magnetic properties of Fe-C and Fe-Si alloys, Trans. of Faraday Soc. Vol. 8, (1912), pp. 98-144.

[34] H.G. Rutz, F. G. Hanejko, and G. W. Ellis, The manufacture of electromagnetic components by the powder metallurgy process, International conference on powder metallurgy June 29-July 2, 1997 Chicago, IL USA, pp. 1-16.

[35] F. G. Hanejko, G. W. Ellis and T. J. Hale, Application of high performance material processing electromagnetic products , International Conference and Exhibition on Powder Metallurgy and Particulate Materials; Las Vegas, NV; USA; 31 May-4 June 1999. pp. 8.13-8.26.

[36] P. Jansson, Soft magnetic materials for ac applications, Journal of Powder Metallurgy, Vol. 35, No. 1, (1992), pp. 63-66.

[37] C. Lall and L. W. Baum, High performance soft magnetic components by powder metallurgy and metal injection molding, Modern Developments in Powder Metallurgy, Vol. 18, (1988) , compiled by P. U. Gummeson and D. A. Gustafson, pp.363 - 389.

[38] F. G. Hanejko, Howard G. Rutz and C. G. Oliver, Effect of processing and material on soft magnetic performance of powder metallurgy parts, Presented at the 1992 powder metallurgy world congress, Vol. 6, San Francisco, CA, June 21-26, 1992, pp. 375 - 404.

[39] J. A. Bas and C. Molins Jr, Effect of machining procedures on the magnetic properties of several sintered soft magnetic materials, PM'86 proceedings, (1986).

[40] A. G. Olabi and M. Ricco, Optimization of multi-purpose solenoid actuator used for automotive application, in The Proceeding of Advanced Materials and Process Technology Conference AMPT2001, Madrid, Spain, September 21-23, pp. 745-752.

[41] T. Kajjma, Development of a high-speed solenoid Valve: Investigation of energizing circuits, IEEE Transactions on Industrial Electronics, IE, Vol. 40, Aug. 1993, pp. 428-435.

[42] M. Ricco, S. D. Matthaeis and A. G. Olabi, Simulation of the magnetic properties for common rail electro-injector, Journal of Materials Processing Technology, Volumes 155-156, (2004), pp.1611-1615 .

[43] G. Tao, H. Y. Chen, Y. Y. J, and Z. B. He, Optimal design of the magnetic field of high-speed response solenoid valve, Journal of Materials Processing Technology, Vol. 129, 2002, pp.555-558.

[44] Y. Kano and K. Maeda ,Analysis and reformation of characteristic of linear electromagnetic solenoid, IEEE Transactions on Magnetics, Vol.29, No.6, NOV (1993), pp. 2929-2931.

[45] D. Jiles, Introduction to magnetism and magnetic materials, 2nd Edition, Chapman & Hall, USA, (1998).

[46] Al-Tousi, Effect of sintering temperature on the high strain rate property of iron powder compacts, PhD. Theses, DCU, (1992).

[47] K. S. Tan, P. Hing and P. Ramalingam, The elastic moduli and diametrical compressive fracture stress of Al203-Zro_2, Journal of Phys.D: Appl. Vol.30,1(997),pp. 1029-1037.

[48] Metals Handbook, Powder Metallurgy, American Society for Metals, Ninth Edition, Vol. 7, (1992).

[49] Metals Handbook, Mechanical testing, American Society for Metals, Ninth Edition, Vol. 8, (1992).

[50] Metals Handbook, Metallographic and Microstructures, American Society for Metals, Ninth Edition, Vol. 9, (1992).

[51] M. Saeed, Finite element analysis: Theory and application with ANSYS, 2nd Edition, Pearson Education, Inc., (2003), pp. 5-8.

[52] S. I. Krishnamachari, Applied stress analysis of plastics: a mechanical engineering approach, New York: Van Nostrand Reinhold, (1993), chapter 8 Finite element Method: an introduction p. 450.

[53] http://www.fea-optimization.com/ans_macro/ANS-history.txt, on 27.11.2005.

[54] R. H. Yu, S. Basu, L. Ren, Y. Zhang, A. P. Majidi, K. M. Unruh and J. Q. Xiao, High temperature soft magnetic materials: FeCo alloys and composites, IEEE Transaction on Magnetics, Vol. 36, No. 5, Sept. (2000), pp. 3388 -3393.

[55] Abdelmuniem M. Alsebaie, Characterization of Alumina-Zirconia Composites Produced By Micron-Sized Powders, M. Sc. Thesis, DCU, 2006.

APPENDICES

APPENDIX A

Magnetic test result for Si-Fe alloys

KJS Associates, Inc. Model SMT-600 Hysteresigraph System

File Name	MS14671.csv	**Test Date/Time**	8 Dec 2005	
Sample I.D.	Sample 1 1% Si 99% Fe	**Test Procedure**	ASTM A773/A773M-01	
Batch I.D.	Dublin City University 20051539	**Operator/version**	JDC	2.0.3.0
Comments	KJS Associates Div. - Excellence in magnetics since 1968.			

SAMPLE INFORMATION		
Diameter	0.6716	in
B Coil Turns	9	
B Coil Resistance	0.4	Ohms
B Coil Wire Thickness	0.011	in
Tape Thickness	0.004	in
Cross Sectional Shape	Circular	
Area Calculation Method	Dimension	
Sample Area	2.28549	cm^2
B Coil Area	2.41663	cm^2

TEST PARAMETERS		
Temperature	25	C
Max. Measured B	15351	G
Max. Measured H	1040	Oe
Step Delay	0	s

TEST SUMMARY		
Remanence Br	5792	G
Coercive Field Hc	3.7	Oe
Max. Permeability umax	715	
B @ Max. Permeability	5364	G
H @ Max. Permeability	7.505	Oe
Demag. Offset	44	G
Test Type	DC Yoke	

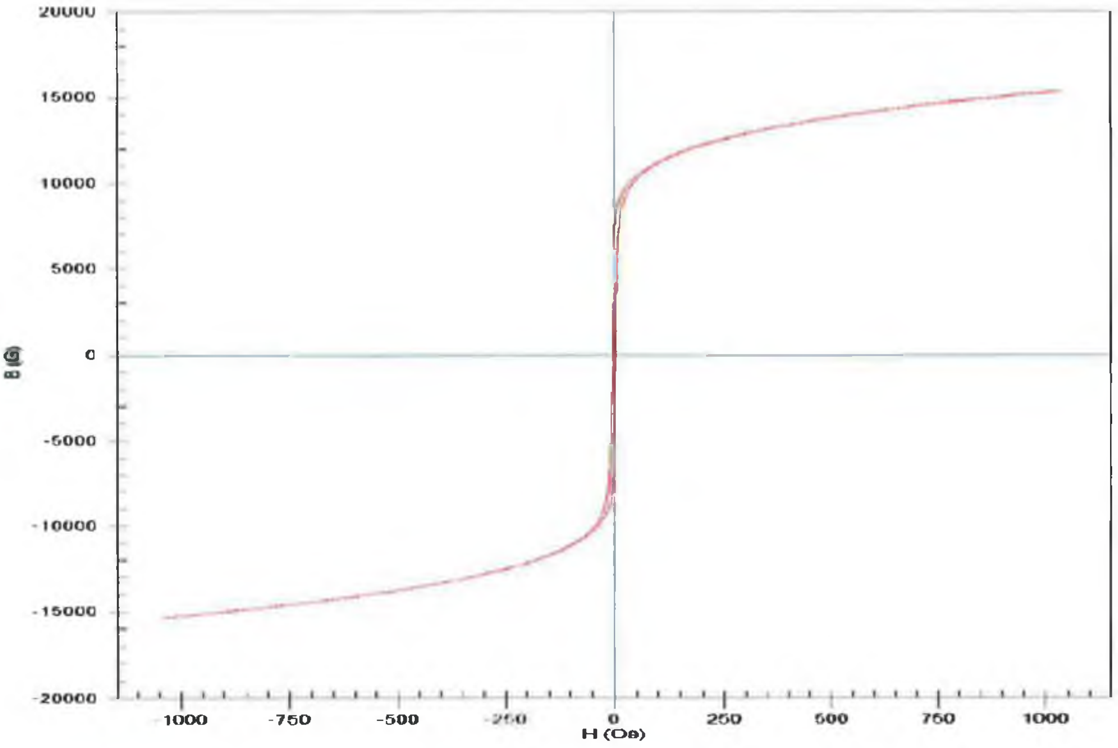

KJS Associates Div. - Excellence in magnetics since 1968.

KJS Associates, Inc. Model SMT-600 Hysteresigraph System

File Name	MS14672.csv	**Test Date/Time**	8 Dec 2005	
Sample I.D.	Sample 2 2% Si 98% Fe	**Test Procedure**	ASTM A773/A773M-01	
Batch I.D.	Dublin City University 20051539	**Operator/version**	JDC	2.0.3.0
Comments	KJS Associates Div. - Excellence in magnetics since 1968.			

SAMPLE INFORMATION		
Diameter	0.6676	in
B Coil Turns	9	
B Coil Resistance	0.5	Ohms
B Coil Wire Thickness	0.011	in
Tape Thickness	0.004	in
Cross Sectional Shape	Circular	
Area Calculation Method	Dimension	
Sample Area	2.25834	cm^2
B Coil Area	2.38872	cm^2

TEST PARAMETERS		
Temperature	25	C
Max. Measured B	19606	G
Max. Measured H	1033	Oe
Step Delay	0	s
TEST SUMMARY		
Remanence Br	5069	G
Coercive Field Hc	2.34	Oe
Max. Permeability umax	1098	
B @ Max. Permeability	7759	G
H @ Max. Permeability	7.065	Oe
Demag. Offset	39	G
Test Type	DC Yoke	

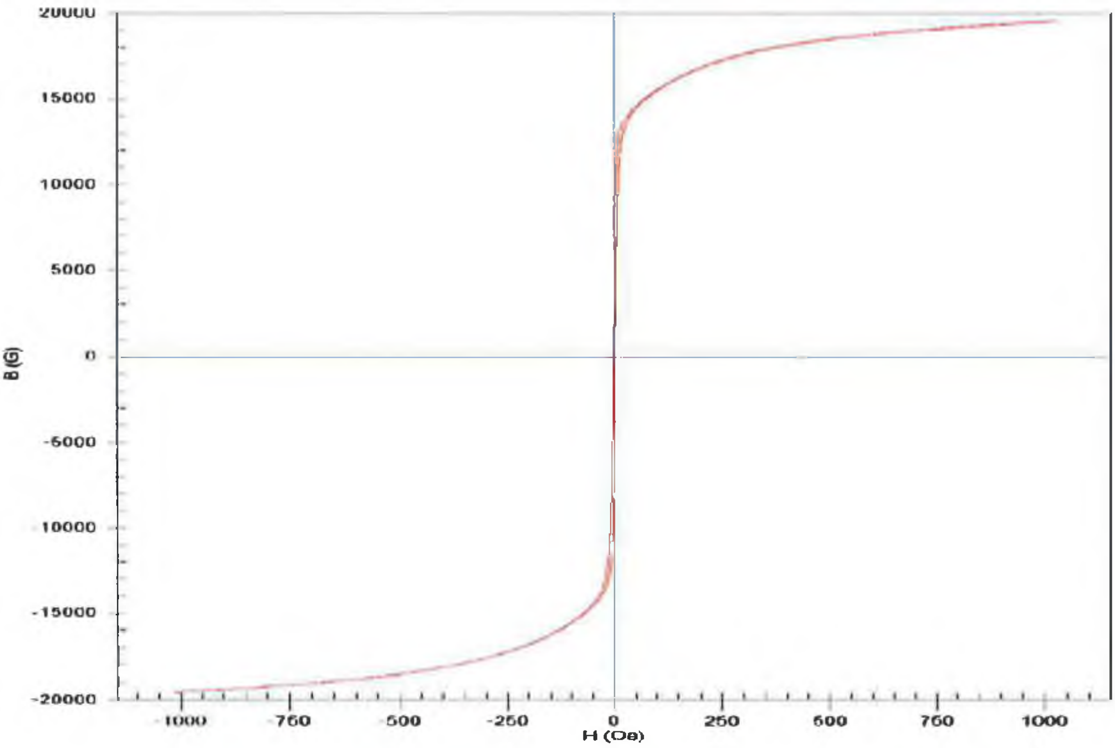

KJS Associates Div. - Excellence in magnetics since 1968.

KJS Associates, Inc. Model SMT-600 Hysteresigraph System

File Name	MS14673.csv	**Test Date/Time**	8 Dec 2005	
Sample I.D.	Sample 3 3% Si 97% Fe	**Test Procedure**	ASTM A773/A773M-01	
Batch I.D.	Dublin City University 20051539	**Operator/version**	JDC	2.0.3.0
Comments	KJS Associates Div. - Excellence in magnetics since 1968.			

SAMPLE INFORMATION		
Diameter	0.6641	in
B Coil Turns	9	
B Coil Resistance	0.4	Ohms
B Coil Wire Thickness	0.011	in
Tape Thickness	0.004	in
Cross Sectional Shape	Circular	
Area Calculation Method	Dimension	
Sample Area	2.23473	cm^2
B Coil Area	2.36443	cm^2

TEST PARAMETERS		
Temperature	25	C
Max. Measured B	19551	G
Max. Measured H	1055	Oe
Step Delay	0	s
TEST SUMMARY		
Remanence Br	4108	G
Coercive Field Hc	2.08	Oe
Max. Permeability umax	1102	
B @ Max. Permeability	7267	G
H @ Max. Permeability	6.592	Oe
Demag. Offset	47	G
Test Type	DC Yoke	

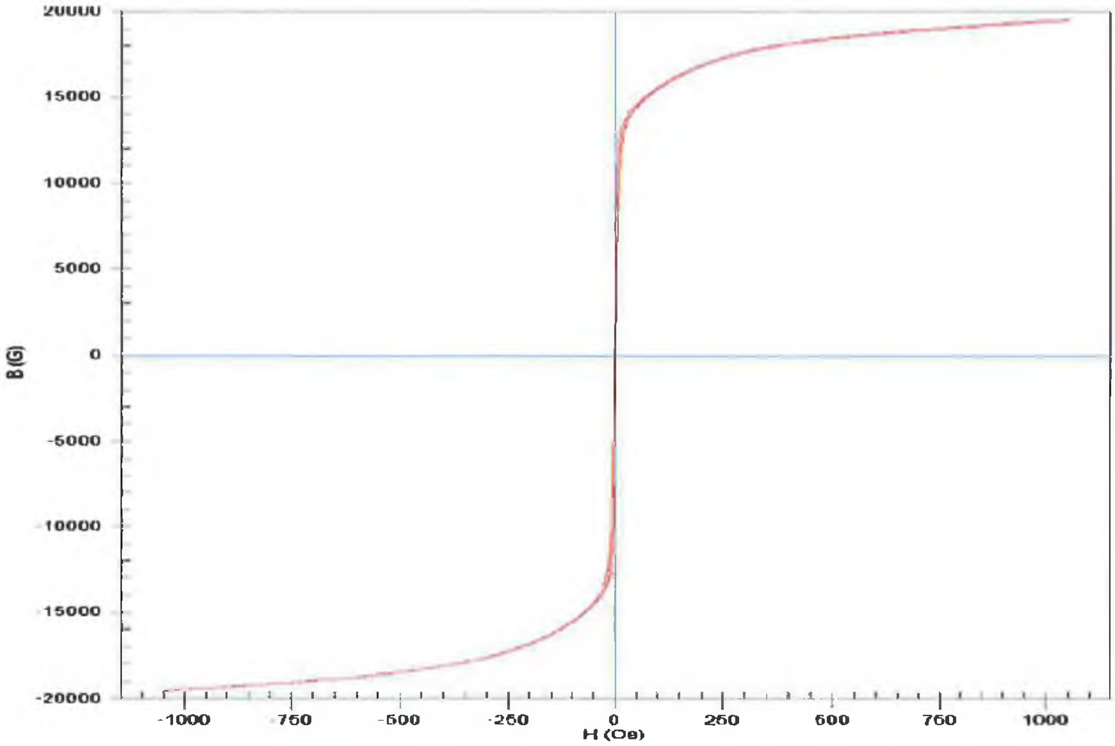

KJS Associates Div. - Excellence in magnetics since 1968.

KJS Associates, Inc. Model SMT-600 Hysteresigraph System

Filename	MS14671, 72 ,73 COMPOSITE.csv	**Print Date**	8 Dec 2005
Test Procedure	ASTM A773/A773M-01	**Version**	2.0.3.0

Comments KJS Associates Div. - Excellence in magnetics since 1968.

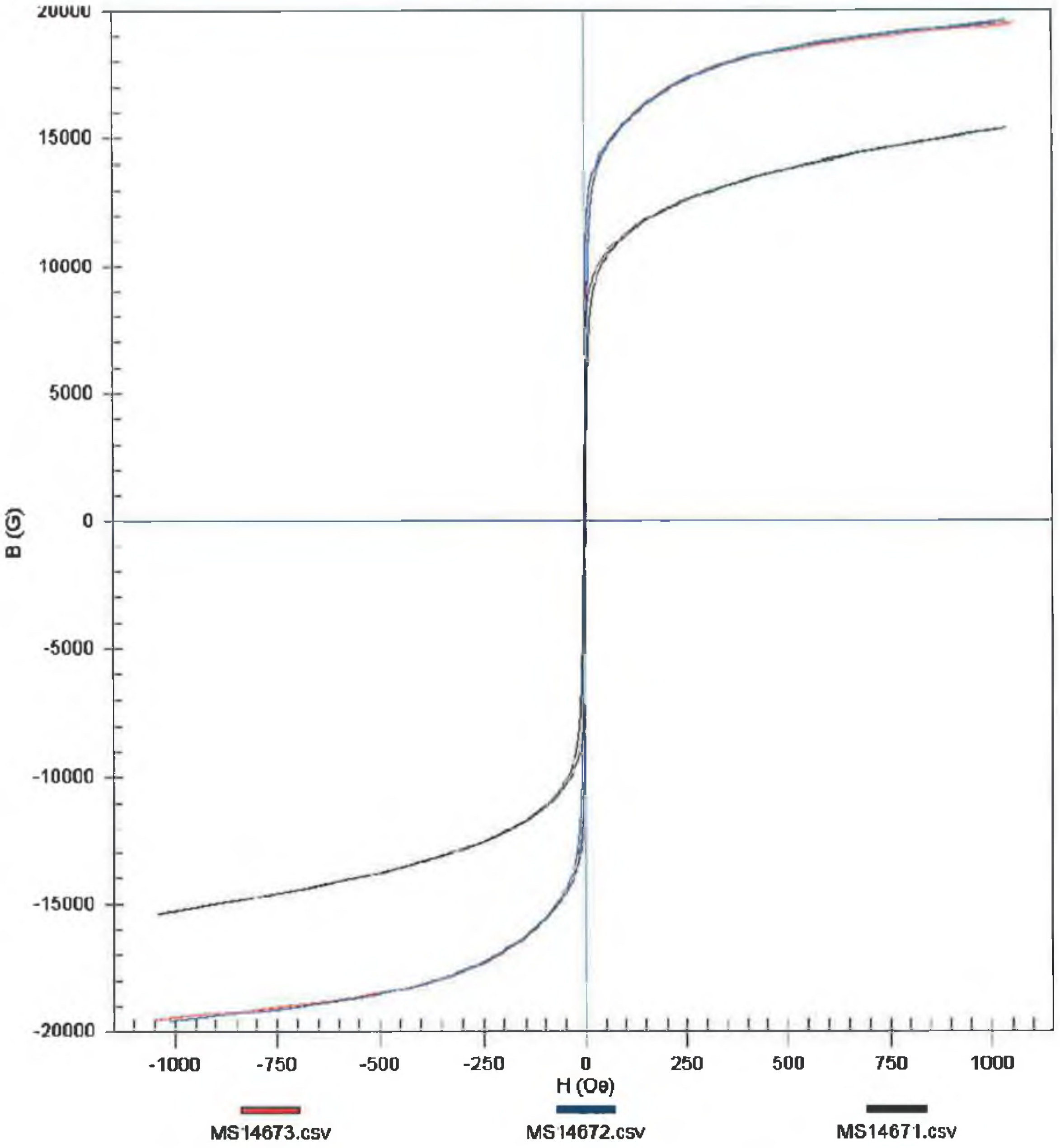

KJS Associates, Inc. Model SMT-600 Hysteresigraph System

Filename	MS14671, 72 ,73 COMPOSITE.csv	**Print Date**	8 Dec 2005
Test Procedure	ASTM A773/A773M-01	**Version**	2.0.3.0

Comments KJS Associates Div. - Excellence in magnetics since 1968.

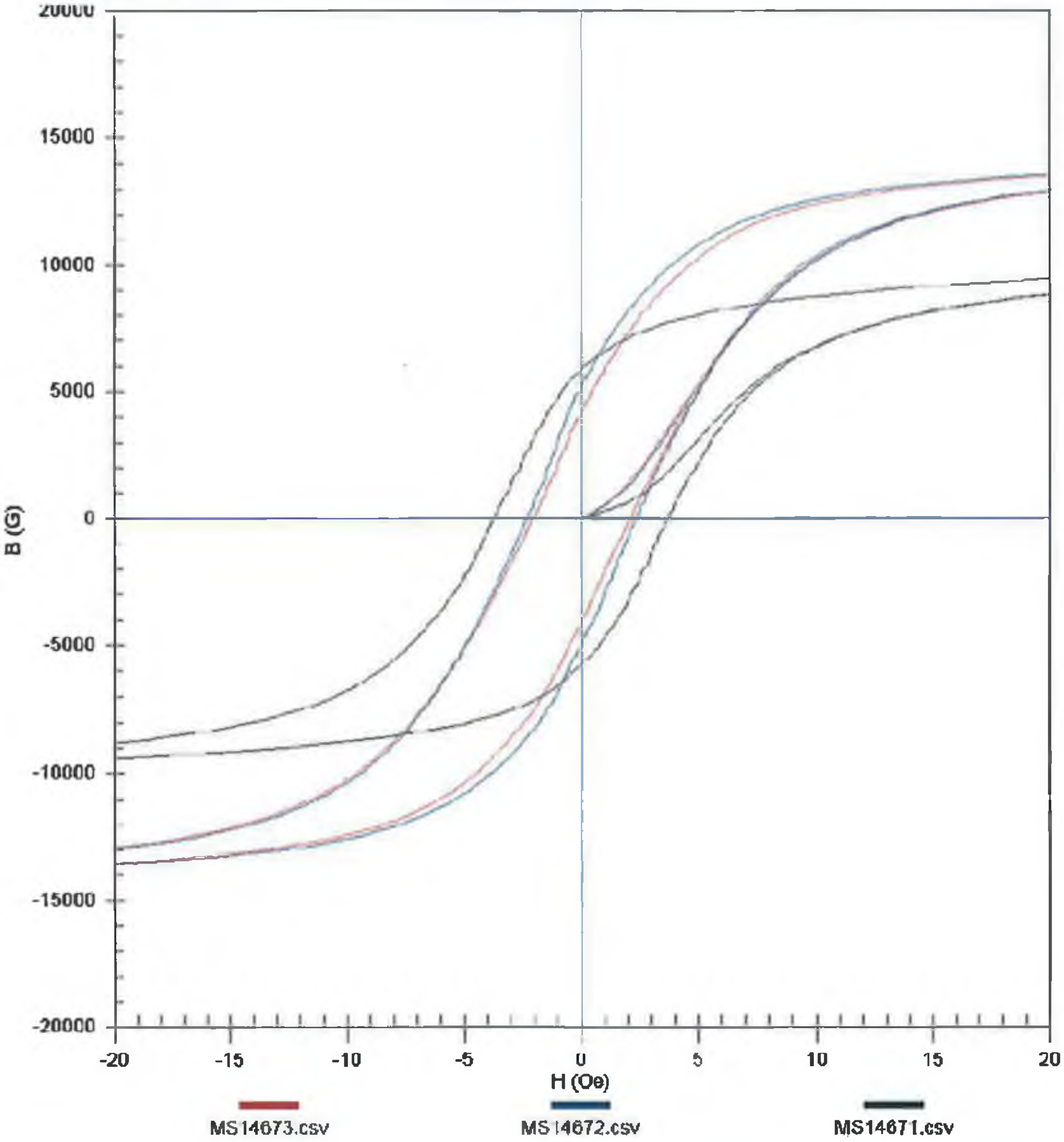

KJS Associates Div. - Excellence In Magnetics Since 1968.

APPENDIX B

Magnetic test result for Co-Fe alloys

KJS Associates, Inc. Model SMT-600 Hysteresigraph System

File Name	MS14674.csv	**Test Date/Time**	8 Dec 2005	
Sample I.D.	Sample 4 1% Co 99% Fe	**Test Procedure**	ASTM A773/A773M-01	
Batch I.D.	Dublin City University 20051539	**Operator/version**	JDC	2.0.3.0
Comments	KJS Associates Div. - Excellence in magnetics since 1968.			

SAMPLE INFORMATION		
Diameter	0.6703	in
B Coil Turns	9	
B Coil Resistance	0.5	Ohms
B Coil Wire Thickness	0.011	in
Tape Thickness	0.004	in
Cross Sectional Shape	Circular	
Area Calculation Method	Dimension	
Sample Area	2.27665	cm^2
B Coil Area	2.40754	cm^2

TEST PARAMETERS		
Temperature	25	C
Max. Measured B	15703	G
Max. Measured H	1028	Oe
Step Delay	0	s
TEST SUMMARY		
Remanence Br	6155	G
Coercive Field Hc	3.1	Oe
Max. Permeability umax	885	
B @ Max. Permeability	5935	G
H @ Max. Permeability	6.708	Oe
Demag. Offset	16	G
Test Type	DC Yoke	

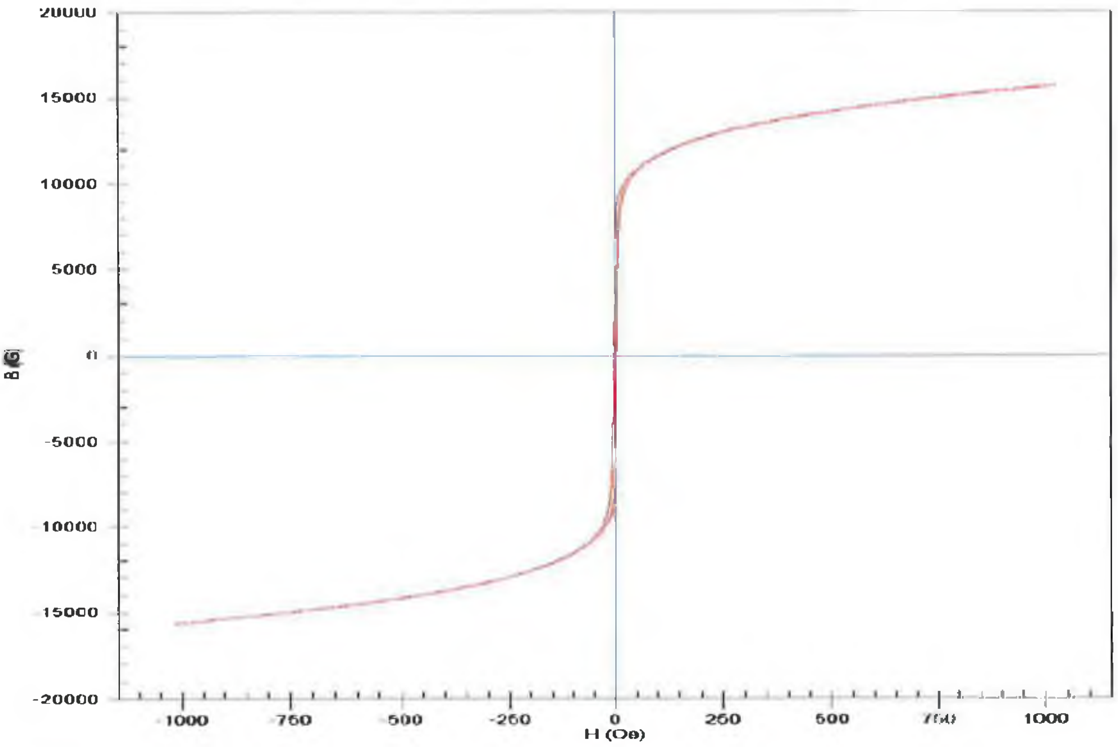

KJS Associates Div. - Excellence in magnetics since 1968.

KJS Associates, Inc. Model SMT-600 Hysteresigraph System

File Name	MS14675.csv	**Test Date/Time**	8 Dec 2005	
Sample I.D.	Sample 5 3% Co 97% Fe	**Test Procedure**	ASTM A773/A773M-01	
Batch I.D.	Dublin City University 20051539	**Operator/version**	JDC	2.0.3.0
Comments	KJS Associates Div. - Excellence in magnetics since 1968.			

SAMPLE INFORMATION		
Diameter	0.6717	in
B Coil Turns	9	
B Coil Resistance	0.4	Ohms
B Coil Wire Thickness	0.011	in
Tape Thickness	0.004	in
Cross Sectional Shape	Circular	
Area Calculation Method	Dimension	
Sample Area	2.28617	cm^2
B Coil Area	2.41733	cm^2

TEST PARAMETERS		
Temperature	25	C
Max. Measured B	16185	G
Max. Measured H	1033	Oe
Step Delay	0	s
TEST SUMMARY		
Remanence Br	5407	G
Coercive Field Hc	2.42	Oe
Max. Permeability umax	1055	
B @ Max. Permeability	5915	G
H @ Max. Permeability	5.609	Oe
Demag. Offset	-5	G
Test Type	DC Yoke	

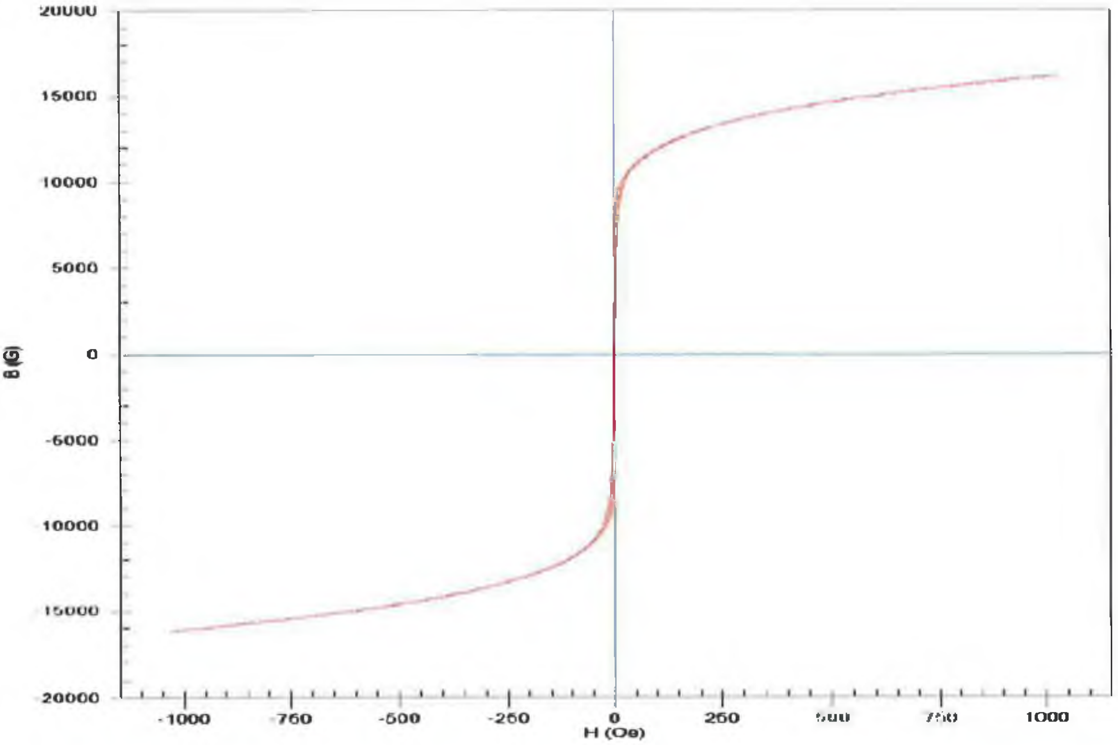

KJS Associates, Inc. Model SMT-600 Hysteresigraph System

File Name	MS14676.csv	**Test Date/Time**	8 Dec 2005	
Sample I.D.	Sample 6 5% Co 95% Fe	**Test Procedure**	ASTM A773/A773M-01	
Batch I.D.	Dublin City University 20051539	**Operator/version**	JDC	2.0.3.0
Comments	KJS Associates Div. - Excellence in magnetics since 1968.			

SAMPLE INFORMATION		
Diameter	0.6718	in
B Coil Turns	9	
B Coil Resistance	0.5	Ohms
B Coil Wire Thickness	0.011	in
Tape Thickness	0.004	in
Cross Sectional Shape	Circular	
Area Calculation Method	Dimension	
Sample Area	2.28685	cm^2
B Coil Area	2.41803	cm^2

TEST PARAMETERS		
Temperature	25	C
Max. Measured B	15560	G
Max. Measured H	1041	Oe
Step Delay	0	s
TEST SUMMARY		
Remanence Br	3639	G
Coercive Field Hc	2.7	Oe
Max. Permeability umax	701	
B @ Max. Permeability	3667	G
H @ Max. Permeability	5.228	Oe
Demag. Offset	-54	G
Test Type	DC Yoke	

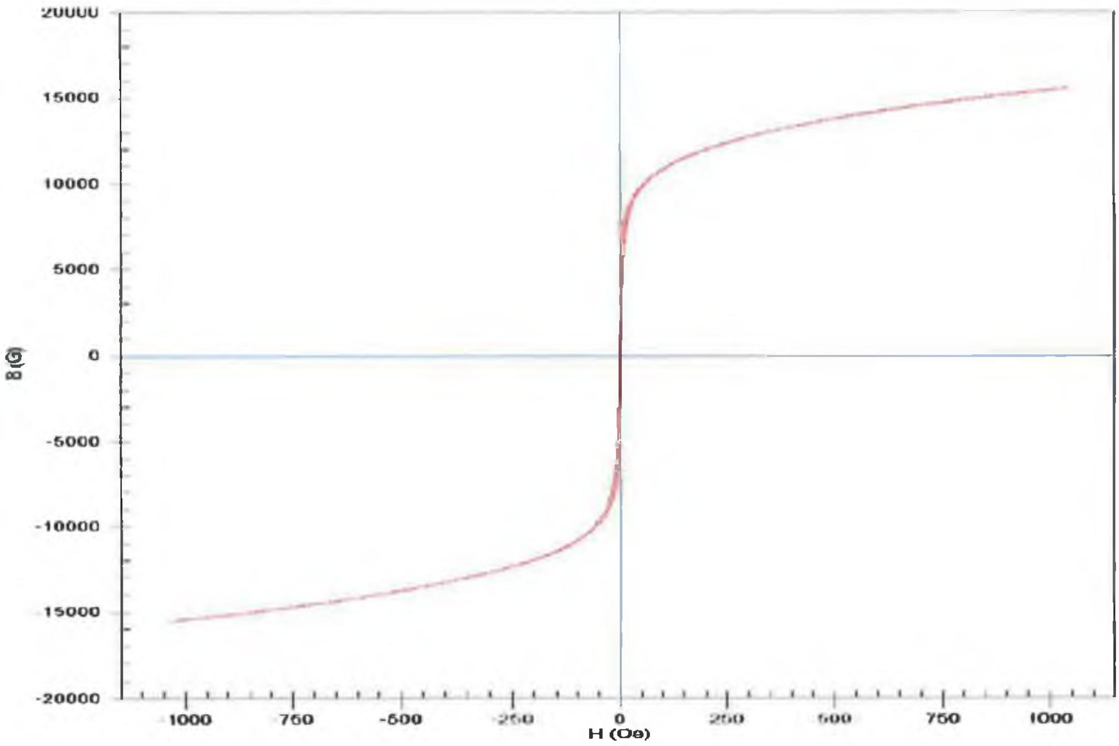

KJS Associates Div. - Excellence in magnetics since 1968.

KJS Associates, Inc. Model SMT-600 Hysteresigraph System

Filename	MS14674, 75 ,76 COMPOSITE.csv	**Print Date**	8 Dec 2005
Test Procedure	ASTM A773/A773M-01	**Version**	2.0.3.0

Comments KJS Associates Div. - Excellence in magnetics since 1968.

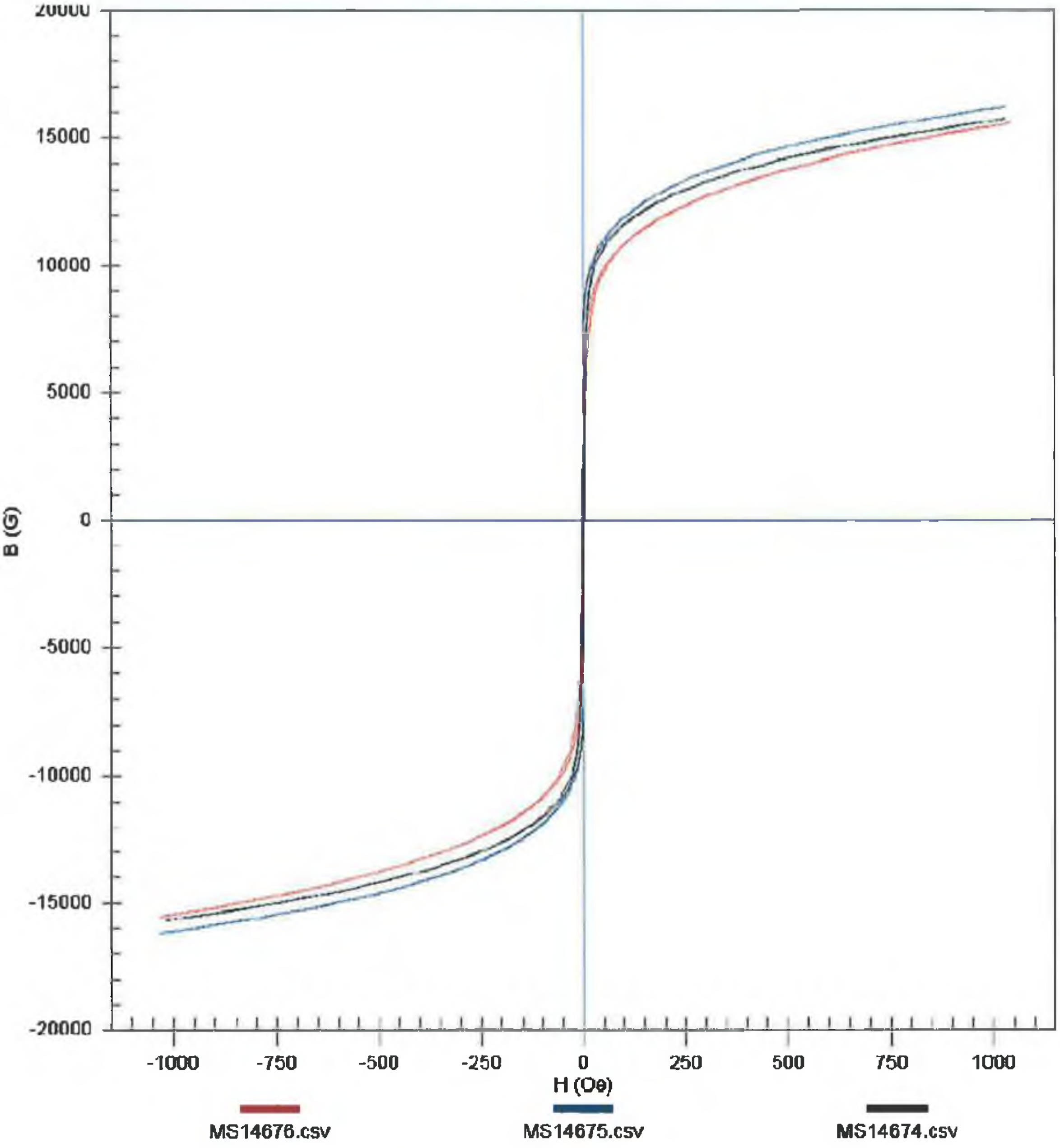

KJS Associates Div. - Excellence in Magnetics Since 1968.

KJS Associates, Inc. Model SMT-600 Hysteresigraph System

Filename	MS14674. 75 ,76 COMPOSITE.csv	**Print Date**	8 Dec 2005
Test Procedure	ASTM A773/A773M-01	**Version**	2.0.3.0

Comments KJS Associates Div. - Excellence in magnetics since 1968.

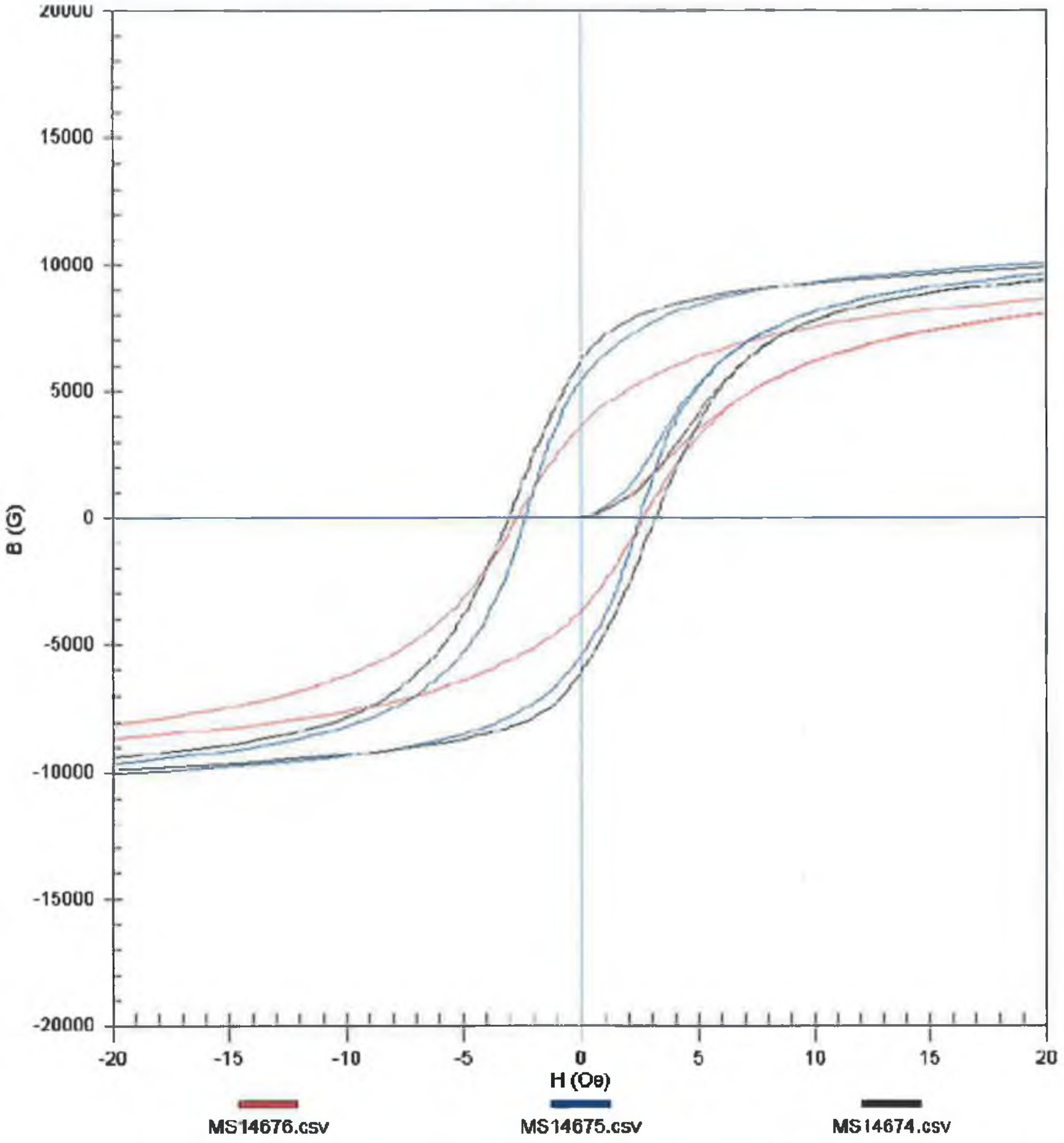

KJS Associates Div. - Excellence in Magnetics Since 1968.

APPENDIX C

Magnetic test result for Co-Si-Fe alloys

KJS Associates, Inc. Model SMT-600 Hysteresigraph System

File Name	MS14677.csv	**Test Date/Time**	8 Dec 2005	
Sample I.D.	Sample 7 1% Co 1% Si 98% Fe	**Test Procedure**	ASTM A773/A773M-01	
Batch I.D.	Dublin City University 20051539	**Operator/version**	JDC	2.0.3.0
Comments	KJS Associates Div. - Excellence in magnetics since 1968.			

SAMPLE INFORMATION		
Diameter	0.6722	in
B Coil Turns	9	
B Coil Resistance	0.4	Ohms
B Coil Wire Thickness	0.011	in
Tape Thickness	0.004	in
Cross Sectional Shape	Circular	
Area Calculation Method	Dimension	
Sample Area	2.28957	cm^2
B Coil Area	2.42083	cm^2

TEST PARAMETERS		
Temperature	25	C
Max. Measured B	15350	G
Max. Measured H	1053	Oe
Step Delay	0	s
TEST SUMMARY		
Remanence Br	5630	G
Coercive Field Hc	3.3	Oe
Max. Permeability umax	771	
B @ Max. Permeability	5856	G
H @ Max. Permeability	7.596	Oe
Demag. Offset	-65	G
Test Type	DC Yoke	

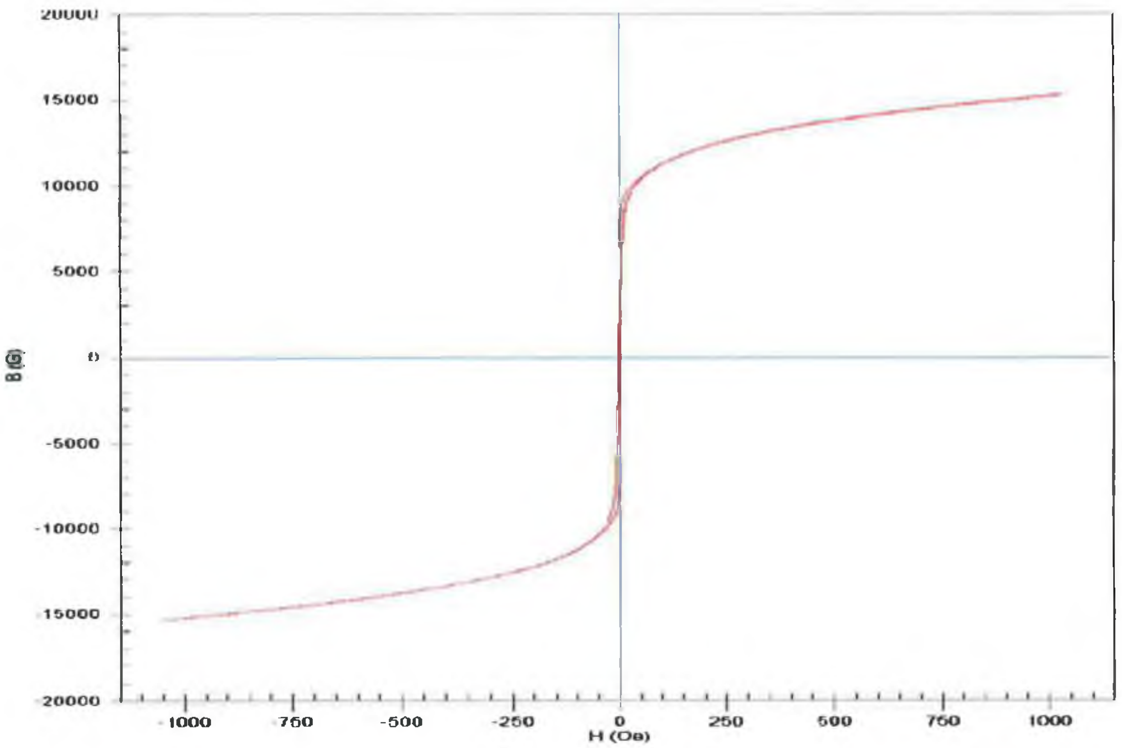

KJS Associates Div. - Excellence in magnetics since 1968.

KJS Associates, Inc. Model SMT-600 Hysteresigraph System

File Name	MS14678.csv	**Test Date/Time**	8 Dec 2005	
Sample I.D.	Sample 8 3% Co 1% Si 96% Fe	**Test Procedure**	ASTM A773/A773M-01	
Batch I.D.	Dublin City University 20051539	**Operator/version**	JDC	2.0.3.0
Comments	KJS Associates Div. - Excellence in magnetics since 1968.			

SAMPLE INFORMATION		
Diameter	0.672	in
B Coil Turns	9	
B Coil Resistance	0.4	Ohms
B Coil Wire Thickness	0.011	in
Tape Thickness	0.004	in
Cross Sectional Shape	Circular	
Area Calculation Method	Dimension	
Sample Area	2.28821	cm^2
B Coil Area	2.41943	cm^2

TEST PARAMETERS		
Temperature	25	C
Max. Measured B	15048	G
Max. Measured H	1018	Oe
Step Delay	0	s

TEST SUMMARY		
Remanence Br	5067	G
Coercive Field Hc	3.72	Oe
Max. Permeability umax	656	
B @ Max. Permeability	4567	G
H @ Max. Permeability	6.958	Oe
Demag. Offset	47	G
Test Type	DC Yoke	

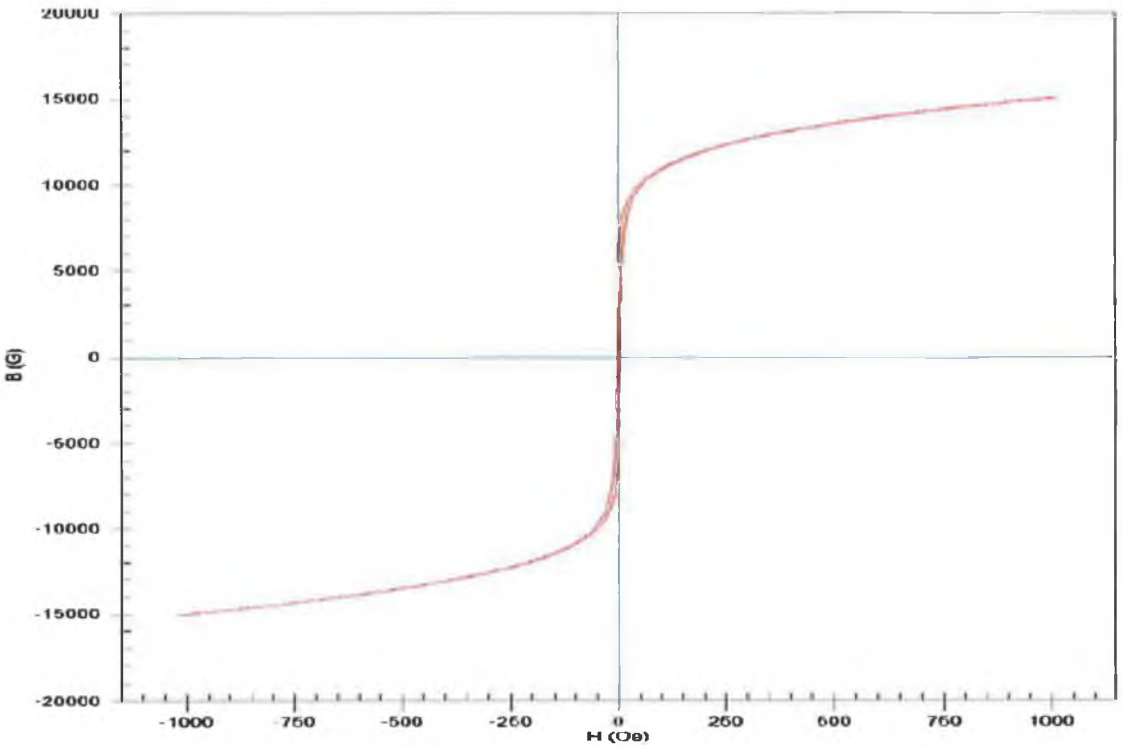

KJS Associates Div. - Excellence in magnetics since 1968.

KJS Associates, Inc. Model SMT-600 Hysteresigraph System

File Name	MS14679.csv	**Test Date/Time**	8 Dec 2005	
Sample I.D.	Sample 9 5% Co 1% Si 94% Fe	**Test Procedure**	ASTM A773/A773M-01	
Batch I.D.	Dublin City University 20051539	**Operator/version**	JDC	2.0.3.0
Comments	KJS Associates Div. - Excellence in magnetics since 1968.			

SAMPLE INFORMATION		
Diameter	0.6716	in
B Coil Turns	9	
B Coil Resistance	0.5	Ohms
B Coil Wire Thickness	0.011	in
Tape Thickness	0.004	in
Cross Sectional Shape	Circular	
Area Calculation Method	Dimension	
Sample Area	2.28549	cm^2
B Coil Area	2.41663	cm^2

TEST PARAMETERS		
Temperature	25	C
Max. Measured B	15116	G
Max. Measured H	1059	Oe
Step Delay	0	s
TEST SUMMARY		
Remanence Br	4972	G
Coercive Field Hc	4.11	Oe
Max. Permeability umax	591	
B @ Max. Permeability	4288	G
H @ Max. Permeability	7.26	Oe
Demag. Offset	68	G
Test Type	DC Yoke	

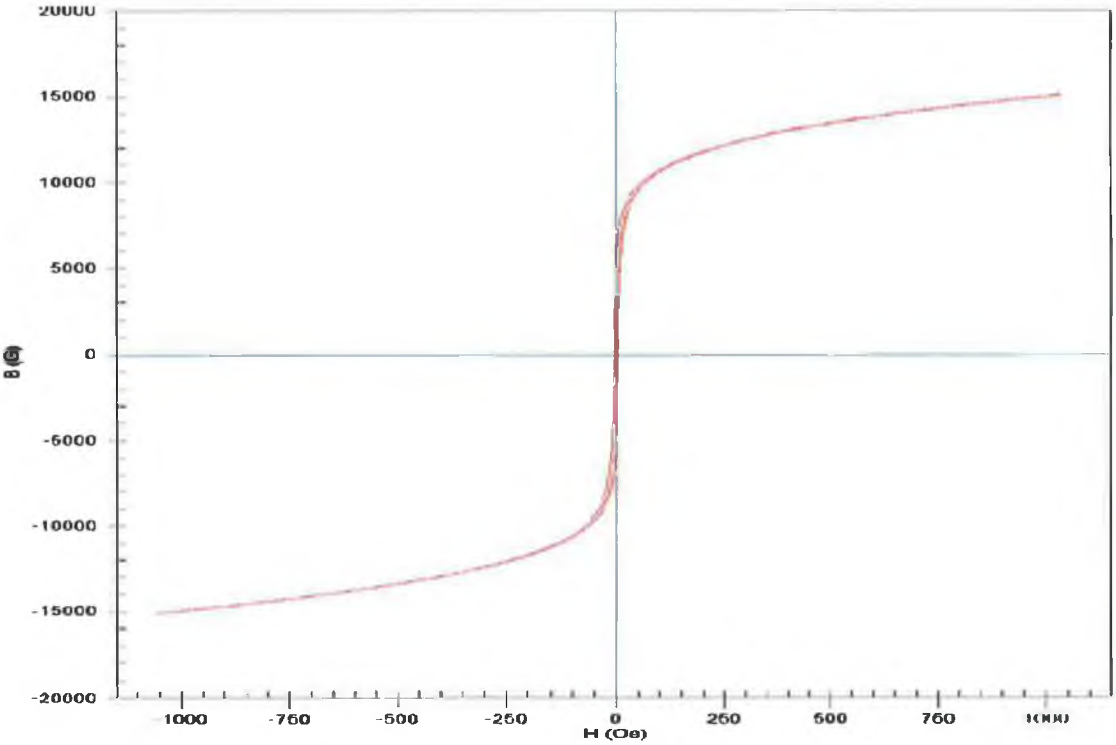

KJS Associates Div. - Excellence in magnetics since 1968.

KJS Associates, Inc. Model SMT-600 Hysteresigraph System

File Name	MS14680.csv	**Test Date/Time**	8 Dec 2005	
Sample I.D.	Sample 10 7% Co 1% Si 92% Fe	**Test Procedure**	ASTM A773/A773M-01	
Batch I.D.	Dublin City University 20051539	**Operator/version**	JDC	2.0.3.0
Comments	KJS Associates Div. - Excellence in magnetics since 1968.			

SAMPLE INFORMATION		
Diameter	0.672	in
B Coil Turns	9	
B Coil Resistance	0.4	Ohms
B Coil Wire Thickness	0.011	in
Tape Thickness	0.004	in
Cross Sectional Shape	Circular	
Area Calculation Method	Dimension	
Sample Area	2.28821	cm^2
B Coil Area	2.41943	cm^2

TEST PARAMETERS		
Temperature	25	C
Max. Measured B	15144	G
Max. Measured H	1021	Oe
Step Delay	0	s
TEST SUMMARY		
Remanence Br	4284	G
Coercive Field Hc	4.28	Oe
Max. Permeability umax	499	
B @ Max. Permeability	4109	G
H @ Max. Permeability	8.237	Oe
Demag. Offset	-11	G
Test Type	DC Yoke	

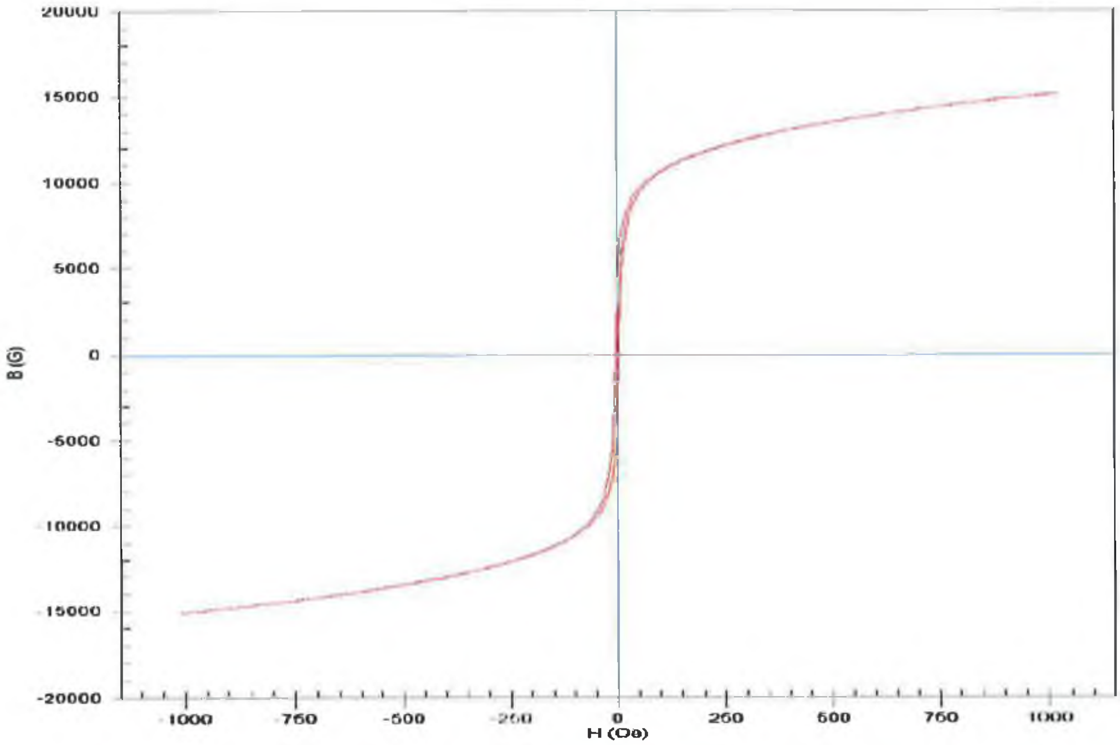

KJS Associates Div. - Excellence in magnetics since 1968.

KJS Associates, Inc. Model SMT-600 Hysteresigraph System

Filename	MS14677, 78 , 79, 80 COMPOSITE.csv	**Print Date**	8 Dec 2005
Test Procedure	ASTM A773/A773M-01	**Version**	2.0.3.0

Comments KJS Associates Div. - Excellence in magnetics since 1968.

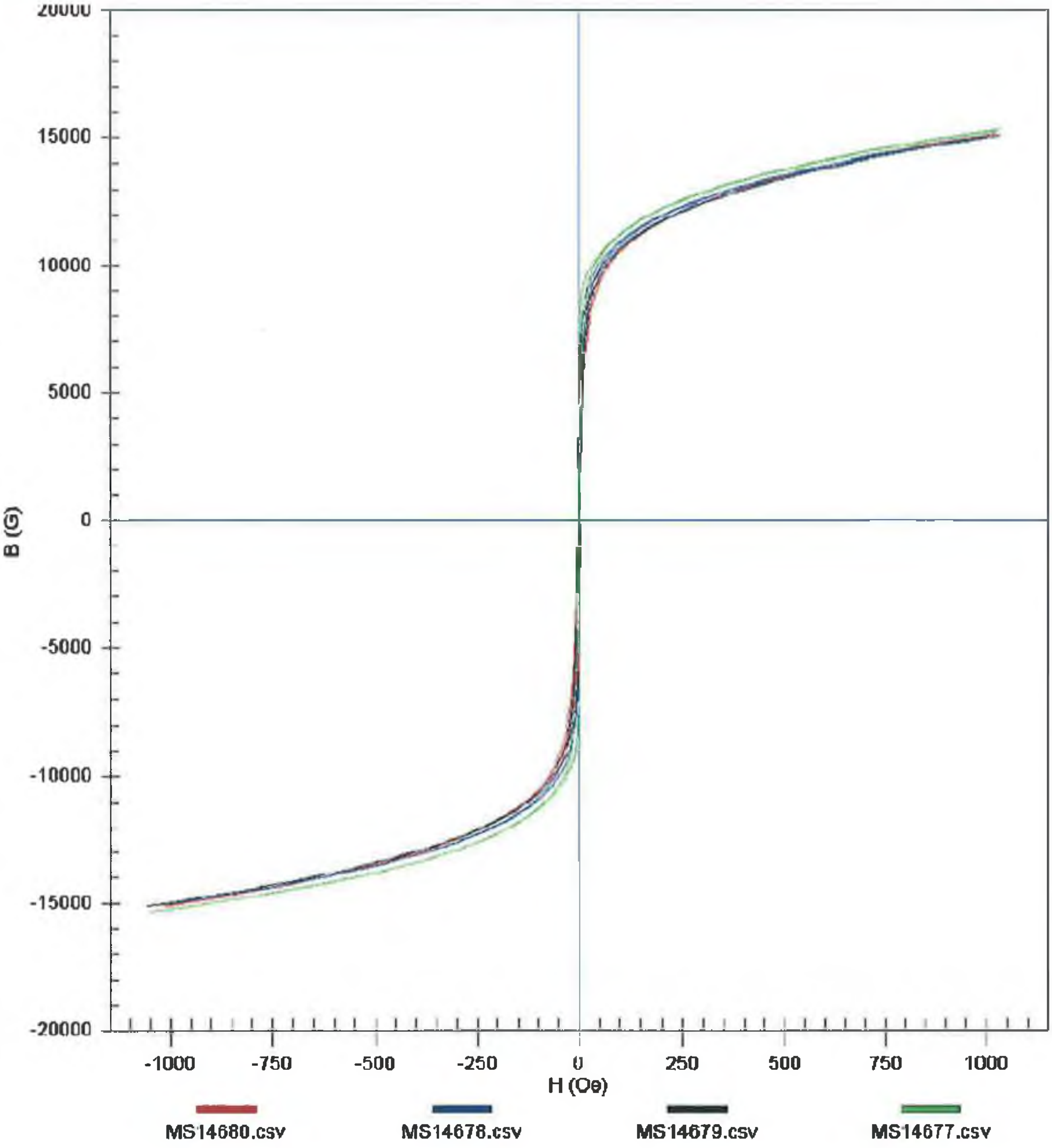

KJS Associates Div. - Excellence in Magnetics Since 1968.

KJS Associates, Inc. Model SMT-600 Hysteresigraph System

Filename	MS14677, 78 , 79, 80 COMPOSITE.csv	**Print Date**	8 Dec 2005
Test Procedure	ASTM A773/A773M-01	**Version**	2.0.3.0

Comments KJS Associates Div. - Excellence in magnetics since 1968.

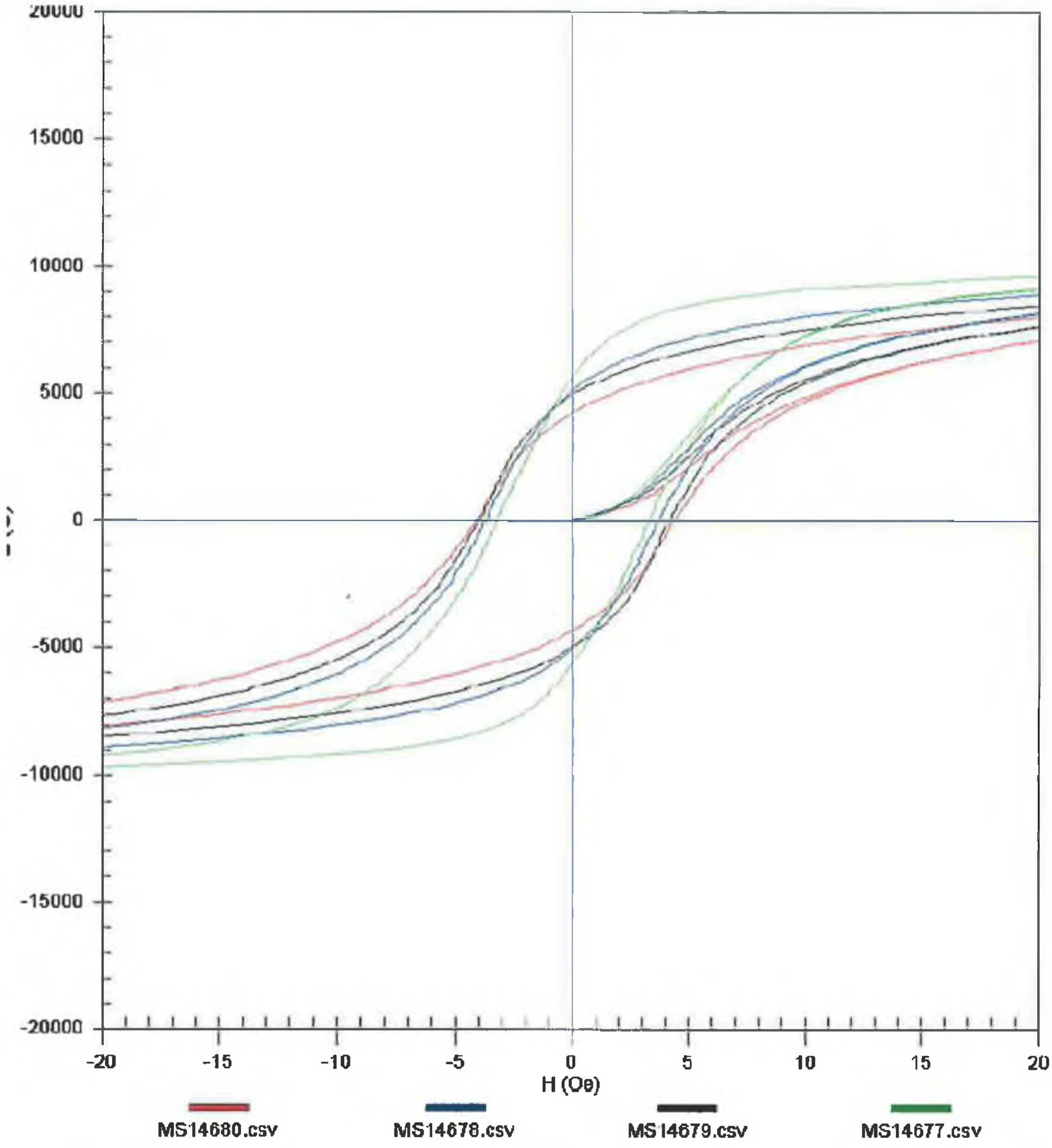

APPENDIX D

List of Publications

1. H. A. Eltawahni, A. G. Olabi and M. S. J. Hashmi, Application of P/M process for producing soft magnetic material, accepted for publication in AMPT 2006, Jul 30- Aug. 3, 2006, Las Vegas, USA.

2. A. G. Olabi and H. A. Eltawahni, Finite element analysis for elector-magnetic solenoid used in medical devices, accepted for publication in 6th international conference on the scientific and clinical application of magnetic carriers, May 17-20, 2006, Krems-Austria.